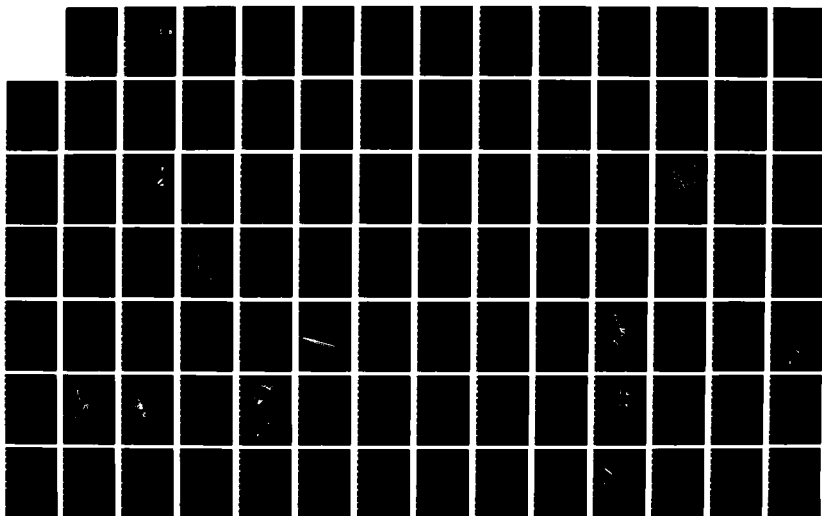
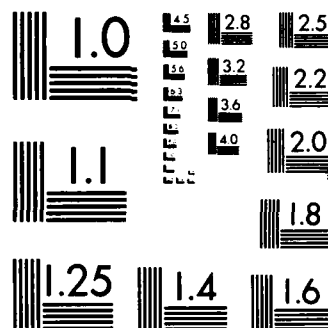


AD-A184 203

TELESEISMIC WAVEFORM MODELING INCORPORATING THE EFFECTS 1/2  
OF KNOWN THREE-DI (U) MASSACHUSETTS INST OF TECH  
CAMBRIDGE EARTH RESOURCES LAB V F CORMIER 08 JUN 87  
AFGL-TR-87-0192 F19628-85-K-0031 F/G 8/11 NL

UNCLASSIFIED





MICROCOPY RESOLUTION TEST CHART  
NATIONAL BUREAU OF STANDARDS-1963-A

AD-A184 203

DTIC FILE COPY

12

AFGL-TR-87-0192

TELESEISMIC WAVEFORM MODELING INCORPORATING THE  
EFFECTS OF KNOWN THREE-DIMENSIONAL STRUCTURE  
BENEATH THE NEVADA TEST SITE

Vernon F. Cormier

Massachusetts Institute of Technology  
Earth Resources Laboratory  
Department of Earth, Atmospheric, and  
Planetary Sciences  
Cambridge, MA 02139

DTIC  
ELECTE  
SEP 02 1987  
S D

8 June 1987

Final Technical Report

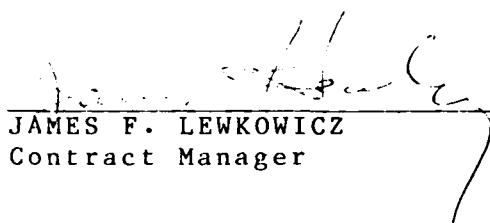
4 February 1985 - 3 February 1987

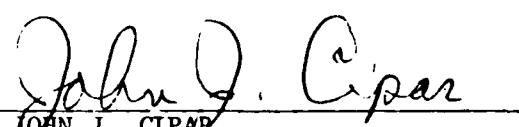
APPROVED FOR PUBLIC RELEASE; DISTRIBUTION UNLIMITED

AIR FORCE GEOPHYSICS LABORATORY  
AIR FORCE SYSTEMS COMMAND  
UNITED STATES AIR FORCE  
HANSCOM AIR FORCE BASE, MASSACHUSETTS 01731


07 9 1 024

"This technical report has been reviewed and is approved for publication"

  
JAMES F. LEWKOWICZ  
Contract Manager

  
JOHN J. CIPAR  
Acting Branch Chief

FOR THE COMMANDER

  
DONALD H. ECKHARDT  
Division Director

This report has been reviewed by the ESD Public Affairs Office (PA) and is releasable to the National Technical Information Service (NTIS).

Qualified requestors may obtain additional copies from the Defense Technical Information Center. All others should apply to the National Technical Information Service.

If your address has changed, or if you wish to be removed from the mailing list, or if the addressee is no longer employed by your organization, please notify AFGL/DAA, Hanscom AFB, MA 01731. This will assist us in maintaining a current mailing list.

Do not return copies of this report unless contractual obligations or notices on a specific document requires that it be returned.

Unclassified

SECURITY CLASSIFICATION OF THIS PAGE

A184 203

## REPORT DOCUMENTATION PAGE

1a. REPORT SECURITY CLASSIFICATION Unclassified			1b. RESTRICTIVE MARKINGS	
2a. SECURITY CLASSIFICATION AUTHORITY			3. DISTRIBUTION / AVAILABILITY OF REPORT Approved for public release; distribution unlimited	
2b. DECLASSIFICATION / DOWNGRADING SCHEDULE				
4. PERFORMING ORGANIZATION REPORT NUMBER(S)			5. MONITORING ORGANIZATION REPORT NUMBER(S) AFGL-TR-87-0192	
6a. NAME OF PERFORMING ORGANIZATION Earth Resources Laboratory, Dept. of Earth, Atmospheric, and Planetary Sciences		6b. OFFICE SYMBOL (If applicable)	7a. NAME OF MONITORING ORGANIZATION Air Force Geophysics Laboratory	
6c. ADDRESS (City, State, and ZIP Code) Massachusetts Institute of Technology Cambridge, MA 02139			7b. ADDRESS (City, State, and ZIP Code) Hanscom Air Force Base Massachusetts 01731	
8a. NAME OF FUNDING / SPONSORING ORGANIZATION Air Force Geophysics Laboratory		8b. OFFICE SYMBOL (If applicable)	9. PROCUREMENT INSTRUMENT IDENTIFICATION NUMBER F19628-85-K-0031	
8c. ADDRESS (City, State, and ZIP Code) Hanscom Air Force Base Massachusetts 01731 J. Lewkowicz/LWH			10. SOURCE OF FUNDING NUMBERS	
			PROGRAM ELEMENT NO. 61101E	PROJECT NO. 5A10
11. TITLE (Include Security Classification) Teleseismic Waveform Modeling Incorporating the Effects of Known Three-Dimensional Structure Beneath the Nevada Test Site				
12. PERSONAL AUTHOR(S) Vernon F. Cormier				
13a. TYPE OF REPORT Final Technical	13b. TIME COVERED FROM 2/4/85 to 2/3/87	14. DATE OF REPORT (Year, Month, Day) 8 June 1987	15. PAGE COUNT 106	
16. SUPPLEMENTARY NOTATION				
17. COSATI CODES			18. SUBJECT TERMS (Continue on reverse if necessary and identify by block number) yield estimation, body wave magnitude, three-dimensional structure, Gaussian beams, ray theory	
FIELD	GROUP	SUB-GROUP		
19. ABSTRACT (Continue on reverse if necessary and identify by block number) The pattern of teleseismic amplitudes from underground nuclear tests has been found to have strong variations as a function of location within a test site. Forward modeling of body waves in known three-dimensional structures beneath seismic sources is used to investigate the effects of such structures on teleseismic amplitudes and to determine the structural resolution necessary to formulate amplitude corrections for variations in source site and recording networks. Three-dimensional structures having scale lengths of 20 to 50 km down to 100 km depth with several per cent fluctuation in P and S velocity are shown to produce a factor of three fluctuation in the amplitude of teleseismic body waves. The associated travel time fluctuations introduced by the three-dimensional structures are weak, being on the order of several tenths of a second, and exhibit only a weak regional correlation with amplitude fluctuations. A known structure beneath Pahute Mesa, Nevada Test Site may be used to formulate amplitude corrections that may reduce the variance in a yield estimate by 25 per cent. Magnitudes based on measurements of coda amplitudes or integrated energy flux in a time window following and including the direct P phase can reduce the fluctuations				
20. DISTRIBUTION / AVAILABILITY OF ABSTRACT <input checked="" type="checkbox"/> UNCLASSIFIED/UNLIMITED <input type="checkbox"/> SAME AS RPT <input type="checkbox"/> DTIC USERS			21. ABSTRACT SECURITY CLASSIFICATION Unclassified	
22a. NAME OF RESPONSIBLE INDIVIDUAL James F. Lewkowicz			22b. TELEPHONE (Include Area Code) 617/377-3028	22c. OFFICE SYMBOL LWH

Unclassified

19. Abstract (continued)

within of observations by a seismic network, but will be only partially successful in reducing the effects of near-source structure.--

unclassified

## 1 Summary

### 1.1 OBJECTIVES

Observations of teleseismic P waves at large aperture arrays have found amplitude fluctuations across the array as large as those observed over worldwide networks. The amplitude fluctuations and their correlation with travel time variations are consistent with the focusing/defocusing effects of three-dimensional velocity structure beneath the array, rather than the effects of intrinsic attenuation. A reciprocal effect on amplitudes is to be expected for variations in the location of underground nuclear tests within a test site. An objective of this project is to predict these amplitude variations using known 3-D structure within a test site. Fast, asymptotically approximate methods of modeling the body wavefield are used to predict these amplitude variations by forward modeling in structures determined from block 3-D inversions of travel times, as well as more detailed models determined from local geophysical surveys at the Nevada test site. The results of these studies can be used to determine the fundamental scale lengths required to produce a correctable amplitude anomaly of a given size.

## 1.2 RESULTS

### 1.2.1 NTS

A known three-dimensional structure beneath Pahute Mesa, Nevada Test Site (Taylor, 1983) can account for many of the features in the azimuthal amplitude pattern of teleseismic P waves from Pahute underground tests. This model can be used to correct for focusing and defocusing effects of the structure beneath Pahute Mesa

For	
A&I	<input checked="" type="checkbox"/>
3	<input type="checkbox"/>
ced	<input type="checkbox"/>
4	

---

1/

---

Library Codes

---

and/or

Special

accounting for factors of three in amplitude fluctuation and for 0.6 sec. in travel time fluctuation. The reduction in variance of teleseismic magnitude or log amplitude using these corrections is about 25 percent, similar to the reduction of variance in teleseismic travel times. These results are useful in predicting the structural resolution needed for models of other test sites to be useful in making corrections for focusing and defocusing. The NTS results suggest that meaningful corrections can be made if the model resolves 10 to 20 km. scale lengths down to 100 km. with perturbations of velocity exceeding 4 percent. Velocity inversions that primarily resolve scale lengths larger than these or that smooth over anomalies larger than 2 percent, (e.g., Montfort and Evans, 1982; Minster et al., 1981), are much less useful in formulating amplitude corrections. By analogy to the Taylor inversion for NTS structure, the data required to resolve structure having these scale lengths would consist of origin times and locations of tests widely distributed over linear dimensions on the order of 100 km. with significant concentrations of tests spaced less than 10 km. apart. It is also necessary to obtain an average crustal structure within the test site from seismograms recorded at local and regional range.

The focusing and defocusing effects of 20 to 50 km. scale length structure having perturbation in P velocity of several percent is nearly independent in the frequency band of teleseismic body waves. This conclusion is even stronger in the 0.2 to 10 Hz. band in which measurements are made on the teleseismic P waves of underground nuclear tests. Frequency dependent effects in the coda of teleseismic P waves are probably due to either the effects of heterogeneities having scale lengths smaller than 20 km. and/or to frequency dependent effects in the scattering processes occurring near the source and receiver.

Magnitude measurements based on the integrated energy in the coda of teleseismic P waves are likely to be more stable because they can remove some of the focusing/defocusing effects of three-dimensional mantle structure near the source. The deeper in the coda, the measurement is made, the less affected it will be by mantle



structure near the source. The optimal time in the coda for this measurement should be as long as possible after the direct P wave given the signal to noise ratio. The minimum time to achieve good stability can be estimated by dividing the length of characteristic scale lengths of mantle structure near the source by the velocity of the presumed scattered wave near the source. For example, assuming a 3.3 km./sec. S wave is scattered into a P wave that is propagated to teleseismic range, one would estimate that after 30 sec. into the coda, the focusing/defocusing effects of 100 km. scale and smaller length structure beneath the source would be minimized. Coda magnitudes, however, are only partially successful in removing the focusing/defocusing effects of structure beneath the source. They cannot remove these effects from the fraction of the coda that is due to scattering of direct P near the receiver.

These conclusions are consistent with tests of the relative performance of coda versus classical magnitudes. The predicted behavior of coda amplitude critically depends on assumptions about the distribution of mantle heterogeneity with depth. Smaller scale heterogeneities with greater percent velocity fluctuations are assumed to be concentrated closer to the surface. Scale lengths on the order of several kilometers to 10 kilometers are assumed in the crust and scale lengths on the order of 10 to 100 kilometers are assumed in the upper mantle. Fluctuations in the mid and lower mantle down to the D'' layer near the core are assumed to be smaller than 1 percent.

### *1.2.2 Descending Slab Structures*

A P velocity model of the Kuril-Kamchatka lithospheric slab determined from travel time study by Creager and Jordan (1986) has been parameterized in three dimensions to investigate amplitude and waveform effects on body waves. Very broad Gaussian beams were used in a reciprocal sense, shooting from receiver to source, to synthesize broad band S waves. The per cent velocity perturbation on S velocity was assumed to be equal to that in P velocity. Frequency dependent effects in the tail of the S pulse were

observed in all azimuths on the side of the slab dipping away from the arc. This "slab diffracted" phase rapidly decays away within 10 to 15 degrees of the azimuth parallel to the strike. The character of the slab diffraction agrees with that seen in finite difference calculations by Vidale (1986) for P waves propagating down dip from an hypocenter in the slab.

The results of these studies will be useful in interpreting the waveform studies of P and S attenuation of the type reported by Choy and Cormier (1986), as well as investigating the shadowing and slab multipathing evident in teleseismic P waves from U.S. nuclear tests on Amchitka Island in the Aleutian arc (Davies and Julian, 1972).

## **2 Publications**

The detailed results of the research conducted under this contract are reported in two refereed publications:

Cormier, V.F., An application of the propagator matrix of dynamic ray tracing: The focusing and defocusing of body waves by three-dimensional velocity structure in the source region, *Geophys. J. R. Astr. Soc.*, 87, 1159-1180, 1986.

Cormier, V.F., Focusing and defocusing of teleseismic P waves by known 3-D structure beneath Pahute Mesa, Nevada Test Site, *Bull. Seism. Soc. Am.*, 77, in press (will appear in October issue), 1987.

The first two papers are included in reprint form in sections 3 and 4. Results of the slab modeling are still being prepared for publication. Preliminary results and modeling are included in a section 5 following the reprints of the two papers referenced above.

### 3 An application of the Propagator matrix ....

(Reprint of a paper by the P.I., *Geophys. J. R. Astr. Soc.*, 87, 1159-1180, 1986.)

**An Application of the Propagator Matrix of Dynamic Ray Tracing:  
The Focussing and Defocussing of Body Waves by Three-Dimensional  
Velocity Structure in the Source Region**

V.F. Cormier\*

\*Earth Resources Laboratory  
Department of Earth, Atmospheric, and Planetary Sciences  
Massachusetts Institute of Technology  
Cambridge, MA 02139

*Geophys J R Astr Soc*, 87, 1986, 1159-1180

**Summary.** Since the dynamic ray tracing system can be written in the linear form  $\frac{dW}{ds} = SW$ , it permits the definition of fundamental matrix and propagator matrix solutions. The propagator matrix can be exploited to connect complex 3-D and 2-D regions to 1-D regions of a model. For example, if the three-dimensional variations of a model are confined only to the portion of the ray path between  $O'$  and  $O_0$ , numerical integration of the linear system need only be performed between  $O'$  and  $O_0$  to construct the propagator  $\Pi(O_0, O')$ . Along the segment of the ray path between  $O'$  and  $O_0$ , traversing a 1-D or homogeneous portion of the model, analytic solutions exist for  $\Pi(O', O_0)$ . Thus  $\Pi(O_0, O_0)$  can be simply obtained by multiplying the analytic and numerically obtained  $\Pi$  matrices. With this procedure, quantities are calculated that are needed for the synthesis of teleseismic P waves by superposition of Gaussian beams. These synthetics are used to investigate the focussing and defocussing of teleseismic P waves by 3-D structure in the vicinity of the source. A source region, having a fluctuation in velocity of 4 per cent over a characteristic scale length of 50 to 100 km., produces factors of two fluctuations in amplitude and several tenths of a second in travel time at teleseismic range in experiments in which either source location is varied at constant azimuth or in which azimuth is varied at constant source location. A model having a maximum fluctuation as small as 0.8 per cent is capable of producing caustics and multipaths at teleseismic range, depending on its distribution of scale lengths and its ratio of vertical with respect to horizontal scale length. The multipaths and caustics of such a model, however, occur over too small an area and are too closely spaced in arrival time to be resolved with seismograph systems in the 0.01 to 4 Hz. band.

## 1 Introduction

All of the asymptotically approximate methods of synthesizing body waves in three-dimensionally varying media are closely related. They all require the calculation of travel times and either geometric spreading or quantities closely related to geometric spreading. In the case of ray theory, a travel time and spreading factor must be estimated between two given points. In the case of Gaussian beams (Červený, 1983) or WKBJ/Maslov seismograms (Chapman and Drummond, 1982) travel times and weighting factors that depend on ray spreading must be calculated. The weighting factors appear in the integrand of a superposition integral over either take-off angles or slowness components measured at the source point. In applications of the Kirchhoff-Helmholtz integral (e.g., Haddon and Buchen, 1981; Scott and Helmberger, 1983), travel time and geometric spreading must be estimated at points on a spatial integration surface.

In any of these techniques, the travel times, weighting factors, and geometric spreading can be calculated in a three-dimensionally varying model by numerical integration of linear differential equations. These equations consist of a kinematic system for ray trajectory and travel time (e.g., Červený et al., 1977) and a dynamic system (Červený and Hron, 1980) for quantities related to the weighting factors and spreading. The kinematic system requires the specification of seismic velocity and its first spatial derivative. In addition to these, the dynamic system requires the specification of the second order spatial derivatives of velocity.

The computational expense of numerical integration of the kinematic and dynamic systems increases with the length of ray paths. Hence, it is desirable to incorporate the known analytic forms of the integrated equations along portions of the ray path traversing regions of the model that are either

homogeneous or vary in only one co-ordinate direction. The patching of analytic to numerical solutions is particularly useful in the synthesis of body waves at teleseismic distances. In this case, long segments of the ray paths are contained in the mid-mantle between 700 km. and 2500 km. depth, where all evidence suggests that velocity fluctuations and departures from radial symmetry are much weaker than either in the crust and upper mantle or in the lowermost mantle (e.g., Dziewonski, 1984; Woodhouse and Dziewonski, 1984).

In the following sections, a procedure is described for the multiplying of propagator matrices to patch analytic to numerical solutions of the equations of dynamic ray tracing. The analytic forms for the elements of this propagator are given for a flattened, 1-D Earth model. Calculations using this propagator are illustrated for the synthesis of P waves at teleseismic distances by superposition of Gaussian beams. The specific problem considered in these calculations is the focussing and defocussing of body waves due to 3-D structure in the region of the source. One example of such focussing and defocussing is the shadowing effect of a subducted lithospheric slab (Sleep, 1973). Other examples, which are discussed in this paper, are related to yield estimation of underground nuclear explosions. At a constant distance, the focussing and defocussing effects of 3-D structure in the source region can introduce an azimuthal variation in the amplitudes of P waves radiated from an explosive, isotropic source. This focussing and defocussing also introduces variations in the apparent yield of explosions of equal yield as their location varies within a test site.

## **2 The linear equations of dynamic ray-tracing**

Both travel times and dynamic spreading quantities can be estimated in 3-D elastic media from a paraxial approximation of the wavefront, in which  $2 \times 2$

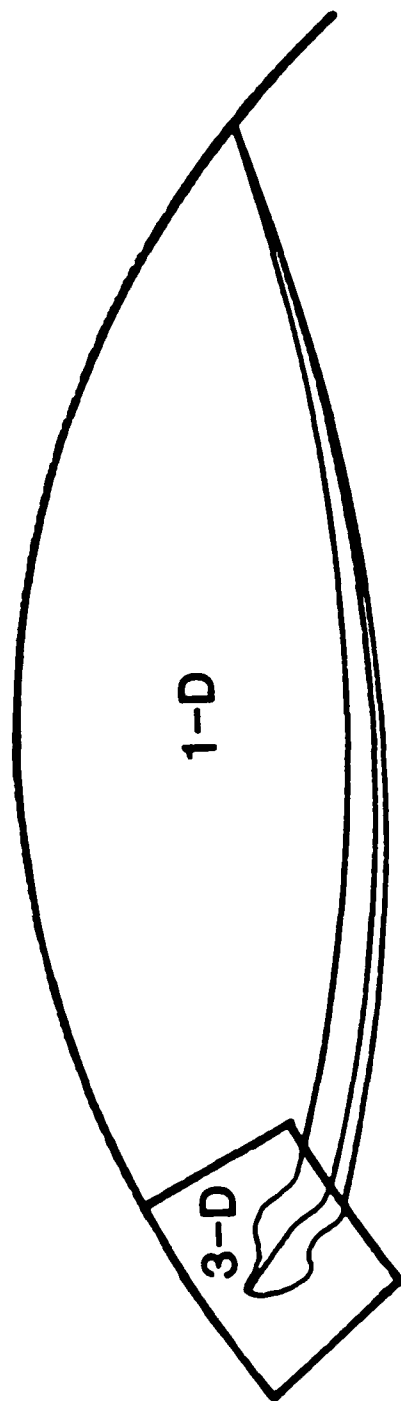


Figure 1. This paper considers the problem of connecting the dynamic ray tracing equations from a 3-D region surrounding the source, in which seismic velocity  $v = v(\tau, \vartheta, \varphi)$ , into a 1-D region, in which  $v = v(\tau)$ , along the remainder of the ray path. (In an Earth-flattened co-ordinate system,  $v = v(x, y, z)$  in the 3-D region;  $v = v(z)$  in the 1-D region.)



matrices  $\mathbf{P}$  and  $\mathbf{Q}$  are defined (Červený, and Pšenčík, 1983). At any given point along a ray the values of  $\mathbf{P}$  and  $\mathbf{Q}$  can be found by integrating a system of linear equations:

$$\frac{d\mathbf{Q}}{ds} = \mathbf{v}\mathbf{P} \quad (1a)$$

and

$$\frac{d\mathbf{P}}{ds} = -\mathbf{v}^{-2}\mathbf{V}\mathbf{Q} \quad (1b)$$

Here  $ds$  is an incremental element of ray path,  $v$  is a local velocity, and  $\mathbf{V}$  is a matrix of second derivatives with respect to ray centered co-ordinates that move along the ray. The elements of  $\mathbf{V}$  are

$$\mathbf{V} = \begin{bmatrix} v_{11} & v_{12} \\ v_{21} & v_{22} \end{bmatrix} \quad (2)$$

The subscripts on the elements of  $\mathbf{V}$  denote differentiation of velocity  $v$  with respect to the ray centered co-ordinate directions  $q_1$  and  $q_2$ .

Equations (1a-b) can be rewritten as a single linear system consisting of four equations:

$$\frac{d\mathbf{W}}{ds} = \mathbf{S}\mathbf{W} \quad (3)$$

where  $\mathbf{W}$  is a column vector having four components and  $\mathbf{S}$  is a  $4 \times 4$  matrix. The form of such a system is similar to the system for stress-displacement components in a vertically varying medium. Here, of course, the differentiation is with respect to incremental path length along a ray rather than depth. Just as for the stress-displacement system, propagator matrix solutions can be found to this system. Specifically, Červený (1985a) has defined a fundamental matrix for the equation system (3), which can be normalized to a  $4 \times 4$  propagator matrix  $\Pi(O_0, O_s)$  by choice of initial conditions at a point  $O_s$ , so that  $\mathbf{W}(O_0) = \Pi(O_0, O_s)\mathbf{W}(O_s)$ . Since  $\Pi$  is a propagator matrix, it has the property that  $\Pi(O_s, O_s) = \mathbf{I}$ , where  $\mathbf{I}$  is the identity matrix. Also, given a point  $O'$  between  $O_s$  and  $O_0$ ,  $\Pi(O_0, O_s) = \Pi(O_0, O')\Pi(O', O_s)$ . This property can be used to accelerate

two point ray tracing and the calculation of spreading functions and weighting factors needed for synthesis of body waves in three-dimensionally varying media. For example, if the three-dimensional variations of a model are confined only to the portion of the ray path between  $O'$  and  $O_s$ , numerical integration of the linear system need only be performed between  $O'$  and  $O_s$  to construct  $\Pi(O_s, O')$ . Along the segment of the ray path between  $O'$  and  $O_s$ , traversing a 1-D or homogeneous portion of the model, analytic solutions exist for  $\Pi(O', O_s)$  (Figure 1). Thus  $\Pi(O_s, O_s)$  can be simply obtained by multiplying the analytic and numerically obtained  $\Pi$  matrices.

### 3 The elements of the propagator matrix

#### 3.1 GENERAL 3-D

The  $\Pi$  matrix can be defined in terms of 2 x 2 sub matrices  $P$  and  $Q$  as follows:

$$\Pi = \begin{bmatrix} Q^I & Q^R \\ P^I & P^R \end{bmatrix} \quad (4)$$

The superscripts  $I$  and  $R$  distinguish solutions to the dynamic ray tracing equations (1a-b) using plane wave and point source initial conditions respectively. The initial conditions for  $Q^I$ ,  $P^I$  and  $Q^R$ ,  $P^R$  have been discussed extensively by Červený and Pšenčík (1983a,b) and Červený (1985a,b) in the context of the general complex solutions of eq. (3) for Gaussian beams. The simplest form of the initial conditions are that at  $O_s$

$$Q^R = 0 ; P^R = I \quad (5a)$$

and

$$Q^I = I ; P^I = 0 \quad (5b)$$

Eqs. (5a,b) are necessary for  $\Pi$  to have propagator character; more general conditions can be incorporated by specifying  $W(O_s)$ .

### 3.2 1-D

In order to determine the elements of the  $\Pi$  matrix, a vector basis must first be selected for the ray centered co-ordinate system  $(q_1, q_2, s)$  at the point at which initial conditions are specified. Here, given a fixed Cartesian co-ordinate system  $(x, y, z)$ , the ray will be assumed to be confined to the  $(x, z)$  plane in a 1-D medium and the  $e_1$  direction will be chosen to point in the  $y$  direction. A vector  $e_2$  is chosen such that  $(e_1, e_2, t)$  forms an orthogonal, right-handed vector basis, where  $t$  is the ray tangent.

With this definition of the ray centered co-ordinate system, and assuming that velocity varies only as a function of  $z$  (1-D medium), it is possible to derive analytic expressions for the elements of  $\Pi$ . The solutions for the spreading of a line source in a vertically ( $z$ ) varying medium have been given by Madariaga (1984). These are appropriate for the components  $Q_{ij}, P_{ij}, i, j = 2, 2$ . For the spreading of a point source in three dimensions, solutions for the components  $i, j = 1, 1$  must be added to these. The components  $i, j = 1, 1$  are quite simple in form. This is because by the choice of the ray centered co-ordinates in the 1-D medium,  $v_{11} = 0$ . The off diagonal elements of the  $Q$  and  $P$  matrices are all zero because the velocity  $v$  is assumed not vary in the  $x$  and  $y$  directions. In summary, the 16 components of the  $\Pi$  matrix in a vertically varying medium are

$$Q'_{11} = P^R_{11} = 1$$

$$Q^R_{11} = \frac{X}{p}$$

$$Q'_{12} = Q^R_{12} = P^I_{11} = P^I_{12} = P^R_{12} = Q'_{21} = Q^R_{21} = P^I_{21} = P^R_{21} = 0$$

$$Q'_{22} = \cos\delta \left( \frac{1}{\cos\delta_0} + p^2 v_s^2 \frac{dX}{dp} \right) \quad (6)$$

$$Q_{22}^R = \cos\delta \cos\delta_0 \frac{dX}{dp}$$

$$P_{22}^I = \frac{p^2 v_s^0}{\cos\delta} (1 - p^2 v_s \cos\delta \frac{dX}{dp}) - p^2 \frac{v_s}{\cos\delta_0}$$

$$P_{22}^R = \frac{\cos\delta_0}{\cos\delta} (1 - p^2 v_s \cos\delta \frac{dX}{dp})$$

If a ray has a turning point, then the angle  $\delta$  must be in the range  $0 < \delta < \pi$ . When a ray is propagating downward in the direction of the positive depth ( $z$ ) axis,  $\delta$  is in the range  $(0, \frac{\pi}{2})$ ; when it is propagating upward,  $\delta$  is in the range  $(0, \pi)$ . This extended angular range is important for properly describing plane wave caustics at turning points (Madariaga, 1984). It is also essential to include in the calculation of  $\Pi$  elements in a product of  $\Pi$  matrices whenever one of the member matrices is associated with a turning ray.

### 3.3 CONNECTING REGIONS

With the elements of the propagator  $\Pi$  above, it can be verified that for any point  $O'$  along the ray path at which the velocity and its first spatial derivatives are continuous, that

$$\mathbf{X}(O_0) = \Pi(O_0, O') \cdot \Pi(O', O_s) \cdot \mathbf{X}(O_s) \quad (7)$$

where  $\mathbf{X}(O_s)$  is a  $4 \times 2$  matrix of initial conditions on  $\mathbf{P}$  and  $\mathbf{Q}$ , and  $\mathbf{X}(O_0)$  is a  $4 \times 2$  matrix formed from a linear combination of plane wave (I) and point source solutions (R) for  $\mathbf{P}$  and  $\mathbf{Q}$ . For example, point source initial conditions at  $O_s$

$$\text{can be specified by setting } \mathbf{X}(O_s) = \begin{bmatrix} 0 & 0 \\ 0 & 0 \\ 1 & 0 \\ 0 & 1 \end{bmatrix}. \text{ Then by eqs. (7) and (4), } \mathbf{X}(O_0) = \begin{bmatrix} \mathbf{Q}^R \\ \mathbf{P}^R \end{bmatrix}.$$

It can also be shown by substitution of the definitions of eqs. (6), that  $\Pi(O_0, O_2) = \Pi(O_0, O') \Pi(O', O_2)$ , that the determinant of  $\Pi$  is constant along the ray path, and that  $\det \Pi = 1$ .

If the velocity or its first spatial derivative are discontinuous at  $O'$ , then the jump conditions defined by Červený (1985a) must first be applied to the elements of  $\Pi(O', O_2)$  before the multiplication of eq. (7) is performed. These jump conditions are identical for both plane wave and point source solutions. The jump conditions can be compactly expressed by a  $4 \times 4$  matrix  $F$ , with eq. (7) becoming

$$X(O_2) = \Pi(O_0, O^+) F \Pi(O^-, O_2) X(O_2) \quad (8)$$

where the + sign refers to quantities evaluated on the incident side of the boundary at  $O'$  and the - sign refers to quantities evaluated on the transmitted side of the boundary at  $O'$ . The elements of  $F$  are given in Červený (1985a) for the most general case of discontinuities in velocity and its first spatial derivatives. For the co-ordinate system chosen here and for velocity depending only on  $z$ , the elements of  $F$  are all zero except for

$$F_{11} = F_{33} = 1$$

$$F_{22} = \frac{\cos \delta^-}{\cos \delta^+} \quad (9)$$

$$F_{42} = \frac{1}{\cos \delta^- \cos \delta^+} p^2 (\cos \delta^- v_z^+ - \cos \delta^- v_z^-)$$

$$F_{44} = \frac{\cos \delta^+}{\cos \delta^-}$$

Thus, computations with the propagator matrix of dynamic ray tracing are not

completely analogous to those using the stress-displacement propagator. In the former case, the dynamic ray tracing propagator is discontinuous at first and second order velocity discontinuities, while in the latter case the stress-displacement propagator is continuous at solid-solid boundaries. The patching of solutions in 1-D and homogeneous regions to those in 3-D regions is most conveniently performed at pseudo boundaries at which velocity and its first spatial derivatives are continuous. Patching can be performed at more general boundaries, but the jump conditions must first be used to correct  $P$  and  $Q$  elements to values appropriate for the transmitted side of the boundary.

A final note should be made that in order for the  $\Pi$  matrix to have the properties of a propagator, one must use the plane wave initial conditions (5b) in calculating  $P'$ ,  $Q'$  rather than the modified plane wave conditions recommended by Madariaga (1984) for a source in a region having a non-zero velocity gradient. The modified initial conditions of Madariaga (1984) were proposed to obtain phase fronts at the source that were equivalent to plane waves. This condition was necessary to stabilize the computation of Gaussian beam seismograms. It also makes Gaussian beam synthesis more closely resemble the process of plane wave superposition upon which the WKBJ/Maslov technique (Chapman and Drummond, 1982) is formulated. Recently, however, Červeny' (1985a,b) has proposed optimal beam width parameters that are equivalent to plane wave fronts at the receiver. These parameters are optimal in the sense of minimizing the error in discretizing and truncating the integral that superposes beams. This choice of beam parameters also addresses the stability problem noted by Madariaga. For a source and receiver both at the surface, Červeny''s optimal beam width parameters are reciprocally equivalent to Madariaga's modified plane wave initial conditions. This can be demonstrated using the propagator matrix of dynamic ray tracing and reciprocal relations between elements of the  $P$  and  $Q$  matrices.

Section 4, which follows, reviews the procedures used in synthesizing the seismograms shown and discussed in section 5. These P wave seismograms were synthesized by a summation of Gaussian beams, in which the propagator  $\Pi$  was used to connect a region having 3-D variations in velocity to a 1-D region.

#### 4 Gaussian beam summation in a 3-D model

##### 4.1 THE TECHNIQUE

Seismogram synthesis by Gaussian beams in three-dimensionally varying media has been fully described by Červený (1985a,b). The steps are repeated here only in summary form, emphasizing the particular choices made for the parameters affecting beam widths and special considerations in the use of propagator matrices.

A spectral component of vertical displacement observed at point  $S$  was calculated by

$$u(\omega, S) = \int \int \varphi^N(\gamma_1, \gamma_2) \hat{U}^N(O_s) \exp[i\omega\tau(S, O_s) - \frac{i\pi}{2}k(O_s, O_s)] d\gamma^2 \quad (10)$$

Seismograms were synthesized in the time domain by the spectral method, in which eq. (10) was first evaluated at the discrete frequencies required by a fast Fourier transform. Source spectra and seismograph responses were applied in the frequency domain before inverse transforming to the time domain.

In eq. (10),  $\gamma_1, \gamma_2$  are take-off angles at the source point  $O_s$ .  $\varphi^N(\gamma_1, \gamma_2)$  is a weighting function that varies for each set of take-off angles.  $\hat{U}^N$  is a factor that includes radiation pattern and source normalization but does not include geometric spreading.  $O_s$  is the orthogonal projection of point  $S$  onto the ray. For the applications here,  $O_s$  can be taken as the ray end point on the surface of the Earth.  $\tau(S, O_s)$  is the Gaussian beam complex-valued travel time at  $S$ , which is defined in terms of ray centered co-ordinates by

$$\tau(S, O_0) = \tau(O_0) + \frac{1}{2} \mathbf{q}^T \mathbf{M}(O_0) \mathbf{q} \quad (11)$$

$\mathbf{M}$  is a  $2 \times 2$  symmetric matrix of the second derivatives of the complex valued travel time with respect to the ray centered co-ordinates  $\mathbf{q}^T = (q_1, q_2)$ .  $\mathbf{M}$  is evaluated from

$$\mathbf{M} = \mathbf{P}\mathbf{Q}^{-1} \quad (12)$$

$k(O_s, O_0)$  is an integer index, which Ziolkowski and Deschamps (1980) have termed the KMAH index. The KMAH index specifies the number of  $\frac{\pi}{2}$  phase advances encountered as each caustic is passed by a ray. Practical calculation of the KMAH in three-dimensionally varying media is discussed in greater detail in Chs. 4 and 6 of Červený (1985a). Examples of its calculation in 2-D media are given in Chapman and Drummond (1982), Nowack and Aki (1984), and Cormier and Spudich (1984).

#### 4.2 BEAM PARAMETERS

The  $\mathbf{P}$  and  $\mathbf{Q}$  matrices of eq. (12) are generally complex. The complex matrices  $\mathbf{P}$  and  $\mathbf{Q}$  are completely specified at any point by the  $2 \times 4$  matrix  $\mathbf{X}$  of eq. (7), with  $\mathbf{P}$  and  $\mathbf{Q}$  being the lower and upper  $2 \times 2$  submatrices respectively of the  $\mathbf{X}$  matrix. Červený (1985a,b) specifies beam parameters using  $\mathbf{M}$  rather than  $\mathbf{P}$  and  $\mathbf{Q}$  individually. This is analagous to imposing initial conditions on the "impedance ratio"  $\mathbf{X} = \mathbf{X}\mathbf{Q}^{-1}$  at ray end points. The propagator relation of eq. (7) makes it possible to specify complex initial conditions at any point along a ray path. Thus at the ray end point  $O_0$ ,  $\mathbf{X}(O_0)$  can be specified by

$$\mathbf{X}(O_0) = \begin{bmatrix} \mathbf{I} \\ \mathbf{P}\mathbf{Q}^{-1} \end{bmatrix} = \begin{bmatrix} \mathbf{I} \\ \mathbf{M} \end{bmatrix} \quad (13)$$

At any other point along the ray, say point  $O_s$  at the source,

$$\mathbf{X}(O_s) = \mathbf{\Pi}(O_s, O_0) \mathbf{X}(O_0) \quad (14)$$

In the example calculations, the initial conditions were specified on  $\mathbf{M}$  at the ray



end points, as in eq. (13). The source point  $O_s$  and ray end points  $O_e$  were chosen to be in locally homogeneous layers.  $\text{Re } \mathbf{M}(O_e)$  was specified by Červeny's "effective plane-wave" condition. For a homogeneous layer, this condition reduces to

$$\text{Re } \mathbf{M} = \mathbf{O} \quad (15)$$

where  $\mathbf{O}$  is a  $2 \times 2$  matrix of zeros. The effective plane wave condition is the set of initial conditions that produce zero second derivatives of the travel time field along the Earth's surface. With this choice, the real part of the complex travel time  $\tau(S, O_e)$  becomes

$$\tau(S, O_e) = \tau(O_e) + \mathbf{p} \cdot [(\mathbf{x}(S) - \mathbf{x}(O_e))] \quad (16)$$

where  $\mathbf{p}$  is the vector slowness at the end point of the ray;  $\mathbf{x}(S)$  is the cartesian position vector of the receiver; and  $\mathbf{x}(O_e)$  is the cartesian position vector of the ray end point. In this form, the real part of the complex travel time  $\tau(S, O_e)$  resembles the phase function in the WKBJ/Maslov technique (Chapman and Drummond, 1982).

$\text{Im } \mathbf{M}$  was selected at ray end points to minimize the error in the discretization of the superposition integral. If the ray end point is in a homogeneous layer, this condition reduces to

$$|\text{Im } \mathbf{M}| = |\mathbf{M}^R|, \quad (17)$$

where  $|\mathbf{M}^R|$  denotes an absolute value of the matrix  $\mathbf{M}^R = \mathbf{P}^R(\mathbf{Q}^R)^{-1} \mathbf{M}^R$  can be calculated by finding the matrix of  $\Omega$  of eigenvectors of  $\mathbf{M}^R$  associated with eigenvalues  $\lambda_1, \lambda_2$  and computing

$$|\mathbf{M}^R| = \Omega \begin{bmatrix} |\lambda_1| & 0 \\ 0 & |\lambda_2| \end{bmatrix} \Omega^T \quad (18)$$

Note that the choices (15) and (17) for complex  $\mathbf{M}$  at the ray end point  $O_e$  uniquely determine the value of complex  $\mathbf{M}$  at the source or starting point of integration  $O_s$ . The value of complex  $\mathbf{M}$  at  $O_s$  may be found by propagator multiplication as in eq. (14). The value  $\mathbf{M}(O_s)$ , however, does not need to be

calculated in order to evaluate the integrand of eq. (10). Moreover, beam parameters may be specified at any point along a ray through a complex  $\mathbf{M}$  matrix. For example, one may specify the parameters at the point where a ray is incident on some boundary. The values of complex  $\mathbf{M}$ , which control beam decay and interference, are then uniquely determined at either end point of the ray by the propagator relation.

If initial conditions are specified at the end points  $O_0$ , the weighting function  $\varphi^N$  in eq. (9) becomes

$$\varphi^N = \frac{\omega}{2\pi} |\det \mathbf{Q}^R| [-\det(\mathbf{M}(O_0) - \mathbf{M}^R(O_0))]^{\frac{1}{2}} \quad (19)$$

with the branch cut of the square root taken such that

$$\text{Re}[-\det(\mathbf{M}(O_0) - \mathbf{M}^R(O_0))]^{\frac{1}{2}} > 0.$$

The amplitudes  $\hat{U}^N$  were taken to be constant over all beams and source locations in the example calculations described in the next section. This neglects effects of the additional component of Gaussian beams, as well as factors having to do with source normalization and the free surface coefficient. In all examples shown, both the additional component and the free surface coefficient had insignificant variations over the spot ellipse (the boundary surrounding a beam at which  $e^{-1}$  decay is achieved). Likewise in experiments involving variations in source locations, velocity variation was too small to significantly affect a source normalization factor.

With beam parameters specified at ray end points, the evaluation of eq. (10) only requires knowledge of  $\mathbf{P}^R$ ,  $\mathbf{Q}^R$  at ray end points.  $\mathbf{P}^I$ ,  $\mathbf{Q}^I$ , however, must also be known along both analytically and numerically integrated segments if propagator products are evaluated.

The calculation of the KMAH index is simplified because any square roots appearing in the integrand of eq. (10) depend only on  $\mathbf{P}^R$ ,  $\mathbf{Q}^R$ . The changes in

sign of  $\det \mathbf{Q}^R$  and the trace of  $\mathbf{Q}^R$  are tracked along rays in the numerically integrated regions of a model. Along the analytically integrated sections of a ray path, the signs of these quantities are compared before and after the propagator multiplications. The KMAH index is advanced one unit if the sign of  $\det \mathbf{Q}^R$  changes but the sign of the trace of  $\mathbf{Q}^R$  remains unchanged. The KMAH index is advanced two units if the signs of both  $\det \mathbf{Q}^R$  and the trace of  $\mathbf{Q}^R$  change ( see Červený, 1985a ). For this procedure to work along segments that are analytically integrated by propagator multiplication, it is important to allow the angle  $\delta$ , which appears in all analytically computed elements, to be defined over an angular range that exceeds  $\frac{\pi}{2}$  whenever a ray passes through a turning point.

#### 4.3 BEAM DECAY AND INTERFERENCE

Figures 2 and 3 illustrate how the waveforms obtained from Gaussian beam superposition critically depend on two phenomena: the exponential decay rate away from the central ray, and the constructive interference of the phase of neighboring beams. In Figure 2, the values of the exponential decay power at 1 Hz. are plotted at the beam end points in the vicinity of a teleseismic station at  $70^\circ$  distance for beams departing from one of the 3-D models of a source region that are discussed in the next section. These decay rates were calculated for the beam parameters given by eqs. (15) and (17). Note that a large region can potentially contribute to a 1-Hz. signal. Lower frequencies would have a proportionally smaller beam decay. A 0.03 Hz signal would have contributions from beams as much as 1000 km. or more away from the station. Equally important, however, are the effects of constructive interference shown in Figure 3. For these beam parameters, the region of constructive interference of a 1 Hz. wavelet is slightly larger than the region in which exponential decay is

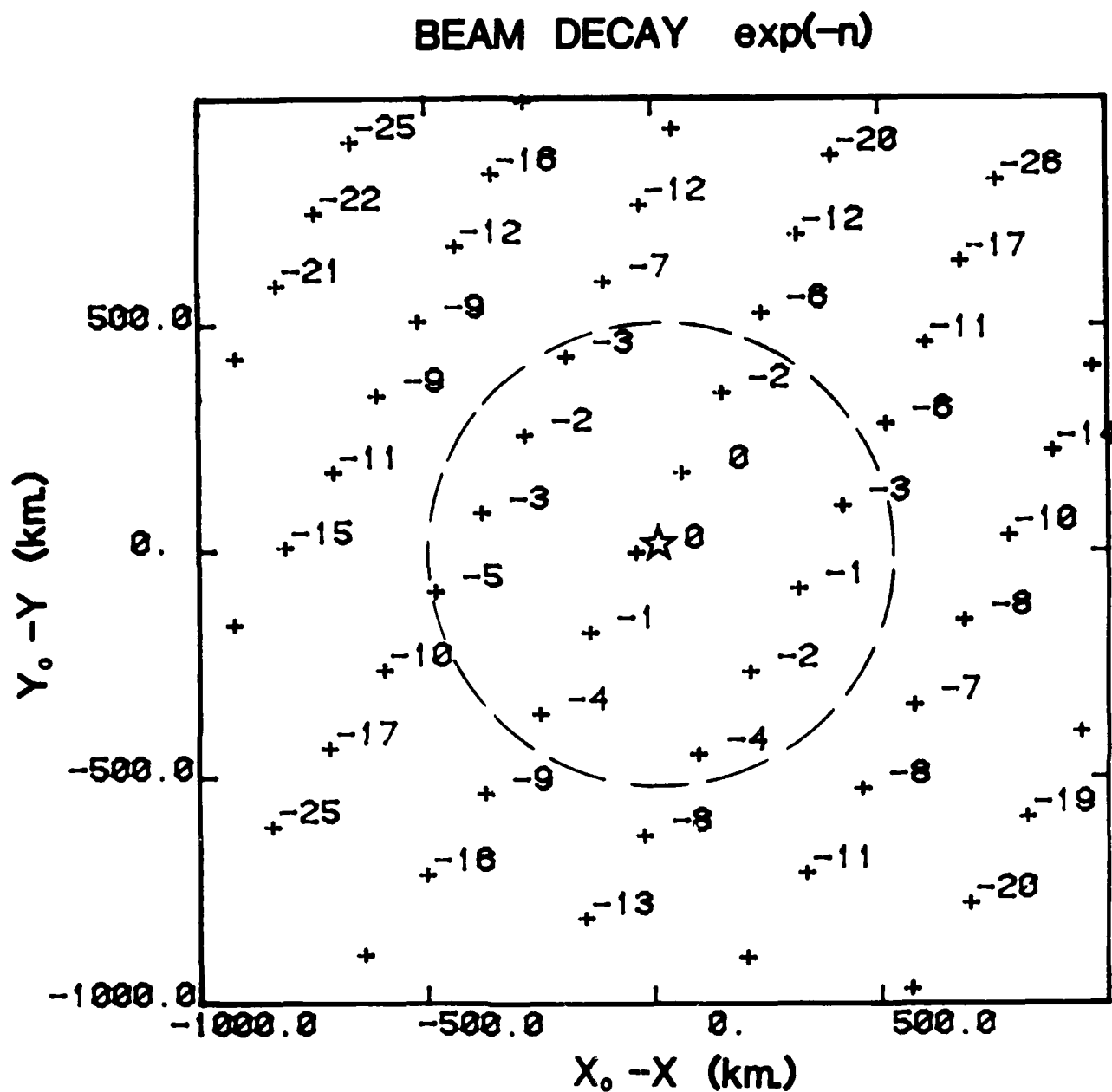


Figure 2. The value of  $n$ , where  $n = \omega \operatorname{Im}(\mathbf{q}^T \mathbf{M} \mathbf{q})$ , is shown here at beam end points. The amplitudes of Gaussian beams are controlled by the factor  $e^{-n}$ . The values shown are at 1 Hz. ( $\omega = 2\pi$  rad/sec.) and are reported to the nearest integer at ray end points in the vicinity of a receiver marked by the star. The  $e^{-6}$  contour of amplitude is dashed.

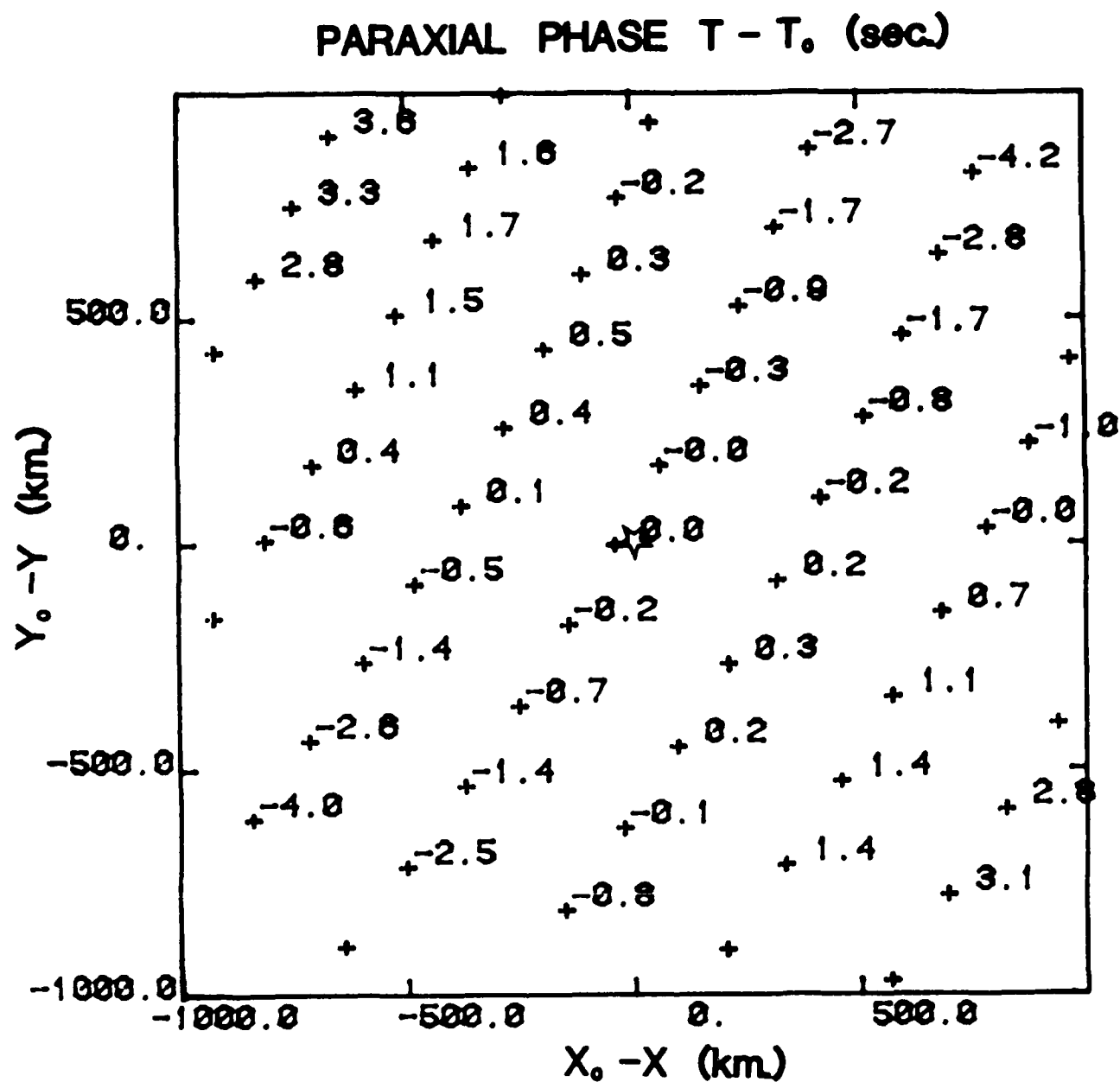


Figure 3. The values of the paraxially approximated phase  $T$  referenced to the travel time  $T_0$  of a ray connecting the source with the receiver marked by the star.  $T$  was calculated by the "equivalent plane wave" condition at beam end points. For a homogeneous layer at the receiver, this condition will give the paraxial approximation of eq. (16).

small.

## 5 Results with a 3-D model of the source region

### 5.1 A MODEL INVERTED FROM TRAVEL TIMES

The focussing and defocussing of teleseismic body waves by 3-D structure in the vicinity of the source have been investigated with two different models. The first model is one obtained by Zandt (1981) for central California using a block inversion of teleseismic travel times by the method of Aki et al. (1976).

The Zandt (1981) model has four layers from 0.0 to 90.0 km in depth. The horizontal block size is 10.0 km in the top layer and 20.0 to 25.0 km in the lower layers. Average velocity variations are between 4.0 to 8.0 percent in the top layer and 2.0 to 4.0 percent in the lower layers. The rms velocity variation measured over grid points, however, is generally much lower, on the order of less than 2 percent. This is because the largest variations take place over relatively broad regions, having characteristic scale lengths of between 50 to 100 km. (Figure 4).

Seismograms were synthesized in this model by summation of Gaussian beams. An explosive point source was assumed at the center of the model at 9.6 km. depth. The  $\Pi$  elements were calculated in the 3-D source region by numerical integration of the kinematic and dynamic ray tracing equations. Velocities and their first and second order spatial derivatives in the 3-D region were defined by the coefficients of cubic spline interpolators between grid points. The 3-D region was patched into a 1-D, radially symmetric Earth model at 90 km. depth. The 1-D Earth model was the 1 Hz., isotropic PREM of Dziewonski and Anderson (1981). PREM was first flattened using the transformations described by Müller (1971). The  $\Pi$  elements of eq. (6) were

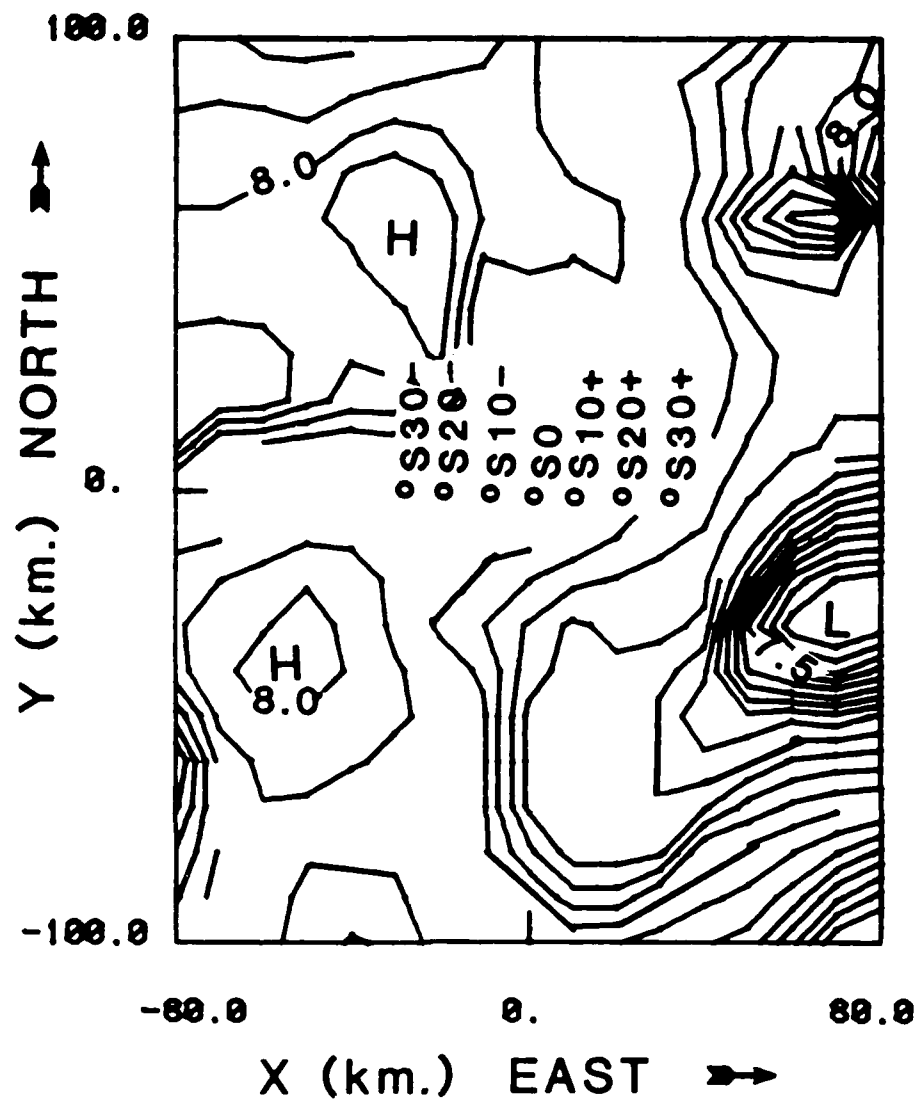


Figure 4. P velocity contours in a horizontal plane at 90 km. depth in the 3-D model for central California by Zandt (1981). Also shown are the projections of source locations used in propagation experiments at teleseismic range.

then computed using a fast algorithm in which the quantities  $\frac{dX}{dp}$  and  $X$  are given by a analytic formulae summed over thick, vertically inhomogeneous layers (Červený and Janský, 1983).  $\Pi$  was determined at the ray end points in the receiver region by propagator multiplication. The matrices  $P^R$ ,  $Q^R$  needed to evaluate eq. (10) are given by the 2 x 2 sub-matrices of  $\Pi$ ,  $\Pi_{22}$  and  $\Pi_{12}$  respectively. Focussing/defocussing effects of the structure were calculated at teleseismic range for the variations in azimuth and variations in lateral source location shown in Figure 4.

#### *5.1.1 Effect of varying azimuth at constant source location*

Figure 5 shows the results of beam summation for a teleseismic P wave from an explosive source embedded in the Zandt (1981) model. At source location  $S_0$ , seismograms were computed at  $70^\circ$  for eight different azimuths. In each column of Figure 5, the amplitudes predicted in different pass bands are shown. The broadband pulse was that obtained using the source-time function of Madariaga and Papadimitriou (1985) in a frequency band between 0.03 to 4 Hz. Amplitudes are scaled to the maximum peak to peak amplitude observed at the  $101^\circ$  azimuth. Amplitude variations are of the order of two and travel time variations on the order of several tenths of a second. The travel time variations are consistent with the focussing/defocussing effects -- large amplitudes correlate with slow travel times and small amplitudes correlate with fast travel times.

Note that even in an expanded time scale, it would be difficult to accurately measure the small travel time fluctuations associated with this model. In Figure 5, the negative peak of the short period record having an amplitude of 100 units lies just to the right of the reference line in the center column. In the record having 45 units amplitude, this negative peak coincides or lies just to the left of



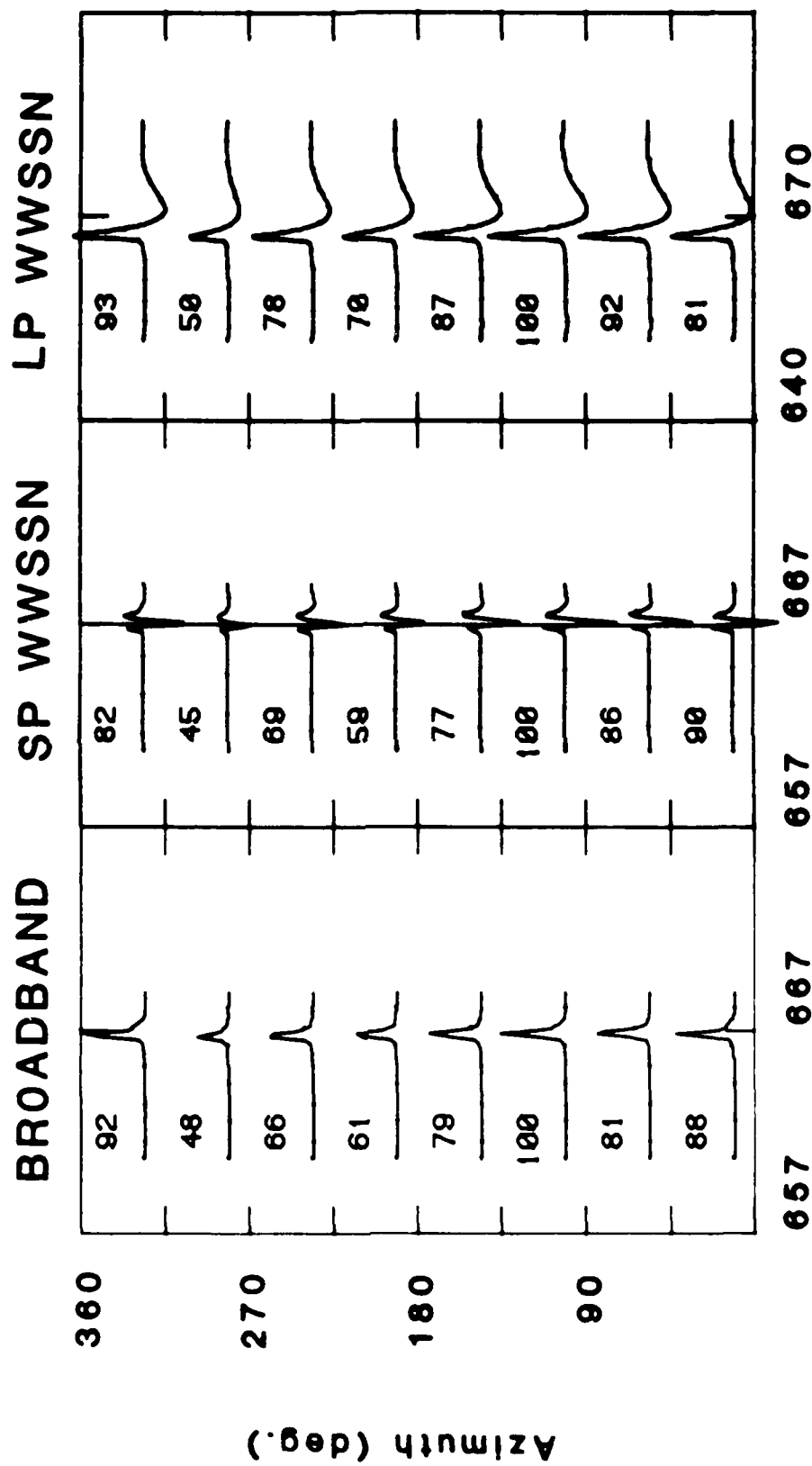


Figure 5. Synthetic seismograms constructed by superposition of Gaussian beams for stations at  $70^{\circ}$  distance and variable azimuths from an explosive point source at a constant location S0 in Figure 4 at 9.6 km depth.

the reference line. These small differences in arrival time do not bode well for any attempt to include amplitude variations with travel time variations in an inversion for velocity structure using real data.

The largest amplitudes correlate with azimuths in which the beams sample a low velocity anomaly to the southeast of source S0. This anomaly is a significant feature in both layers 3 and 4 of the Zandt model, persisting over 50 km of depth in the model. Zandt interprets this feature as a NW-SE trend of lithospheric thinning associated with a fault zone that includes the Calaveras, Rogers Creek, Maacama, and Lake Mountain faults.

#### *5.1.2 Effect of varying source location at constant azimuth*

For a fixed azimuth, and variations in source site from positions S30- to S30+ (Figure 6), amplitude variations are small. This reflects the smaller differences in structure between the regions sampled by the beams compared to those in the azimuthal experiment. The velocity anomalies in the deeper layers are broad features having scale lengths of 50 km or more. The anomalies in the shallower, crustal layers have smaller scale lengths, but the crustal layers are thin compared to the total thickness of the model and the beams spend much longer time in the thick layers 3 and 4. Thus the broad scale lengths of the anomalies in layers 3 and 4 have the greatest influence on amplitudes. This is consistent with the large variations in amplitude shown in the azimuthal experiment (Figure 5) as well as with the smaller variations in amplitude due to changes in receiver location over a line having a length roughly equal to the scale length of the broad anomalies (Figure 6).

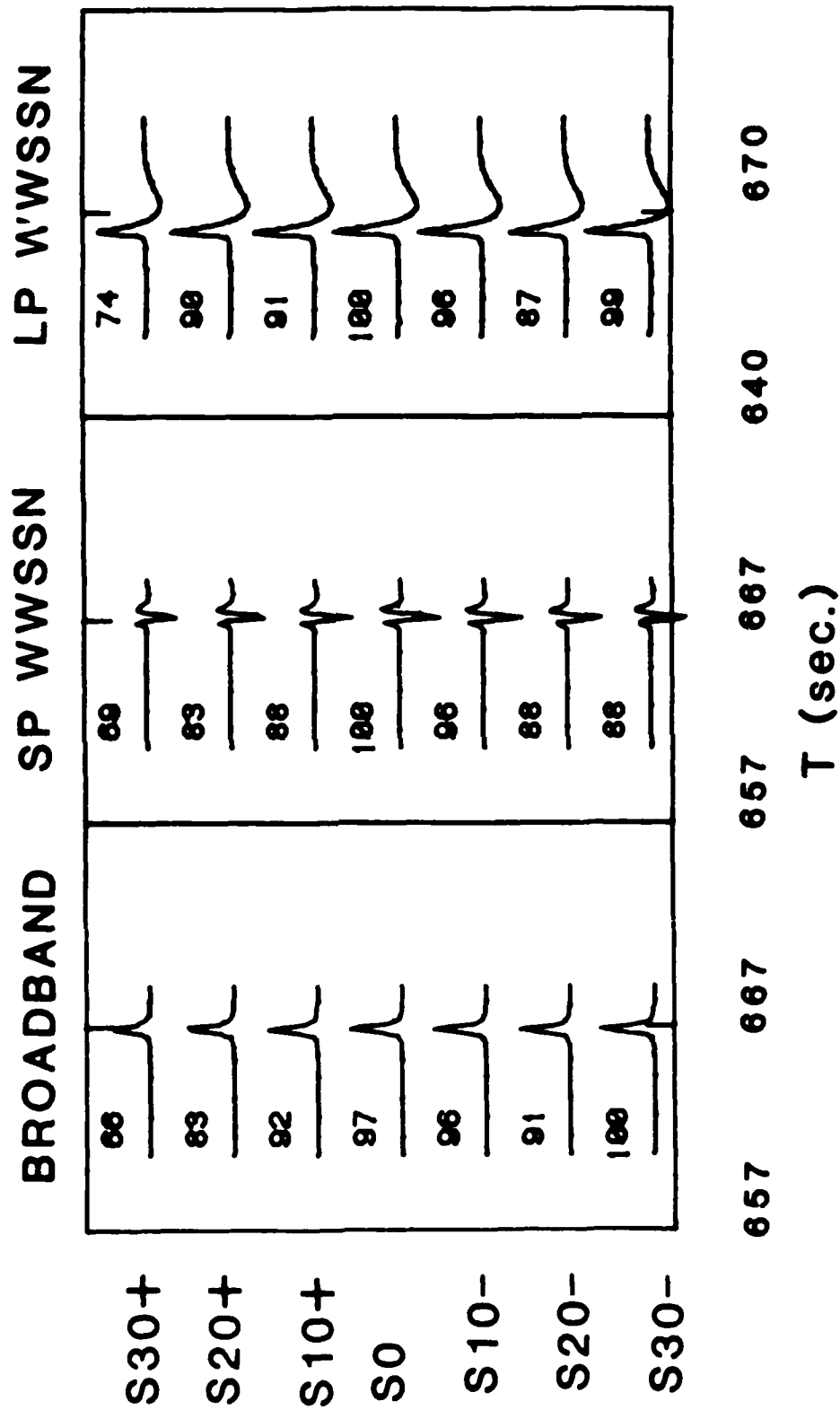


Figure 6. Synthetic seismograms at 70° distance and fixed azimuth for sources at 9.8 km depth and epicentral locations S30+ to S30- shown in Figure A

### *5.1.3 Frequency independence and its implications for treaty verification*

The relative amplitudes in Figures 5 and 6 are nearly independent of the frequency band of observation. This result has important consequences for the yield estimation of underground nuclear explosions by measurements of classical body wave magnitudes,  $m_b$ , versus broader band measurements of radiated energy in the time and frequency domain. If deep seated, broad scale length (50km and greater), velocity anomalies of 2% or more are a common occurrence in the upper mantle of the Earth, they will act to focus and defocus body waves over a broad frequency band. The focussing and defocussing caused by these broad anomalies will be independent of frequency and will thus introduce a scatter in broader band measures of radiated energy which will be equivalent to that seen in the narrow band  $m_b$  measurement. Focussing and defocussing by structure in the source region will also affect the coda of P waves if a portion of this coda is generated in the receiver region. These effects may help explain why broader band and integrated coda measures of body wave energy often do not exhibit any less scatter than classical  $m_b$  measurements. The broadband and coda magnitudes that exhibit the least scatter typically have 0.15 to 0.2 standard deviation in units of logarithm of energy flux rate over source or receiver arrays having apertures of 200 km. (Bullitt and Cormier, 1984). This corresponds to a factor of 1.5 to 2 variation in the amplitudes of particle velocity, similar to that seen in the synthetic seismograms of Figures 5 and 6. These results suggest that knowledge of the broader scale length velocity anomalies beneath source and receiver sites may be useful in correcting and reducing the scatter in magnitude estimates and hence the uncertainty in yield estimates of nuclear tests.

The frequency independence of the amplitudes calculated in the Zandt model is a characteristic of ray-theoretically predicted amplitudes. It suggests

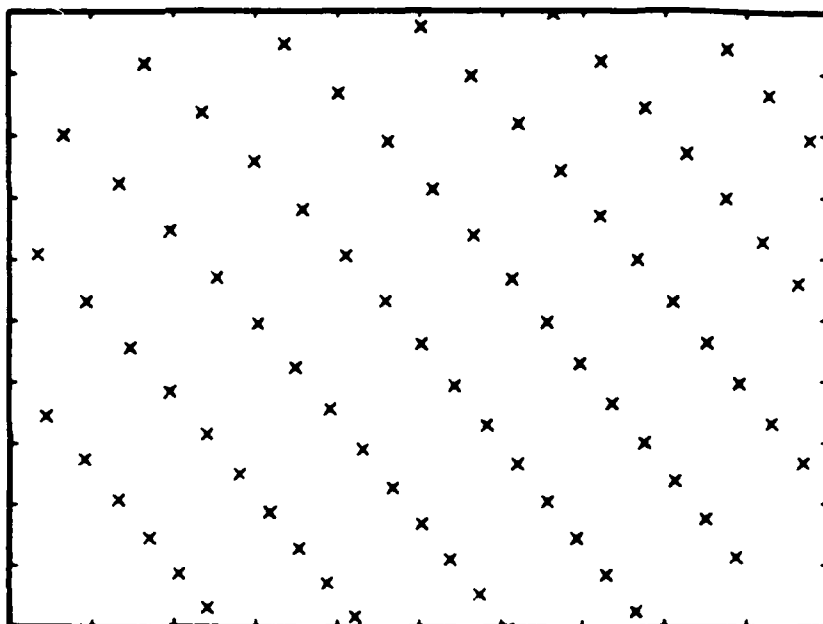
that the Gaussian beam synthesis should not be necessary in order to accurately calculate amplitude variations due to this receiver structure. There are no caustics in this example and there is no particular advantage to using Gaussian beam superposition over asymptotic ray theory, other than exploiting the paraxial estimation of travel time. Additional evidence of why beam superposition in this example reproduces simple ray theory is illustrated in Figures 7. Ray densities (Figure 7) within the vicinity of a receiver can accurately predict the amplitude observed at that receiver. Amplitude is nearly inversely proportional to the square root of beam density, consistent with the calculation of the geometric spreading by ray tube area.

All combinations of sources and receivers produce ray densities that are similar in form to Figure 7, i.e., uniform over broad regions surrounding each receiver, with no evidence of multipathing. This result is identical to that obtained by Comer and Aki (1982). They found that multipaths are not generated even when the intensity of anomalies in the Zandt model are doubled. Multipathing, however, depends on the scale length of anomalies as well as intensity. This is emphasized by the results obtained with the second model investigated.

## 5.2 A RANDOM MODEL

The second model was one generated by perturbing a 1-D model at 10 to 20 km grid points in horizontal planes with a rms velocity fluctuation of 0.8% (McLaughlin and Anderson, 1985). Unlike the Zandt model, this model introduced caustics and multipaths at teleseismic range. This made it essential to use Gaussian beams rather than asymptotic ray theory (ART) to synthesize seismograms at receivers in the vicinity of caustics. ART evaluates the superposition integral of eq. (10) by a stationary or saddle point approximation. The stationary phases occur at the discrete rays that solve the two point ray

## LARGE AMPLITUDE STATION



## SMALL AMPLITUDE STATION

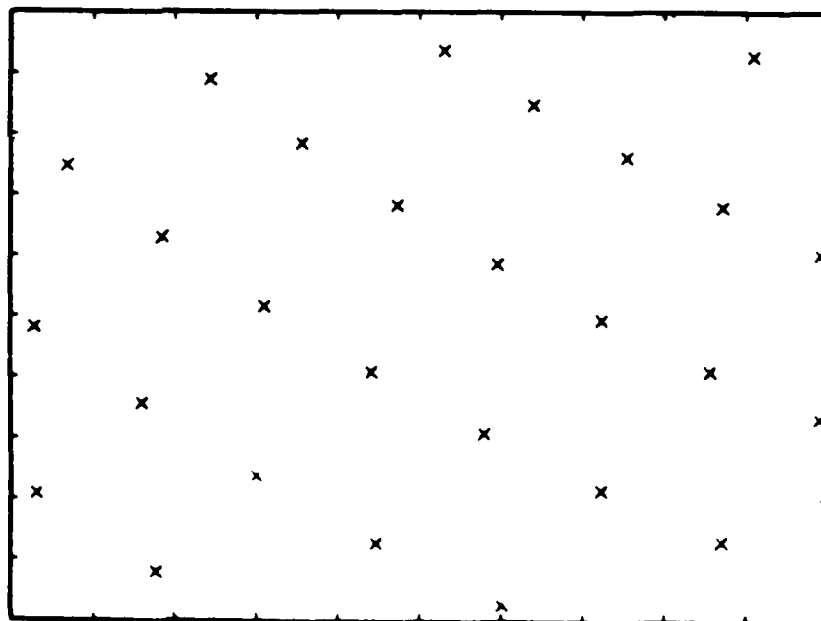


Figure 7. The end points of rays at the surface of the earth at  $70^\circ$  at the highest and lowest amplitude stations (azimuths  $101^\circ$  and  $281^\circ$  respectively) in the experiment shown in Figure 5. The  $1000 \times 1000$  km. region of end points shown here approximately bounds the region in which decay of Gaussian beams is less than  $e^{-1}$  at 0.03 Hz.

tracing problem between source and receiver, leading to amplitudes proportional to factor  $\frac{1}{\sqrt{\det \mathbf{Q}^R}}$ . This factor approaches infinity near the caustic surfaces defined by  $\det \mathbf{Q}^R = 0$ . The superposition integral and its integrand, however, remain regular at caustics for a generalized, complex  $\mathbf{M}$  matrix (Červený et al., 1982; Červený, 1985a,b).

### 5.2.1 *Effect of varying source location at constant azimuth*

Figure 8 shows contours of velocity at the bottom of the random model and the location of sources in a variable source experiment. The velocity contours have been left unlabeled and are shown only to illustrate the dramatically different scale lengths of velocity fluctuation in this model compared to the Zandt model. At a constant azimuth, the amplitude fluctuations (Figure 9) due to variations in source location are both larger and occur more rapidly than those seen in the Zandt model (Figure 6). This reflects the fact that the smallest scale length of velocity fluctuation (10 km.) roughly equals the spacing of source points. Greater frequency dependence of the amplitudes is also seen. This is due, in part, to the presence of caustics in the vicinity of the receivers for some of the source-receiver paths. Figure 10 is a plot of ray end points, illustrating the development of one of these caustics in the vicinity of the 70° station for a source at location S10-. A triplicated zone of end points can be seen, which is elongated along a narrow azimuthal zone. Rays having end points within this zone are found to have a one unit advance in their KMAH index, indicating that these rays have passed through a caustic once. A receiver located within this zone of triplicated end points is likely to observe some phase distortion in its waveform because some of the beams that contribute to the superposition integral will have a  $-\frac{\pi}{2}$  phase shift. This phase distortion is

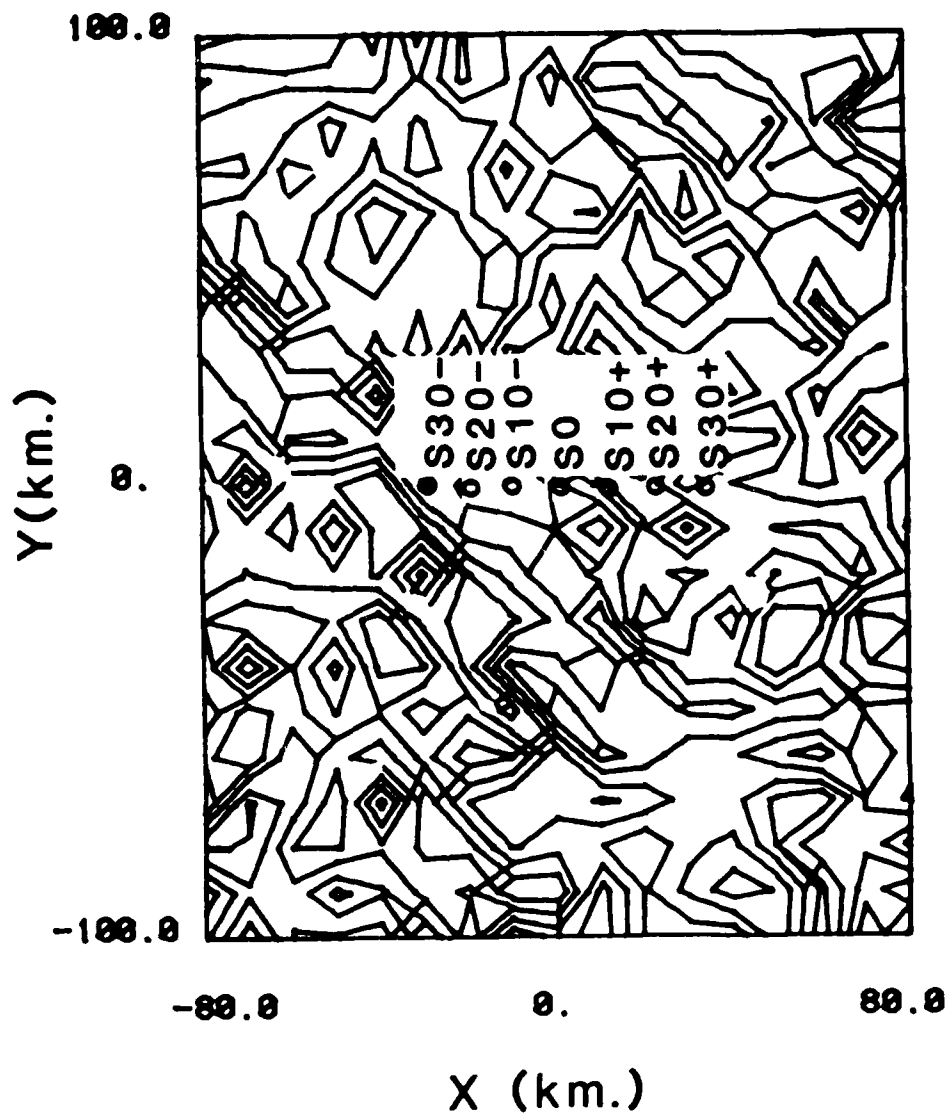


Figure 8. P velocity contours in a horizontal plane at the bottom of a model constructed by adding a 0.8% random perturbation to the velocities of a 1-D model. Perturbations were assigned at 10 to 20 km. spaced grid points in the horizontal plane. The contour interval is 0.05 km/sec, which is the same as that shown in Figure 4. The epicentral location of sources S30- to S30+ at 9.6 km. depth are projected onto this plane.



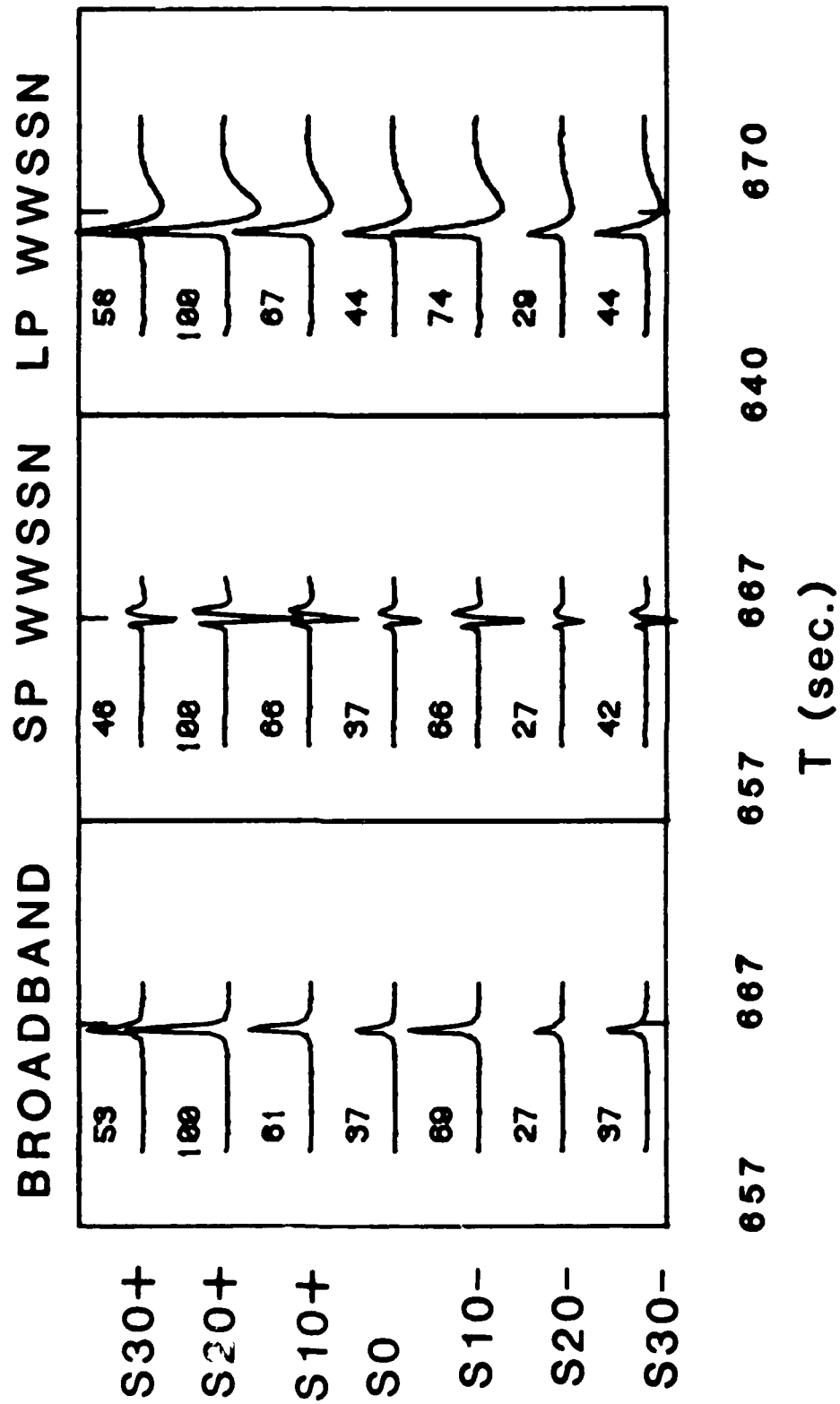


Figure 9. Broad band, short period, and long period synthetic P waves at 70° distance for the sources and random model shown in Figure 8. The azimuth of the station was held constant.

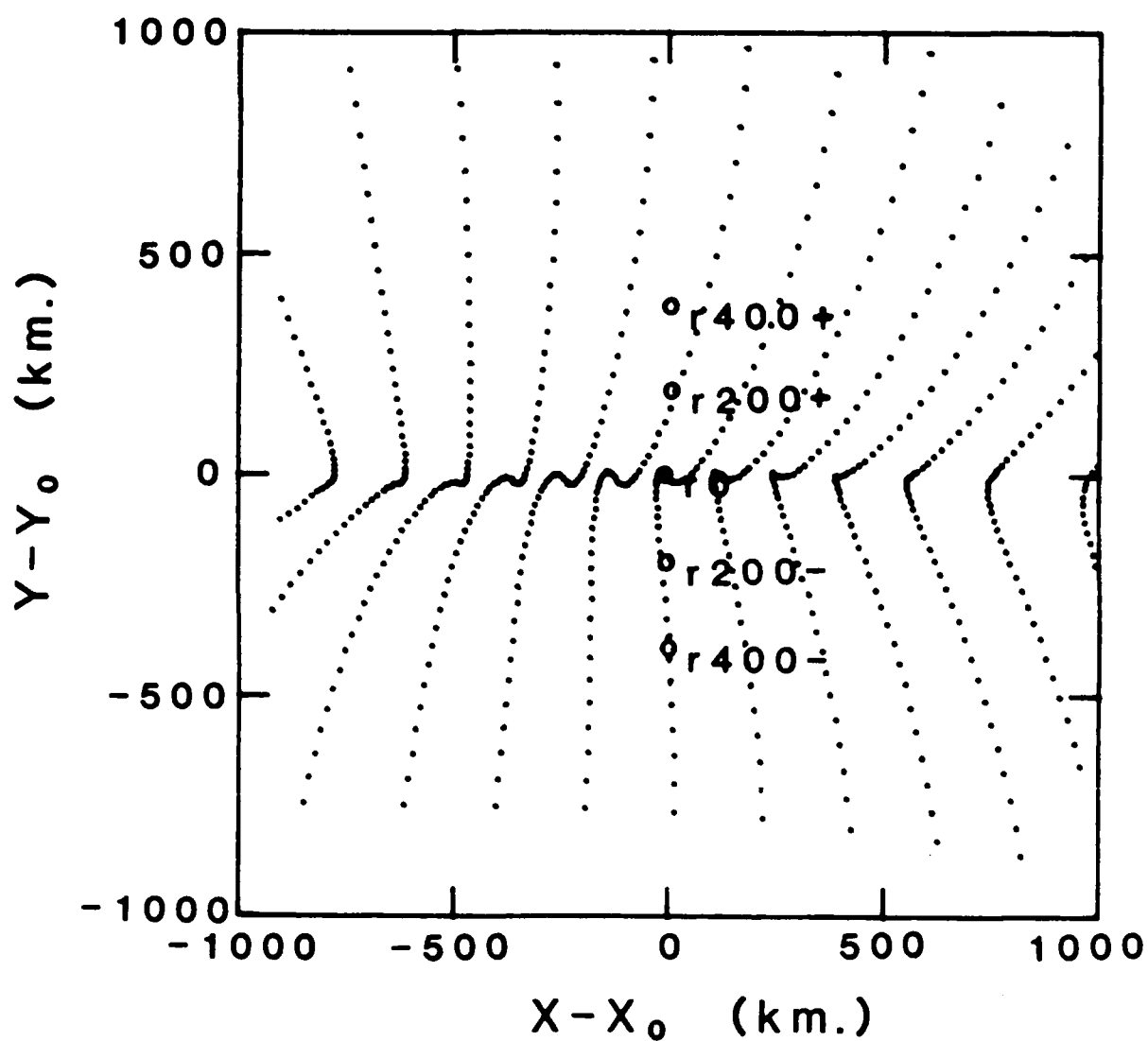


Figure 10. Ray end points near a station at  $70^\circ$  distance from source  $S_{10-}$  in the random model shown in Figure 8. The locations of a profile of receivers in the vicinity of a caustic intersection is given by the labeled points  $r_{400-}$  to  $r_{400+}$ .

difficult to observe in synthetics calculated for a profile of stations r400- to r400+ shown in Figure 11. The phase distortion appears as small change in the rise time of the broadband pulse at station r0. The small negative first break, best visible on the broadband pulse at r0, is not due to the phase shifted beams, but rather due to the unique interference effects of this particular beam pattern. The largest effects to be observed on waveforms might be expected on the short period instrument. The highest frequency band would have the highest per cent contribution from beams within the triplicated region at r0 because beams more distant from r0 would suffer a stronger exponential decay. No substantial modifications, however, are seen in the short period waveform of station r0. Comparison of amplitudes in different frequency bands in Figure 11 now shows substantial frequency dependent effects. Long period amplitudes vary only about half as much as short period and broad band amplitudes. A much broader area of beams contribute to the long period response, smoothing over the effect of the caustic region near station r0.

Although the random model was constructed to simulate the amplitude variations seen across arrays of sources or receivers having apertures of the order of 100 km (McLaughlin and Anderson, 1985), it does not predict the large variations in short period in amplitudes seen over much smaller receiver spacings such as the 7 km. aperture subarrays of NORSAR (e.g., Thomson, 1983). A random layer, having the same statistics and thickness as that placed beneath the source, can also be placed beneath the receiver array, but the combined model would still be unable to reproduce the 40% variations in amplitude commonly seen across the NORSAR subarrays. Clearly, smaller scale lengths of velocity fluctuation, as well as multiple scattering are necessary to explain the fluctuations observed over smaller aperture arrays. Modeling of the effects of smaller scale lengths was not possible in this study because the asymptotic and paraxial approximations of the ray and beam techniques begin to breakdown at scale lengths on the order of or less than the wavelength.

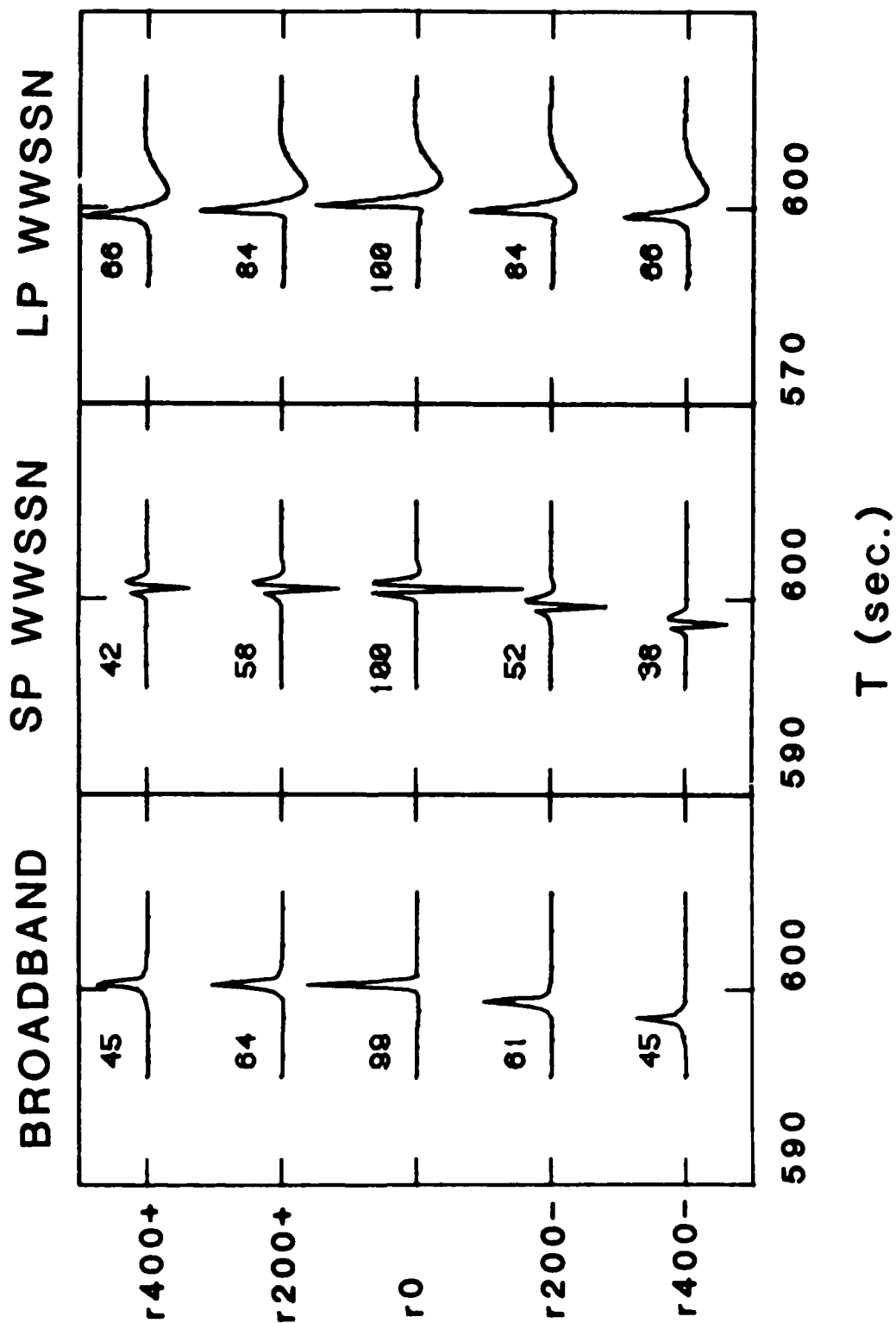


Figure 11. Synthetic P waves for the profile of stations in the vicinity of the caustic shown in the plot of ray end points in Figure 10.

### *5.2.2 The features that generate caustics and multipaths*

Exactly what feature of the random model was responsible for the thin, elongated caustic intersection shown in Figure 10 ? Since this feature is elongated along a particular azimuth, the lateral location of the structure is constrained to be along the ray paths that leave the 3-D portion of the model at this azimuth. The range of vertical take-off angles along this azimuth is also bounded by the apparent edges of the caustic intersections in the plot of ray end points. The calculation of the KMAH index can also be used to identify the particular rays that are tangent to the caustic surface at depth. By either of these methods, the rays that describe the caustic can be identified and their trajectories plotted through the 3-D region of the model. When this is done (Figure 12), it can be seen that the structure responsible for the caustic at teleseismic distance is a low velocity zone, extended in the vertical direction. The reason why such structures have been generated in this random model is that the grid spacing at which velocities were assigned was much larger in the vertical direction (30 km.) than in the horizontal direction (10 or 20 km.). Thus there occasionally will be regions of the model where negative perturbations strongly correlate between adjacent vertical grid lines, forming a vertically, elongated zone of low velocities. Similarly, elongated zones of high velocities will be formed. The surprising observation seen with this particular model is that only a very small perturbation of velocity (0.8%), with a vertical scale of 30 to 60 km., and a horizontal scale of 10 km. can generate caustics and phase advances at teleseismic distances. These caustics intersect the surface of the Earth at teleseismic range, but the areal extent of these intersections are too small to be visibly identified except for some rather subtle effects in the waveforms at a few number of stations. The generation of these caustics depends on the strength of velocity fluctuation as well as on the relation

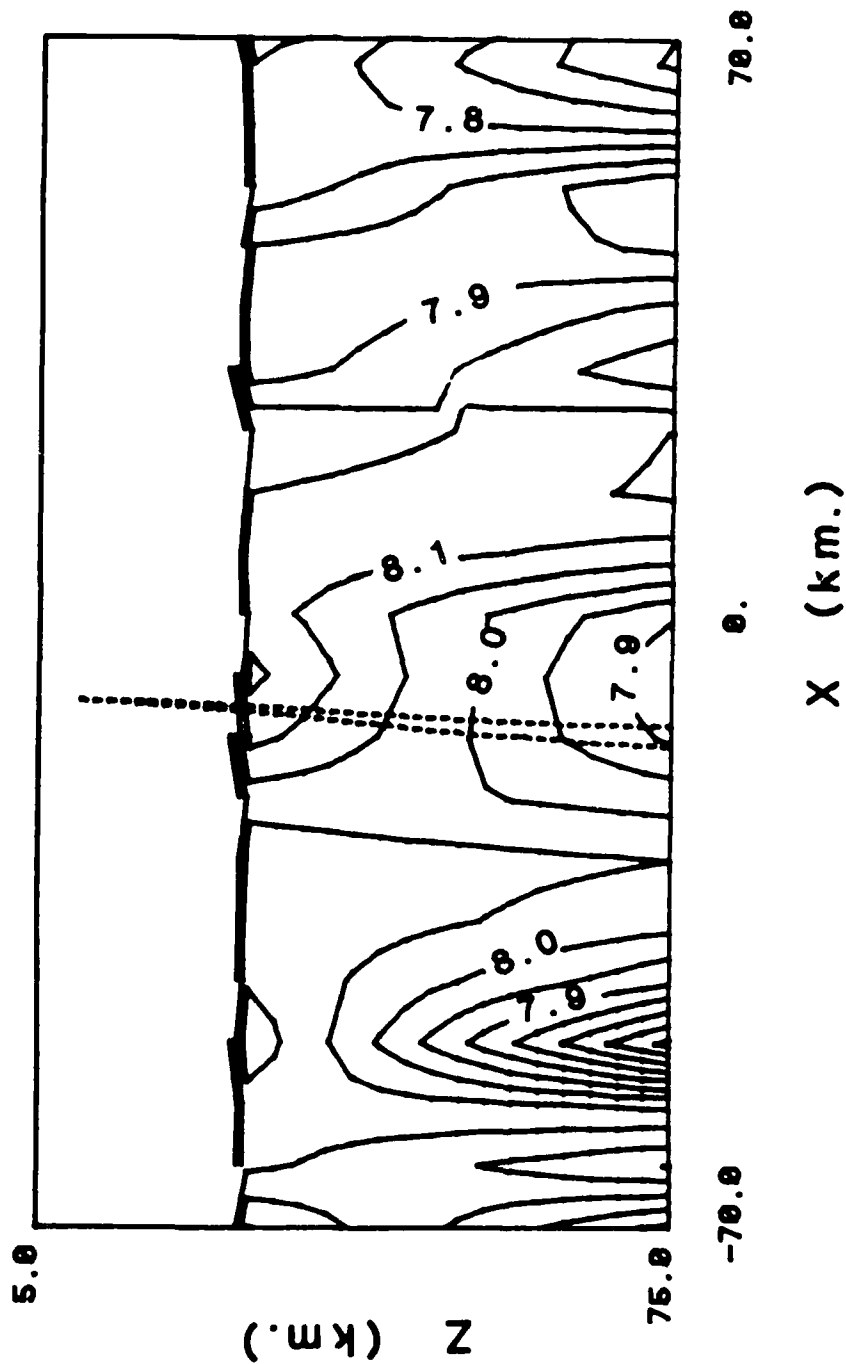


Figure 12. Trajectory of rays in the vicinity of station  $r_0$  plotted in the source region. Trajectories are projected onto a plane defined by the location of the source, receiver, and center of the earth. The two rays shown are rays that were shot at constant azimuth and bound a caustic surface formed at teleseismic range. Contours of velocities are shown at a 0.05 km/sec interval.

between the characteristic vertical and horizontal scale lengths of the 3-D model. In the example considered, the shortest scale length in the vertical direction exceeds that in the horizontal direction, a situation which is probably not the common state of crust/lithospheric structure (McLaughlin, personal communication). Some notable exceptions to this would include regions having concentrations of intrusive pipes and plumes. The results of the single modeling experiment described here suggest that some distributions of heterogeneity would produce unacceptably large effects on teleseismic waveforms. One such effect, suggested in the example shown in Figure 11, is that the first motions of the P waves from explosive, isotropic sources might be interpreted to be dilatations rather than compressions in certain narrow regions surrounding a caustic. The fact that few, if any, dilatations have been documented in the P waves recorded from underground explosions may be evidence that the particular structure that generates these caustics is a highly uncommon feature of the Earth's crust and upper mantle. From this example, it is clear that forward modeling of the effects of very general distributions of heterogeneities will be useful in defining the "heterospectrum" of the lithosphere. (The heterospectrum is a term adopted by Wu (1986) to embrace both the the strength of velocity fluctuation and its three-dimensional spatial spectrum).

### 5.3 VALIDITY OF THE RESULTS

All of the example seismograms were calculated by superposition of Gaussian beams. The accuracy of this technique depends both on the validity of using the first term in an asymptotic solution to the elastodynamic wave equation and making a Taylor expansion of the complex phase about the central ray (the paraxial approximation). It is thus appropriate to question

whether the 3-D models of velocity discussed in this paper have exceeded the domains of validity of these approximations. Validity constraints in continuous media have been formulated by Beydoun and Ben-Menahem (1985) and Červený (1985b). White et al. (1988) have considered problems encountered with continuous media as well with boundary interactions. The simplest constraints to check are those related to the asymptotic expansion, which assumes decoupling of P and S waves to zeroth order and neglect reflections and conversions by regions of strong gradient. These constraints require that wavelength be much less than quantities such as  $\frac{v}{||\nabla v||}$  and  $\frac{\rho}{||\nabla \rho||}$  (Kravtsov and Orlov, 1980; Beydoun and Ben-Menahem, 1985), where  $v$  and  $\rho$  are velocity and density respectively, and  $||\cdot||$  denotes vector length. Both the Zandt model and the random model satisfy this constraint throughout the frequency band 0.03 to 4 Hz.

Constraints on the validity of the paraxial approximation and the beam superposition have been cast in terms of the real and imaginary parts of the  $\mathbf{M}$  matrix and distance from the central ray (Beydoun and Ben-Menahem, 1985; Červený, 1985b). In order to see if these constraints are obeyed everywhere along a beam, the  $\mathbf{M}$  matrix must be known everywhere along the central ray associated with that beam. At any point  $O'$  along the central ray,  $\mathbf{M}(O')$  can be found by using the  $\Pi$  matrix to back propagate the complex  $\mathbf{M}(O_s)$  matrix selected at the end point  $O_s$ . Although these constraints were not calculated in the two examples described, a check on the overall validity of the beam superposition was taken from the results of reciprocal experiments, in which the positions of sources and receivers were reversed. Examples of this test in 2-D media are given by Nowack and Aki (1984) and Müller (1984). Reciprocal experiments were conducted in the form of allowing a plane wave to be vertically incident on the 3-D models. The plane wave was expanded into



Gaussian beams by the procedure described by Červený (1982), and the wavefield was calculated at receivers on the surface of the 3-D models. Such an experiment was conducted on the random model (McLaughlin and Anderson, 1985) and on a model having a heterospectrum similar in scale length and velocity fluctuation to the Zandt model (Nowack and Cormier, 1985). Although the geometry was not precisely reciprocal and waveforms were not directly compared, both experiments produced intensities and coherency of amplitude fluctuations similar to those produced by the teleseismic experiments.

### Conclusions

The theory and examples discussed in this paper have shown how the propagator matrix of the dynamic ray tracing equations,  $\Pi$ , can be exploited to connect 3-D to 1-D portions of a model. Both plane wave and point source initial conditions are required to specify the elements of the propagator matrix. Thus both plane wave and point source solutions are generally useful for all asymptotic methods of body wave synthesis and not just for Gaussian beams.

An investigation was made of the effect of 3-D structure in the source region on the focussing and defocussing of teleseismic P waves. These effects were observed with two different models as a function of source location within the 3-D model and of azimuth at the source. In a 3-D model, block inverted from teleseismic travel times, ray theoretical amplitudes matched those predicted from superposition of Gaussian beams. In this model, the characteristic scale lengths of the most intense velocity fluctuations (4%) were on the order of 50-100 km. in the source region. This model produced a factor of two fluctuation in amplitude, associated with fluctuations in travel time on the order of several tenths of a second. Amplitude variations due to variations in source location were small over location variations that were small with respect to the scale length of velocity fluctuation. All amplitude variations were

nearly independent of frequency across the body wave band of 0.03 to 4 Hz. The frequency independence of amplitude variations across the body wave band may have important implications for removing the effects of azimuthal amplitude variations due to 3-D structure beneath nuclear test sites. Broad scale length, deep seated structure can affect short period as well as broad band and coda measures of radiated seismic energy. Its effects, however, may be easily correctible if a 3-D model of the source region is known from block inversion of travel time residuals. A resolvable block size of about 20 km. may be all that is necessary to formulate corrections based on azimuth of teleseismic station and source location within a test site.

Calculations with a random velocity model demonstrated that a smaller intensity of velocity fluctuation (0.8%) can produce even larger amplitude variations if the smallest scale length of fluctuation is on the order of 10 km. The random model was constructed such that the smallest scale length of velocity fluctuation was shorter in the horizontal direction than in the vertical direction. At teleseismic range, this model generated isolated caustics, which were elongated along the azimuth of approach. The waveform distortion associated with these caustics was small. The fact that the caustics were generated at all by such mild 3-D perturbations is significant. It suggests that this type of synthetic modeling may be useful in limiting some of the attributes of the heterospectrum of the Earth's lithosphere.

### **Acknowledgements**

Discussions with Bob Nowack and Keith McLaughlin were particularly helpful in developing both the theoretical and observational results of this study. Bob provided a program that integrated the dynamic ray tracing equations through 3-D models parameterized by cubic splines. Keith generated

the random 3-D models and provided insightful comments on the results of the waveform calculations. This research was supported by the Advanced Research Projects Agency of the Department of Defense and was monitored by the Air Force Geophysics Laboratory under contract #F19628-85-K-0031 and by the National Science Foundation under contract #EAR-85-18151.

## References

- Aki, K., Christoffersson, A., and Husebye, E.S., 1976. Determination of three-dimensional seismic structures of the lithosphere, *J Geophys Res.*, **82**, 277-296.
- Beydoun, W.B., and Ben-Menahem, A., 1985. Range of validity of seismic ray and beam methods in general inhomogeneous media -- I. and II. *Geophys J. R. astr. Soc.*, **82**, 207-262.
- Bullitt, J.T., and Cormier, V.F., 1984. The relative performance of  $m_b$  and alternative measures of elastic energy in estimating source size and explosion yield, *Bull. Seism. Soc. Am.*, **74**, 1863-1882.
- Červený, V., Molotkov, I.A., and Pšenčík, I., 1977. *Ray Method in Seismology*. Charles University, Prague.
- Červený, V., and Eron, E., 1980. The ray series method and dynamic ray tracing systems for 3-D inhomogeneous media, *Bull. Seism. Soc. Am.*, **70**, 47-77.
- Červený, V., Popov, M.M., and Pšenčík, I., 1982. Computation of wavefields in inhomogeneous media - Gaussian beam approach, *Geophys. J. R. astr. Soc.*, **70**, 102-128.
- Červený, V., 1982. Expansion of a plane wave into Gaussian beams, *Stud. Geophys. Geod.*, **26**, 120-131.
- Červený, V., and Pšenčík, I., 1983. Gaussian beams and paraxial ray approximation in three-dimensional elastic inhomogeneous media, *J. Geophys.*, **53**, 1-15.
- Červený, V., 1983. Synthetic body wave seismograms for laterally varying structures by the Gaussian beam method, *Geophys. J. R. astr. Soc.*, **73**, 389-426.

- Červený, V., and Janský, J., 1983. Ray amplitudes of seismic body waves in inhomogeneous, radially symmetric media, *Stud. Geophys. Geod.*, **27**, 9-18.
- Červený, V., 1985a. The application of ray tracing to the propagation of shear waves in complex media, in *Seismic Exploration*, eds. Treitel, S., and Helbig, K., Vol. on Seismic Shear Waves, ed. Dohr, G., Geophysical Press, pp. 1-124.
- Červený, V., 1985b. Gaussian beam synthetic seismograms, *J. Geophys.*, **58**, 44-72.
- Chapman, C.H., and Drummond, R., 1982. Body-wave seismograms in inhomogeneous media using Maslov asymptotic theory, *Bull. Seism. Soc. Am.*, **72**, 5277-5917.
- Comer, R. and Aki, K., 1982. Effects of lateral heterogeneity near an earthquake source on teleseismic raypaths, *Earthquake Notes*, **52**, no. 1.
- Cormier, V.F., and Spudich, P., 1984. Amplification of ground motion and waveform complexity in fault zones: examples from the San Andreas and Calaveras faults, *Geophys. J. R. astr. Soc.*, **79**, 135-152.
- Dziewonski, A.M., and Anderson, D.L., 1981. Preliminary reference earth model (PREM), *Phys. Earth Planet. Inter.*, **25**, 297-356.
- Dziewonski, A.M., 1984. Mapping of the lower mantle: determination of lateral heterogeneity in P velocity up to degree and order 6, *J. Geophys. Res.*, **89**, 5929-5952.
- Haddon, R.A.W., and Buchen, 1981. Use of Kirchhoff's formula for body wave

- calculations in the earth, *Geophys. J. R. astron. Soc.*, **67**, 587-598.
- Kravtsov, Y.A., and Orlov, Y.I., 1980. Limits on the applicability of the method of geometric optics and related problems, *Sov. Phys. Usp.*, **23**, 750-762.
- Madariaga, R., 1984. Gaussian beam synthetic seismograms in a vertically varying medium, *Geophys. J. R. astr. Soc.*, **79**, 589-612.
- Madariaga, R., and Papadimitriou, P., 1985. Gaussian beam modelling of upper mantle phases, *Ann. Geophys.*, **3**, xxx-xxx.
- McLaughlin, K.L., and L.M. Anderson, 1987. Stochastic dispersion of P waves due to scattering and multipathing, *Geophys. J. R. astr. Soc.*, **89**, 933-964.
- Müller, G., 1971. Approximate treatment of elastic body waves in media with spherical symmetry, *Geophys. J.*, **23**, 435-449.
- Müller, G., 1984. Efficient calculation of Gaussian-beam seismograms for 2-D inhomogeneous media, *Geophys. J. R. astr. Soc.*, **79**, 153-166.
- Nowack, R. and Aki, K., 1984. The 2-D Gaussian beam method: testing and application, *J. Geophys. Res.*, **89**, 7797-7819.
- Nowack, R.L., and Cormier, V.F., 1985. Computed amplitudes using ray and beam methods for known 3-D structures (abstract), *EOS, Trans. Am. Geophys. Un.*, **66**, 980.
- Scott, P., and D.V. Helmberger, 1983. Applications of the Kirchhoff-Helmholtz integral to problems in seismology, *Geophys. J. R. astr. Soc.*, **70**, 237-254.
- Sleep, N.E., 1973. Teleseismic P-wave transmission through slabs, *Bull. Seism. Soc. Am.*, **63**, 1349-1373.

- Thomson, C., 1983. Ray theoretical amplitude inversion for laterally varying velocity structure below NORSAR, *Geophys. J. R. Astr. Soc.*, **74**, 525-558.
- White, B.S., Burridge, R., Noriss, A., and Bayliss, A., 1986. Some remarks on the Gaussian beam summation method, *Geophys. J. R. Astr. Soc.*, submitted.
- Woodhouse, J.H., and Dziewonski, A.M., 1984. Mapping the upper mantle: three dimensional modeling of earth structure by inversion of seismic waveforms, *J. Geophys. Res.*, **89**, 5953-5986.
- Wu, R-S., 1986. Heterogeneity spectrum, wave scattering response of a fractal medium and the rupture processes in the medium, *J. of Wave-Material Interaction*, submitted.
- Zandt, G., 1981. Seismic images of the deep structure of the San Andreas Fault system, central coast ranges, California, *J. Geophys. Res.*, **86**, 5039-5052.
- Ziolkowski, R.W., and Deschamps, G.A., 1980. The Maslov method and the asymptotic Fourier transform: caustic analysis, Electromagnetics Laboratory Scientific Report No. 80-9, University of Illinois at Urbana-Champaign.

#### 4 Focusing and defocussing of teleseismic P waves ....

(Reprint of a paper by the P.I., *Bull. Seism. Soc. Am.*, 77, in press, 1987.)



**FOCUSING AND DEFOCUSING OF TELESEISMIC P WAVES BY  
KNOWN 3-D STRUCTURE BENEATH PAHUTE MESA, NEVADA TEST SITE**

By Vernon F. Cormier

\*Earth Resources Laboratory  
Department of Earth, Atmospheric, and Planetary Sciences  
Massachusetts Institute of Technology  
Cambridge, MA 02139

Submitted to the Bulletin of the Seismological Society of America

Revised 3/26/87

## ABSTRACT

The focusing and defocusing of teleseismic P waves predicted by a known (Taylor, 1983) three-dimensional structure beneath the Nevada Test Site is calculated by dynamic ray tracing and superposition of Gaussian beams. The 20 to 100 km. scale lengths of this model, having velocity fluctuations of several percent, account for a factor of three fluctuation in the azimuthal pattern of P amplitudes. Since similar sized scale lengths and intensities of velocity fluctuation are commonly resolved in three-dimensional inversions of mantle structure in other regions, focusing and defocusing of teleseismic P waves is likely to be a ubiquitous feature of every test site. Hence, network averages of  $m_b$  that weight azimuthal windows in which P energy is either focused or defocused will tend to either over or under estimate the yields of underground tests. The results obtained with a known NTS structure suggest that structural inversions having similar structural resolution may be capable of reducing 25 percent of the variance in amplitudes due to the focusing and defocusing of upper mantle structure near the source.

Assuming that scattering processes are concentrated in the crust and uppermost mantle beneath the source and receiver, the integrated energy in the P coda should be more stable than direct P because it tends to homogenize the effect of focusing/defocusing structure near the source for scattering into direct P near the source. For direct P scattering near the receiver, however, even the late coda is not capable of completely removing the effects of focusing/defocusing near the source.

## INTRODUCTION

The underground nuclear tests conducted in the Pahute Mesa region of the Nevada Test Site (Figure 1) exhibit a unique and reproducible azimuthal pattern in the amplitudes of short period P waves at teleseismic range (Lay et al., 1984). Because this pattern differs from those of tests conducted in other regions of the test site, it cannot simply be explained by either receiver effects or by variations in intrinsic attenuation along different paths in the mantle.

Evidence of tectonic release in the waveforms of long period P and S waves of large (greater than 500 kt.) Pahute events (Wallace et al., 1983, 1984), suggests that tectonic release may be the mechanism that also produces the azimuthal variation of the amplitude of short period P waves. A study by Lay et al. (1984) initially favored this explanation, but noted the difficulty in formulating a physically realizable mechanism of tectonic release that would be capable of strongly affecting short period amplitudes. The required tectonic event would have to occur nearly simultaneously with the explosion. Theoretical and model studies of the relaxation of the likely pre-stress in this region have found negligible effects on the amplitudes of short period P waves (Archambeau, 1972; Bache, 1975).

More recent studies by Lynnes and Lay (1984; 1987) and Lay and Welch (1986a) hypothesize that the azimuthal pattern of amplitudes from Pahute tests is instead caused by focusing and defocusing of P waves by three-dimensional structure in the mantle beneath the test site. The structure likely to be responsible for the strongest features of the observed focusing and defocusing is a high velocity structure in the mantle beneath Pahute Mesa. Such structure was first proposed by Spence (1974) from clusters of fast P travel times from Pahute tests to teleseismic stations. Spence's model, which qualitatively fits the observed travel time residuals, consists of a conical shaped

zone of positive velocity perturbation of 6-8 percent lying directly beneath the Silent Canyon Caldera (center marked with x in Figure 1). The high velocity perturbation extends to 190 km depth and its half width is about 50 km.

The development of techniques of inverting for three dimensional structure (Aki et al., 1977) led to attempts to better resolve the structure beneath NTS, including the the structure suggested by Spence's study (Minster et al., 1981; Montfort and Evans, 1982; Taylor, 1983). A consistent result of these studies is that the high velocity structure beneath Pahute Mesa migrates to the north as depth increases (Figure 2). The strong positive perturbation of velocities in this structure is suggested to be an enriched mafic residue resulting from intermittent melting and differentiation. The partial melt material itself is presumed to have erupted through the volcanic center of the Silent Canyon Caldera.

The structure resolved in the inversions of Minster et al. (1981) and Montfort and Evans (1982) are either too broad in scale length or too weak in percent velocity fluctuation to have much of an effect on the focusing and defocusing of teleseismic P waves. In the case of the Minster et al. model, a smoothing algorithm reduces velocity perturbations to less than 2 percent fluctuation. In the case of the Montfort and Evans model, the intent was to resolve structure over a much broader region, using larger block sizes. Hence, the approach followed by Lynnes and Lay (1984) was to find an ad-hoc structure consistent with the observed pattern of amplitudes. The resulting structure bore some resemblance to a high velocity anomaly mapped in the mantle northeast of Pahute Mesa in a travel time inversion by Taylor et al. (1983). The effects of the structure resolved in the Taylor model, however, were not directly investigated.

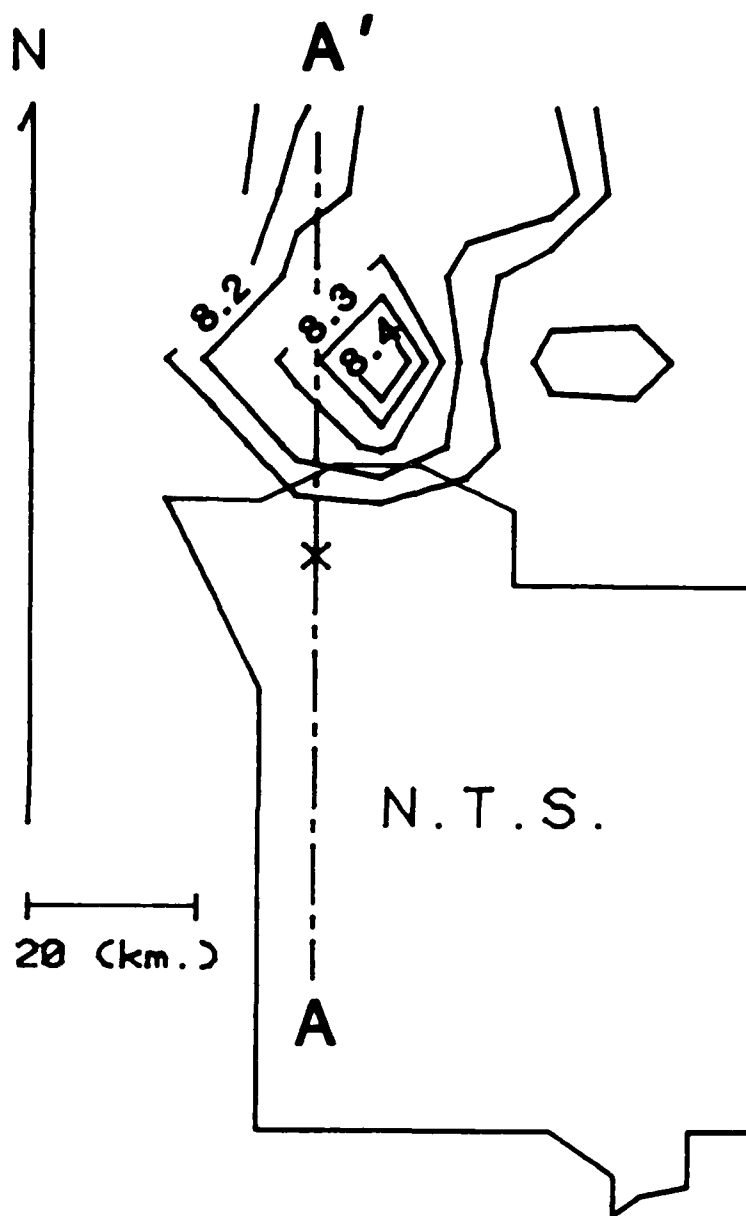


Figure 1. A representative epicenter of an underground nuclear test at Pahute Mesa is marked by the cross (x). Iso-P velocity contours at 85 km. depth are shown for a high velocity anomaly resolved in the study by Taylor (1983).

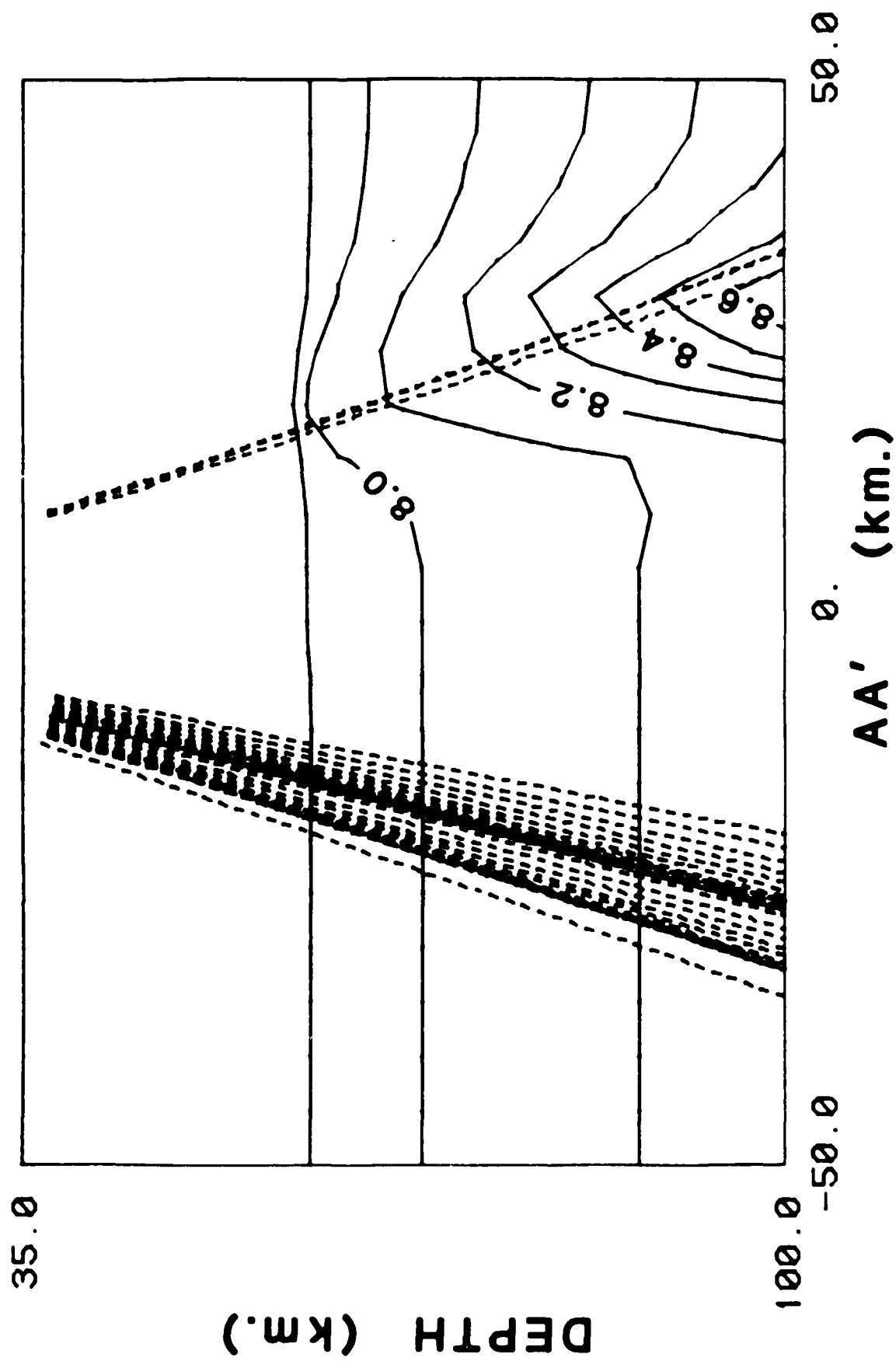


Figure 2. Iso-P velocity contours greater than 7.9 km./sec for the Taylor (1983) model along the AA' cross section shown in Figure 1. Three-dimensionally traced rays (dashed) are projected onto the cross section if their end points lie within 20 km. of the plane of the cross section.

This paper will report on the results of forward modeling of teleseismic P waves for an explosive point source placed in the Taylor (1983) model at a Pahute hypocenter. For several reasons, direct calculation of the focusing and defocusing effects of the Taylor model is relevant to reducing the uncertainties in the yield estimates of underground tests. First, the model would be representative of the best information that would likely be obtainable at foreign test sites, short of deploying dense local arrays within the test site. Comparable data needed to obtain similar resolution of structure would consist of a regional array located primarily outside the test site and a well distributed set of tests with known origin times and hypocenters. Second, the effects of a known model for the structure beneath Pahute Mesa can aid in identifying any biasing effects of focusing and defocusing on the construction of empirical yield versus  $m_b$  curves from NTS data. For example, if globally averaged  $m_b$ 's are concentrated in a narrow azimuthal band of focused or defocused energy, then yields from Pahute events will provide points to the empirical curve that are either biased toward high or low yield.

#### EFFECTS ON DIRECT P

Seismograms of teleseismic P waves were synthesized for sources in Taylor's model using the techniques described in Cormier (1986). The model was specified on a three dimensional grid by percent perturbations from a reference model. Only those perturbations were used whose diagonal elements of the resolution matrix exceeded 0.6. Continuous first and second spatial derivatives of velocity were calculated from splines under tension (Cline, 1981). Ray tracing was performed by integrating the kinematic and dynamic equations numerically in the three-dimensional region surrounding the source and analytically along the rest of the ray path in a flattened, radially symmetric earth model. Seismograms were calculated both by simple ray theory and by

superposition of Gaussian beams (Červený, 1985ab).

*Gaussian beam modeling.* Superposition of Gaussian beams was first performed in order to check whether the three-dimensional model was capable of producing any frequency dependent effects at teleseismic range. Gaussian beams remain regular at caustics and can succeed in predicting the first order effects of frequency dependence at caustics. The beam superposition also averages the effects of structural scale lengths that are small with respect to wavelength. (Here, structural scale length is taken to mean the distance between local minima and maxima of velocity perturbation.) Beam width parameters were chosen as described in Cormier (1986), which amounted to taking a plane wave superposition at the receivers with very wide Gaussian windowing.

Broadband, WWSSN short period, and WWSSN long period seismograms were synthesized for variable azimuths at a fixed receiver distance of  $60^\circ$  for a Pahute Mesa source located as shown in Figure 1. The synthetic seismograms (Figure 3) show little evidence of frequency dependence, with the relative amplitudes of waveforms in the three pass bands being nearly identical. Similar results were found in a study of a three-dimensional model having similar resolution and scale lengths of structure (Cormier, 1986). Amplitudes vary azimuthally by a factor of three, with the smallest amplitude at due north. Figures 1 and 2 show that ray paths in northerly directions will traverse a high velocity anomaly located in the mantle north of the epicenter. The associated travel time variation of several tenths of a second is too small to be easily visible in the synthetics. Note that in the center column for SP WWSSN in Figure 3, the reference line is close to the center of the trough of the waveform of the station having the 30 unit amplitude but is close to the first peak of the waveform of the station having the 100 unit amplitude. The sense of the travel time variation is consistent with focusing and defocusing: small amplitudes



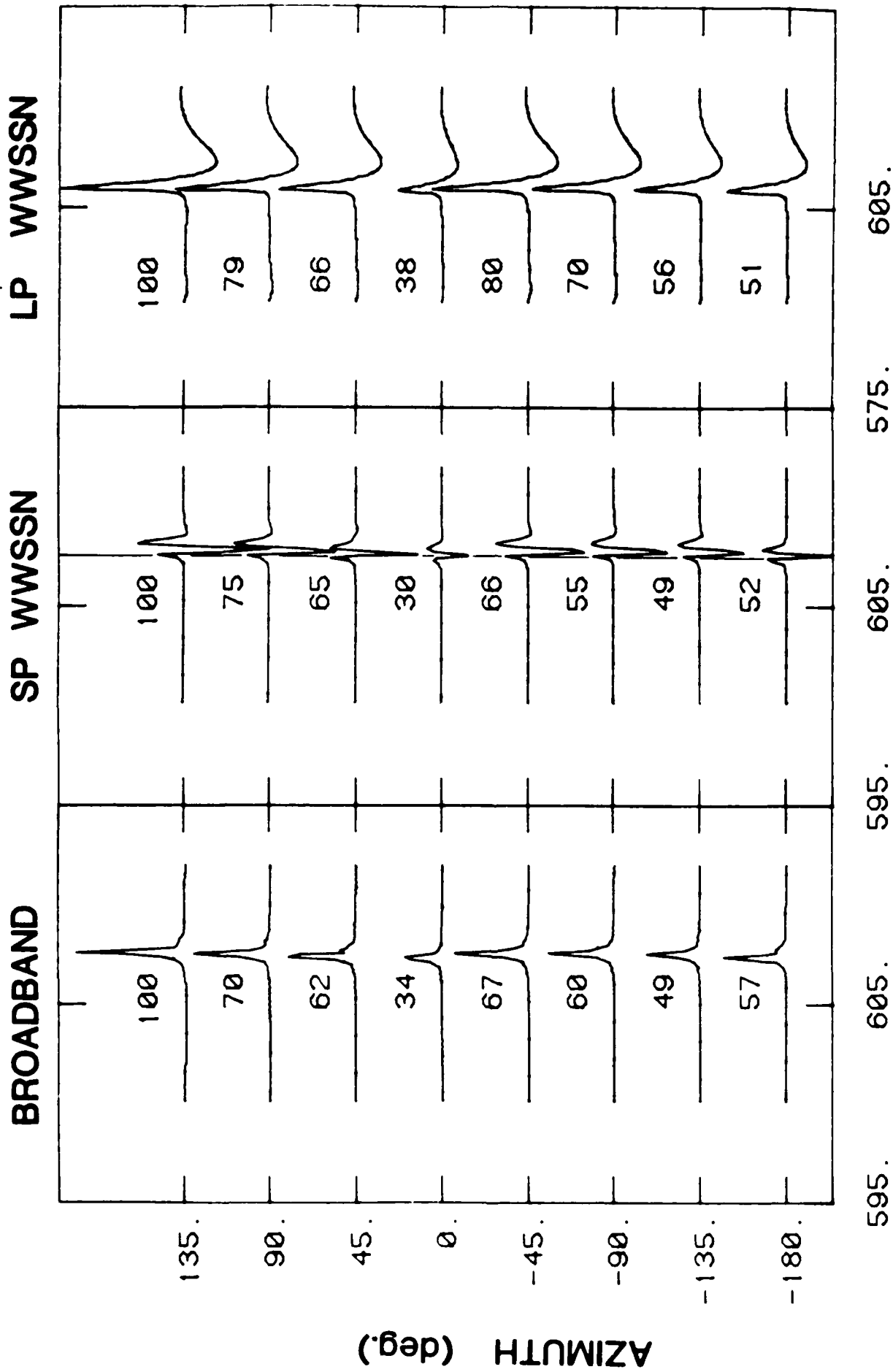


Figure 3. Teleseismic P waves synthesized by superposition of Gaussian beams for stations at 80° distance and variable azimuths for an explosive point source at 1 km depth. The source location is shown in Figure 1. The numbers alongside each seismogram are measurements of peak to peak amplitude. A reference line, from which travel time variations may be measured from the minimum trough, is shown in the short

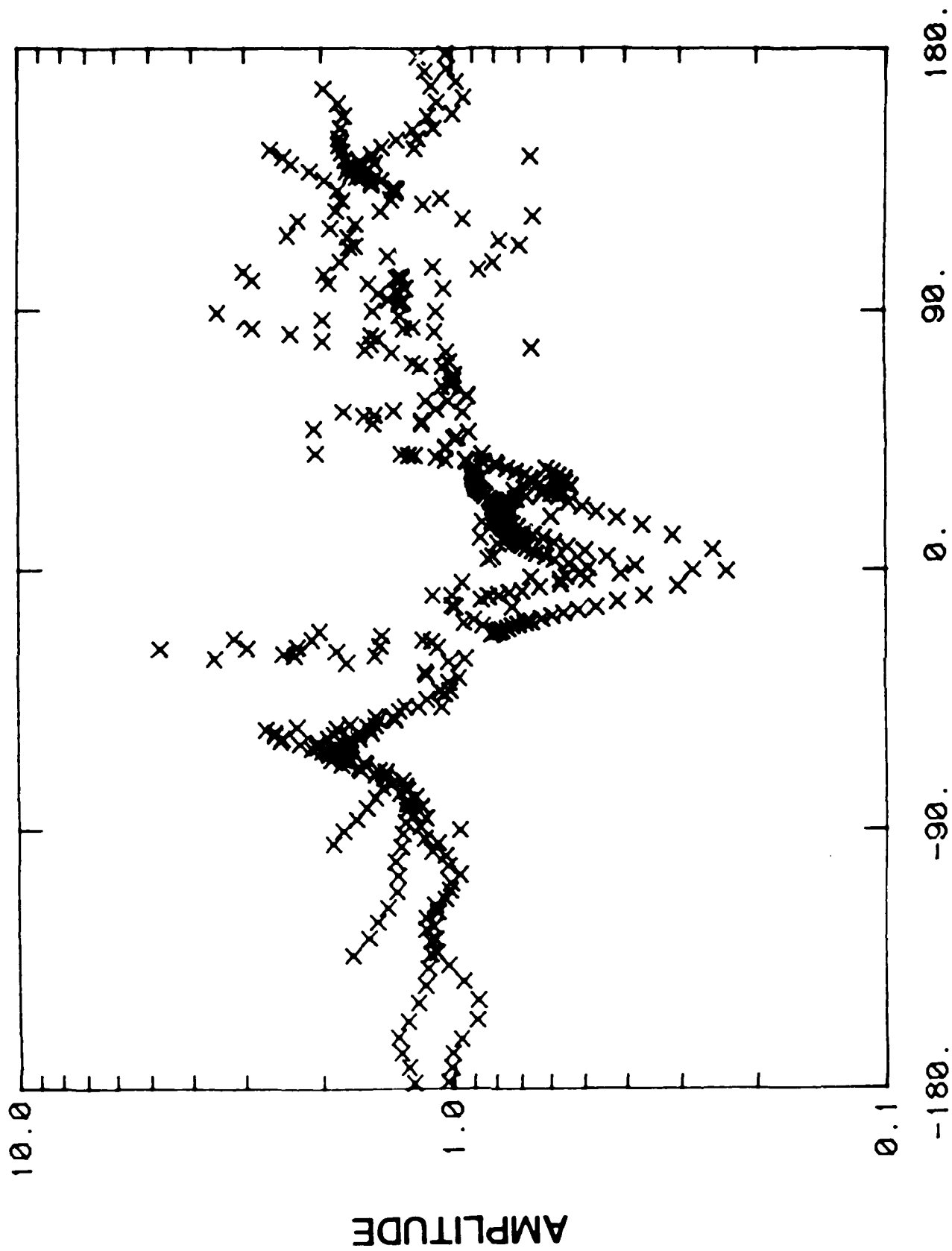
T (sec.)

correlate with fast times; large amplitudes with slow times. This correlation is discussed and shown in finer detail in following section discussing the results of ray theoretical modeling.

*Ray theoretical modeling* Since the Gaussian beam modeling exhibited little evidence of frequency dependence, it was deemed appropriate to model seismograms by ray theory. Ray theoretical amplitudes were predicted from geometric spreading calculated from the determinant of the  $Q$  matrix obtained from dynamic ray tracing (Červený, 1985b). A dense system of rays was shot at variable vertical take-off angle and azimuthal angle. The range of vertical take-off angles was chosen to correspond to great circle distances between  $35^\circ$  and  $95^\circ$ . The determinant of the  $Q$  matrix was evaluated at end points of the rays at the earth's surface. The ray theoretical amplitude is then equal to  $\frac{1}{\sqrt{\det Q}}$ . Figure 4 plots these amplitudes versus azimuth for the system of rays shot. All amplitudes were normalized for the spreading factor appropriate for a P wave at  $60^\circ$  in a radially symmetric earth. The azimuth plotted is the azimuth at the point at which a ray leaves the three-dimensional region surrounding the source.

Note the pronounced minimum in amplitudes again occurs at northerly azimuths, with more steeply dipping rays at greater distances having the smallest amplitudes. A region of larger amplitudes occurs around  $-70^\circ$  azimuth. In other azimuthal ranges, amplitudes scatter depending on the vertical take-off angle.

The large scatter around  $-30^\circ$  azimuth ( $330^\circ$  clockwise from north) is due to the presence of a caustic. The Gaussian beam synthesis did not test this azimuthal range. Calculations with other three-dimensional models obtained from block inversion of travel times and with statistically generated models find that such caustics can be easily generated by velocity perturbations as small as



### AZIMUTH (deg.)

Figure 4. Predicted amplitudes of teleseismic P waves as a function of azimuth. Amplitudes were calculated by dynamic ray tracing in the Taylor

one percent (Cormier, 1986; McLaughlin and Anderson, 1987). Tests with seismograms synthesized by superposition of Gaussian beams find only a very small amount of phase distortion in the P waves of receivers located near the caustic. This is because the class of caustic created by these models encloses a very small area on the earth's surface. This area is generally so small in the vicinity of the receiver that any phase distortion or frequency dependence in the waveforms is barely visible within the pass bands of common seismographs.

*Comparison of predicted with observed Amplitudes.* Figure 5 shows observed amplitudes of Pahute events collected by Lay et al. (1984). Note the amplitude minimum predicted by the Taylor model at northerly azimuths is qualitatively matched. There is some match of the predicted maximum near  $-70^{\circ}$  azimuth as well as of the form of the scatter between  $50^{\circ}$  to  $150^{\circ}$  azimuth. The minimum in the observed amplitudes is displaced slightly to the east of the predicted amplitudes. It appears that the high velocity anomaly in the Taylor model is placed at about the right distance from the center of Pahute Mesa, but is displaced to the west relative to the true anomaly. This may be due to ray bending in the vicinity of the source, which the inversion technique ignores. Even without any azimuthal shift in the predicted amplitudes, the predicted amplitudes can be used to correct for focusing and defocusing, giving about a 25 percent reduction in variance in corrected log amplitudes. It is interesting to note that Taylor's model predicts a similar variance reduction in travel time anomalies. This suggests that a particular model's success in reducing the variance in travel times can be taken as a rough measure of its potential success in reducing the variance in log amplitudes due to focusing and defocusing.

The strong concentration of observations around the amplitude minimum will tend to reduce the network averaged  $m_b$  of Pahute events. This effect can be alleviated by more sophisticated averaging of the individual  $m_b$ 's reported by

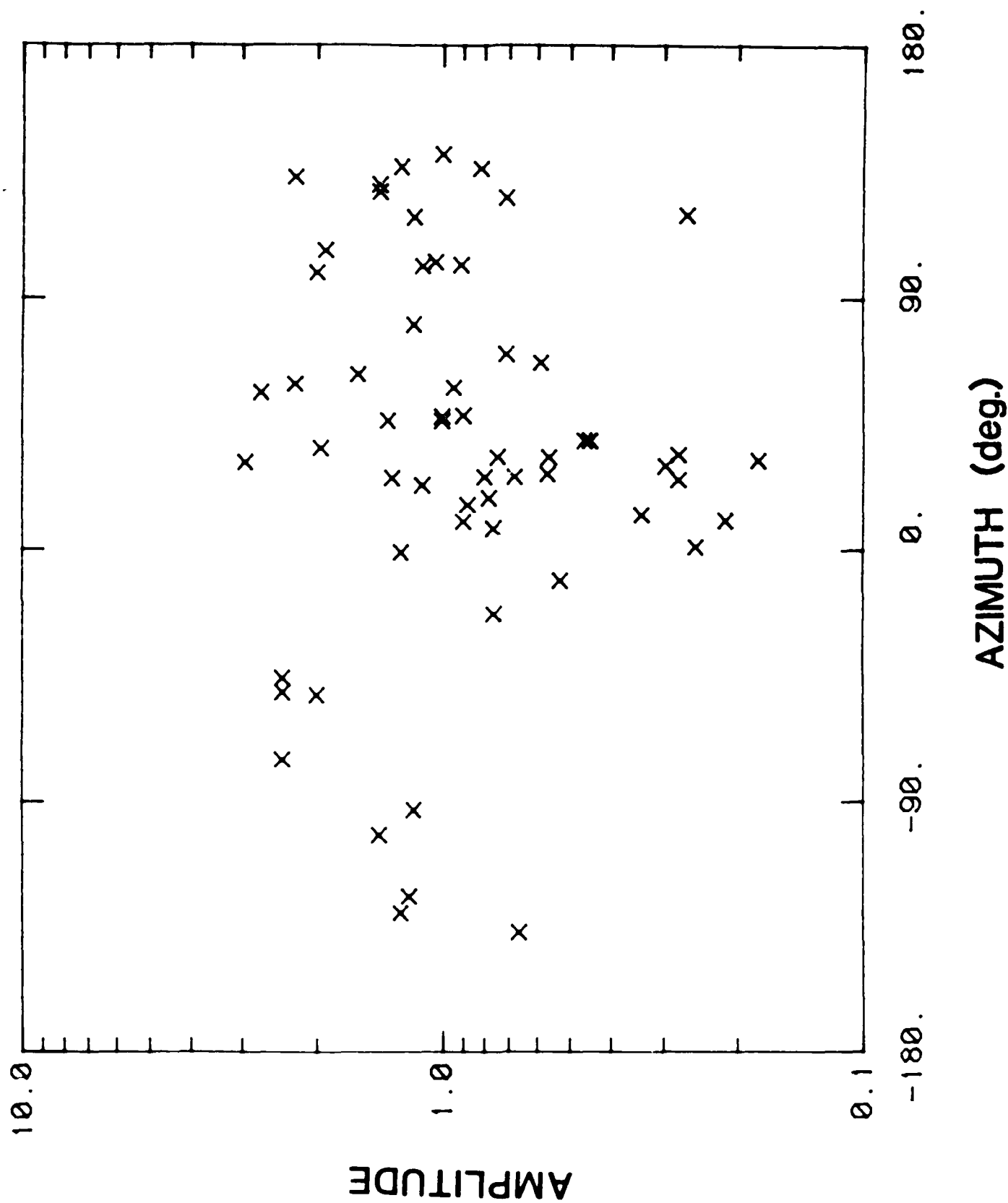


Figure 5. Observed amplitudes of teleseismic P waves from Pahute Mesa tests as a function of azimuth from Lay et al. (1984).

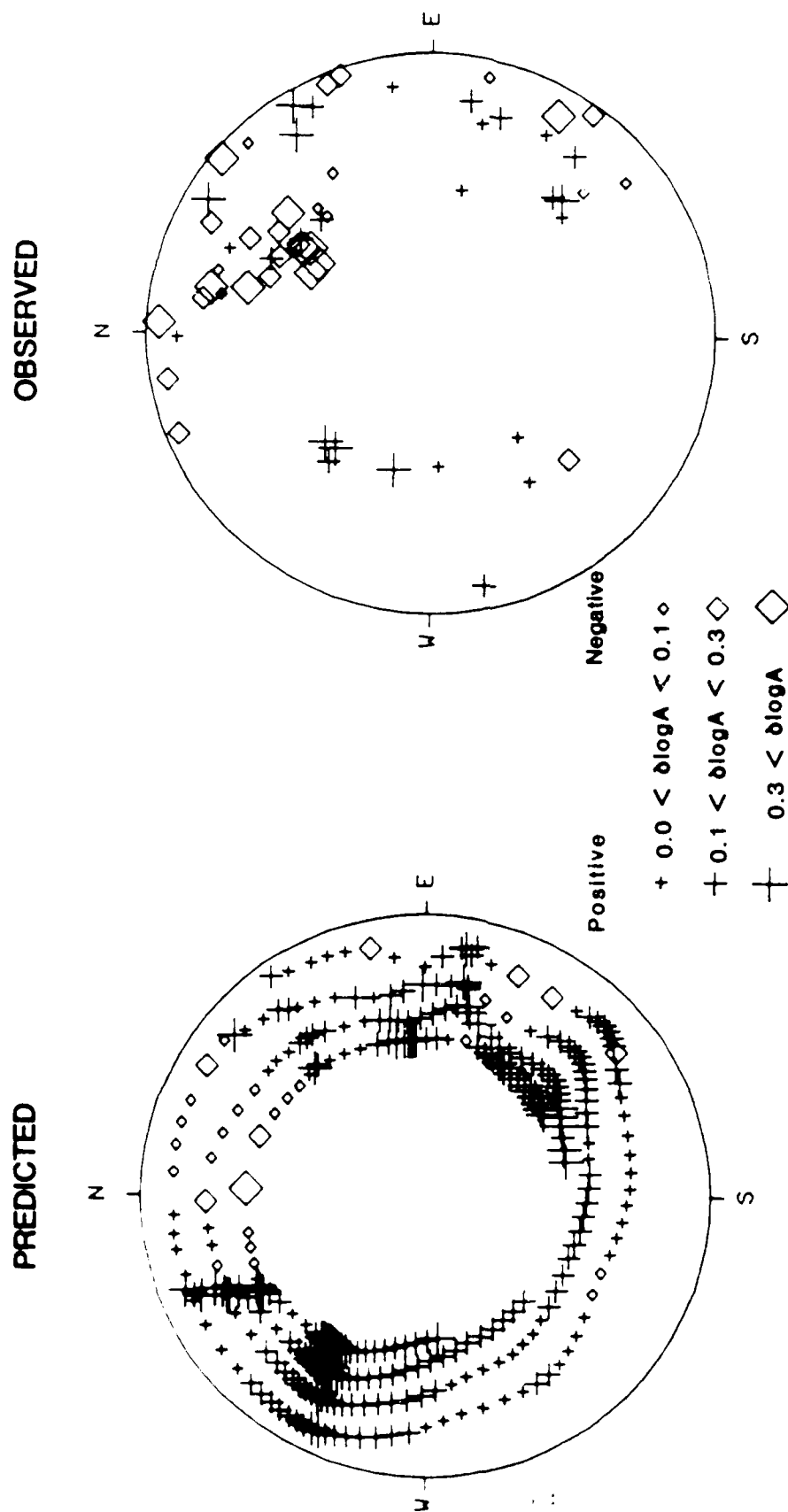


Figure 6. Predicted and observed amplitudes of the Pahute Mesa tests. Symbols are plotted on an equal area, lower hemisphere projection, as a function of vertical and azimuthal angles of the rays leaving the heterogeneous region at 100 km. depth. The radius of the focal sphere is taken to be that for the vertical take-off angle of P waves that propagate to stations at  $35^\circ$  distance in a one-dimensional, radially symmetric earth.  $\delta \log A$  measures the difference in log amplitude from the log amplitude predicted in a 1-D earth.

stations in a global network. For example, maximum likelihood processing can take into account variations in the azimuthal distribution of stations (Ringdal, 1976) and hence can be designed to provide azimuthally dependent weights based on the focusing and defocusing properties of the source region.

The dependence of focusing and defocusing effects on vertical as well as azimuthal ray angle is better illustrated in a plot of amplitudes on a focal sphere. This is shown in Figure 6. In this plot, the agreement between observed and predicted amplitudes is more compelling, with some second order features that depend on both take-off angles highlighted. Note the agreement of negative anomalies near azimuths  $75^{\circ}$ ,  $120^{\circ}$ ,  $150^{\circ}$ , and  $190^{\circ}$  as well as the relative size of negative and positive anomalies in the northeast quadrant.

*Correlation of predicted travel times and amplitudes.* Figure 7 shows the azimuthal and take-off angle dependence of travel time residual predicted by Taylor's model. The same results are shown in the form of focal sphere plots in Taylor's paper. The residual is taken from the predicted time of PREM (Dziewonski and Anderson, 1981). Figure 8 plots this travel time residual against amplitude. The general sense of the correlation, expected for focusing and defocusing is apparent, with slow times correlating with large amplitudes. The scatter from this trend, however, is large. Thus, weak or non-existent correlation of travel time anomalies with amplitude anomalies of data should not necessarily be taken as proof that focusing and defocusing is not affecting amplitudes. Similar weak correlations between amplitudes and travel times have been found in other studies (e.g., McCreery, 1986).

An intuitive argument why log amplitudes do not precisely correlate with travel times can be made by considering travel time curves and ray density plots of test structures. It can be seen that the common situation is that rays will tend to cluster near caustic surfaces and regions of high velocity gradient.

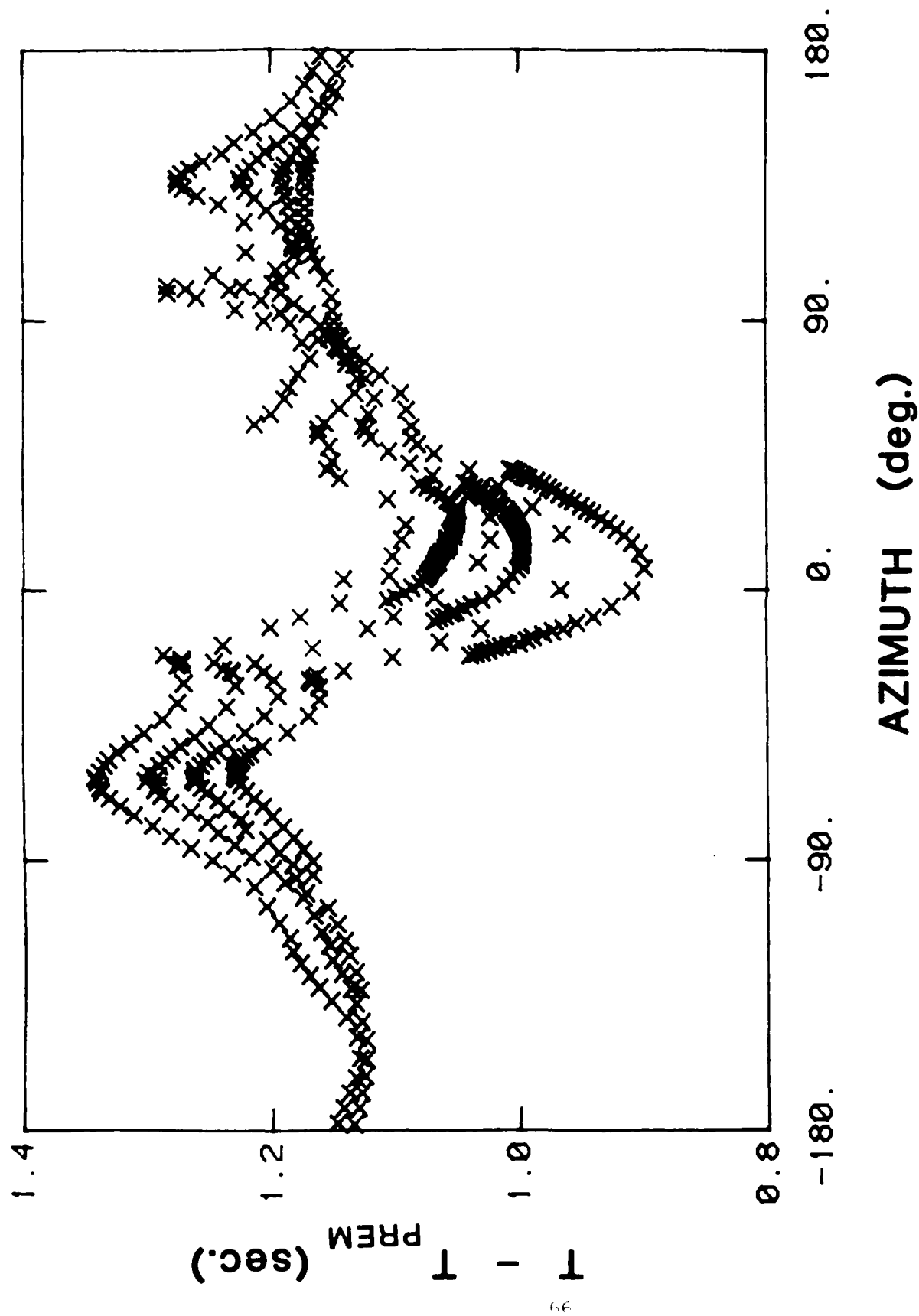


Figure 7. The difference in time  $T$  of teleseismic  $P$  waves propagating from a source located as shown in Figure 1 from the time  $T_{PREM}$  calculated in the radially symmetric earth model of Dziewonski and Anderson (1981).



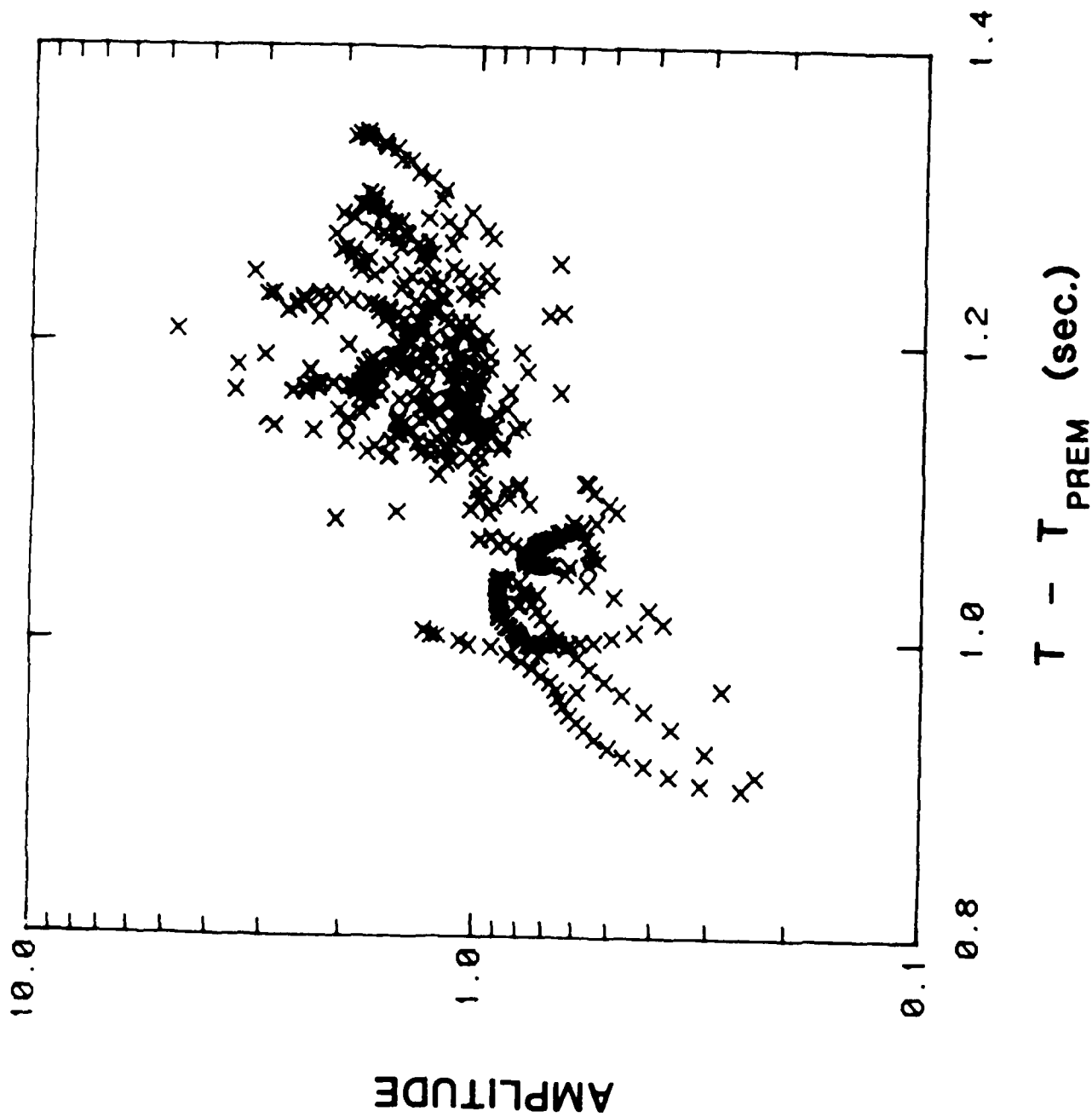


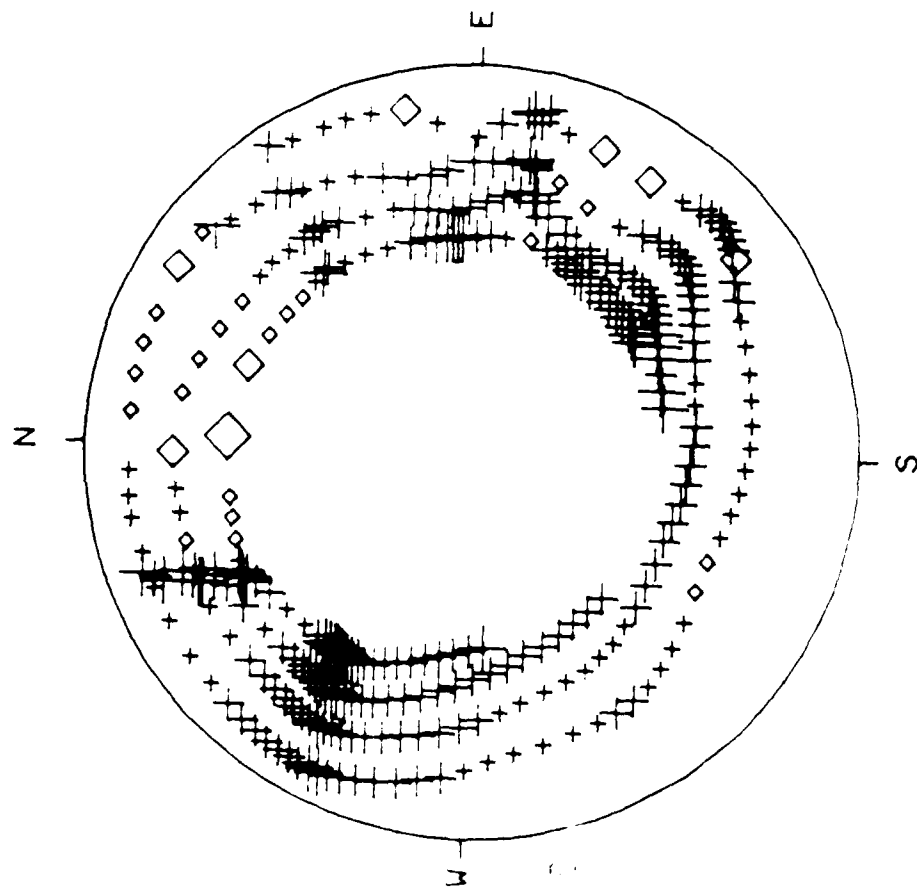
Figure 8. Correlation of calculated amplitudes and travel times for teleseismic P waves from a Pahute Mesa source in the Taylor model.

The rays having the slowest travel times, however, will tend to be slightly displaced from the regions of densest rays. An example of this can be seen in the fault zone calculations of Cormier and Spudich (1983). In that example, the highest amplitudes are associated with caustics near a region of high lateral gradient at the edges of the fault zone but the slowest travel times are in the center of the fault zone. Thus, log amplitudes will tend to be correlated only in a general regional sense with travel times. A travel time-log amplitude plot will typically have large scatter.

*Effects of model parameterization* Velocity models parameterized by blocks, while convenient for travel time calculations, are not the most suitable for amplitude calculations. The sharp velocity contrasts at block boundaries generate clusters of low and high amplitudes that rapidly vary over the focal sphere. Moreover, sharp boundaries at the edges of blocks having linear dimensions on the order of 10 to 20 km may not be representative of the true variation of earth structure at these scale lengths in the upper mantle. For these reasons, the Taylor model was instead parameterized by splines under tension (Cline, 1981). P velocities were specified at knots placed at the center of the original blocks. When the tension parameter  $\sigma = 0$ , velocities are interpolated by cubic polynomials. When  $\sigma = 50$ , the interpolation is essentially linear.

Because ray paths are strongly perturbed by changes in velocity gradient and the dynamic equations governing geometric spreading depend on the second spatial derivative of velocity, one may expect that the tension parameter would affect the teleseismic amplitude pattern. A test of this is shown in Figure 9, which compares predicted amplitudes for  $\sigma = 10.0$  and  $\sigma = 0.0$ . The broad regions of negative and positive perturbations remain substantially the same in the two cases. Negative anomalies are observed in both cases to the north and northeast, with more negative anomalies observed

PREDICTED  $\sigma = 10.0$



PREDICTED  $\sigma = 0.0$

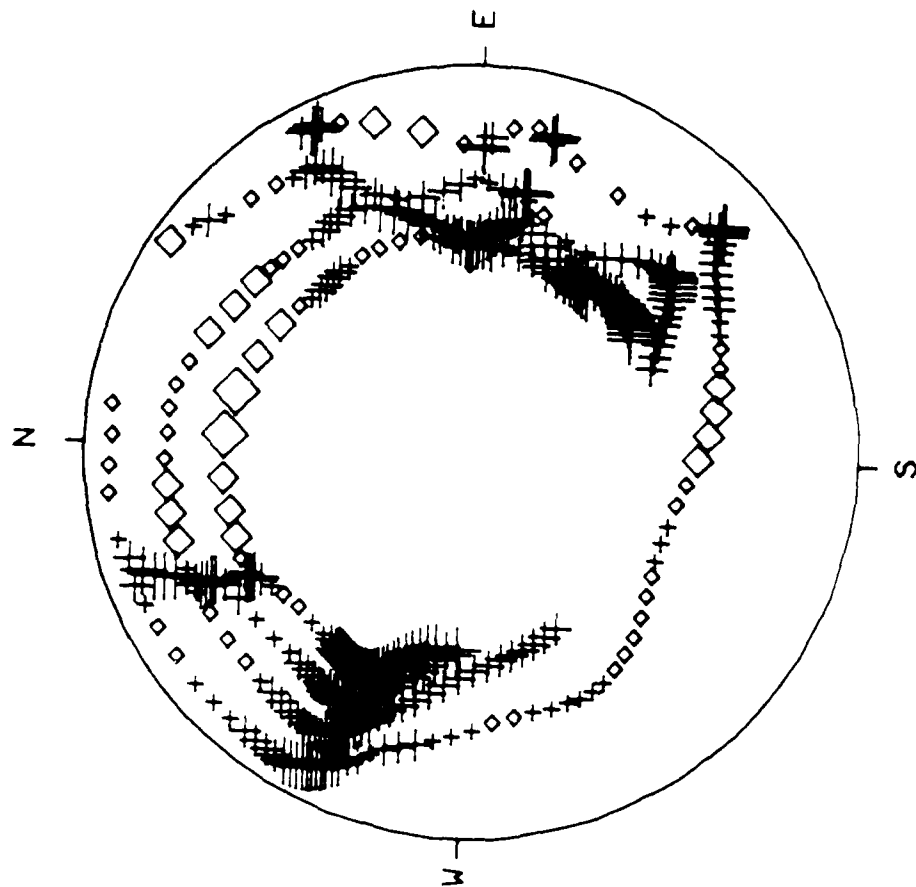


Figure 9 A comparison of predicted amplitudes of teleseismic P waves in the Taylor model parameterized by splines under tension with two different values of the tension factor  $\sigma$ .  $\sigma = 10$  corresponds to nearly linear

for more distant stations at steeper vertical take-off angles. The most pronounced differences are seen to be associated with caustics, marked by narrow regions of tightly clustered, positive anomalies. For example, note the differences around the azimuths bounded by  $300^{\circ}$  and  $340^{\circ}$ . In the region of the model producing the anomaly pattern in this zone, zero tension introduces a high velocity region between two different low velocity regions. The amplitude anomalies between the two caustics become weakly negative instead of weakly positive. In essence, low values of tension tend to decrease the fundamental scale length of the model by allowing strong fluctuations of velocity between knot points. Clearly, a higher tension, corresponding to linear interpolation is desirable because it will tend to be more faithful to the original scale lengths resolved by the travel time inversion.

Simple ray theory rather than superposition of Gaussian beams was chosen for the calculations in Figures 6 and 9 because it enabled a more rapid calculation of the amplitude anomalies at a high density of stations and because there was no evidence of strong frequency dependence in a trial synthesis by beam superposition. If the amplitude anomalies shown in Figure 9 had been calculated by beam superposition rather than by ray theory, an even closer comparison would have been obtained. This is because the superposition tends to average the structure over a Fresnel zone, which, for the short period band, is on the order of the distance between knots. Also in the beam superposition, the tight clusters of positive amplitude anomalies seen near azimuths  $300^{\circ}$  and  $340^{\circ}$  would be reduced in size and spread out over a slightly larger region. As discussed earlier, these caustics are too spatially concentrated to produce any phase distortion in the pass band of short period instruments.

#### EFFECTS ON P-CODA

**Coda stability and waveform complexity** For variations in source and receiver site on the order of 10 to 100 km, magnitude measures based on integrated P coda vary less than those based on the amplitude of the first several cycles of the P wave (Ringdal, 1983; Baumgardt, 1985; Gupta et al., 1986). This observation is consistent with the effects of focusing and defocusing by large scale structures in the mantle beneath the source region together with the assumption that the coda is generated by scattering by heterogeneities concentrated in the crust and uppermost mantle. In the source region, the effects of focusing and defocusing are minimized for scatterers located at a distance from the source that is greater than the characteristic wavelength of heterogeneity in the mantle beneath the source (Figure 10). For a hypothesis of the coda being dominated by single scattering, the later part of the coda will become progressively better in minimizing the effects of focusing and defocusing. This is because the later coda, being generated by scattering structure further from the epicenter, is more likely to travel to the receiver by a P wave path that does not sample the same mantle heterogeneity. These different mantle heterogeneities will produce different degrees of focusing and defocusing than that of the heterogeneity sampled by the P wave path responsible for the first arrival. In three dimensional geometry, this effect is magnified by integrating the scattering that occurs within a concentric ring surrounding the source.

A simplified calculation of this effect for the Pahute structure is shown in Figures 11 and 12. The scattering is assumed to be dominated by scattering of energy propagating to and horizontally in the crust as S, Ig, or Kg waves into P waves propagating to and vertically away from the source region. A ring of scatterers is assumed at a radius of 33 km from a Pahute source. The radius of the ring is chosen to simulate the effects on the coda arriving 10 sec. after the direct P wave for S, Ig, or Kg to P scattering. The group velocity of the S, Ig, or

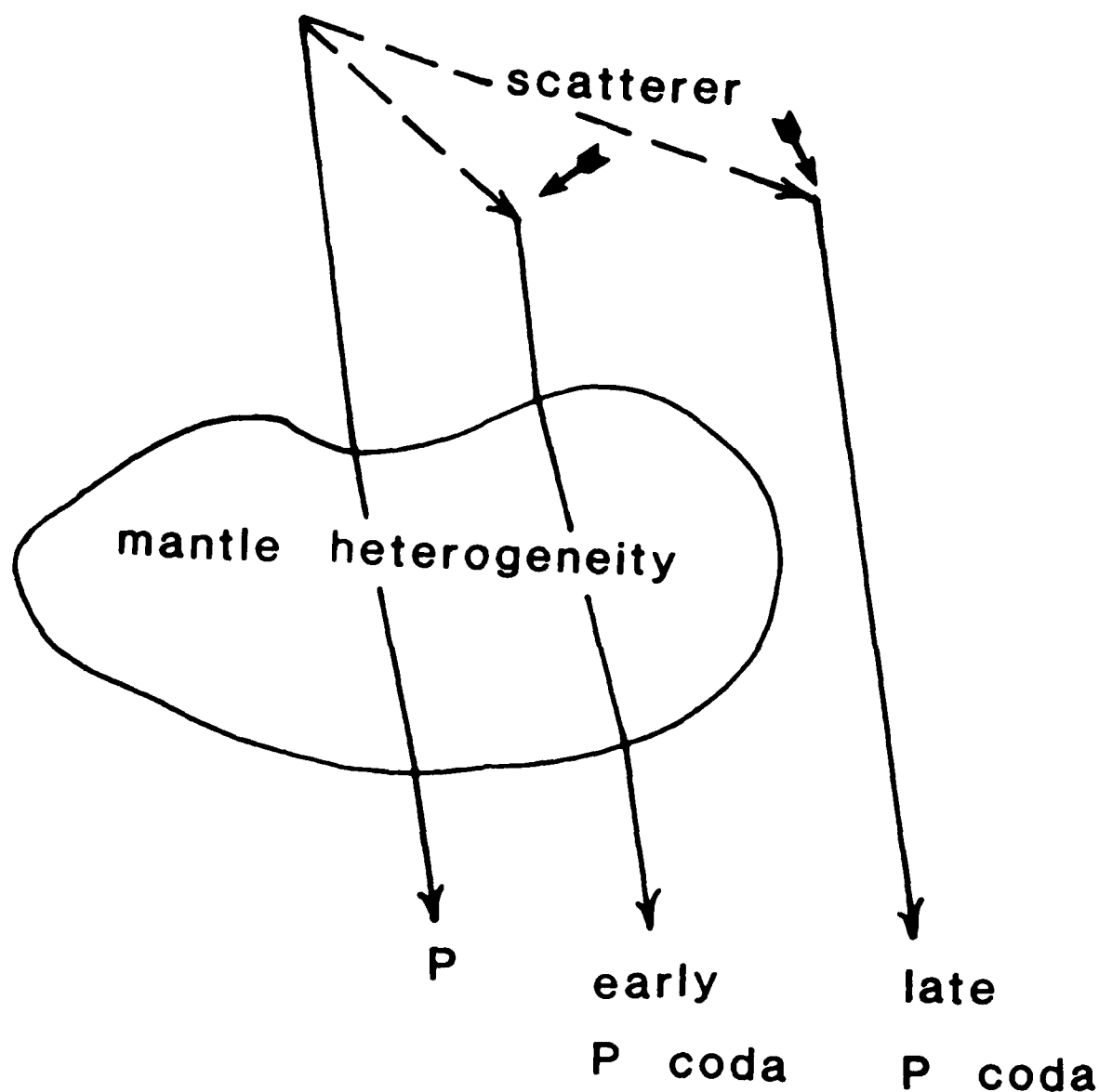


Figure 10 Schematic ray paths of direct P and P coda energy for a source located near a velocity heterogeneity in the upper mantle. P, S, Lg, or Rg energy propagates in the direction of the dashed line away from the source and is scattered into a P wave by a heterogeneity in the crust or upper mantle.

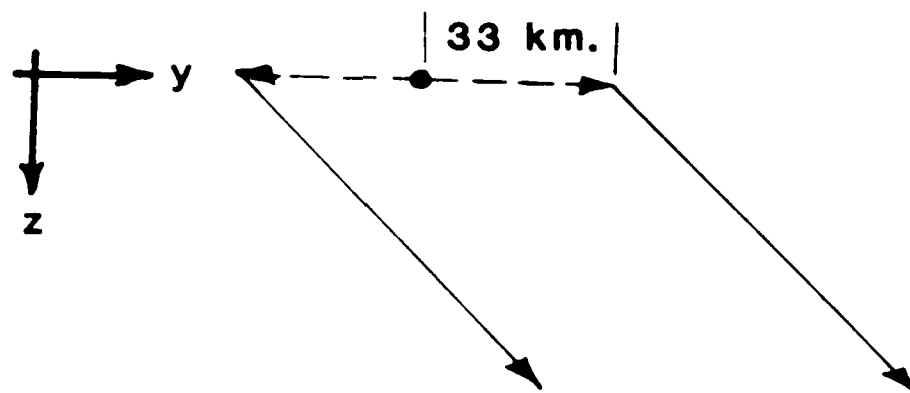
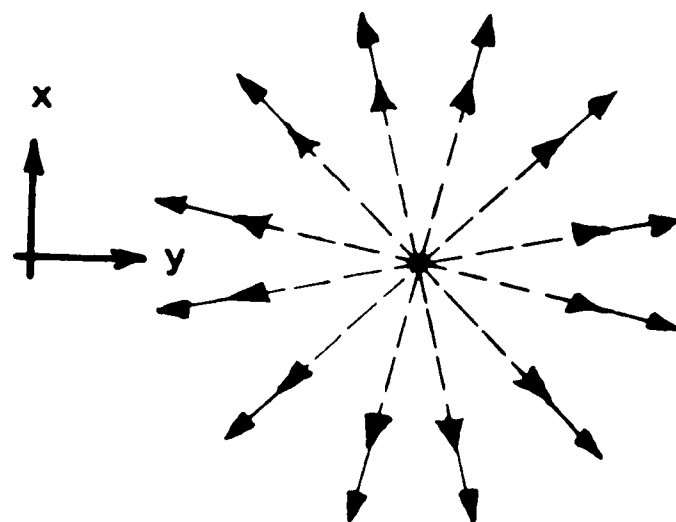


Figure 11. An approximate calculation of focusing and defocusing effects is made for coda generated near the source by considering a ring of scatterers located 33 km. laterally from the source.

Rg wave is assumed to be 3.3 km./sec. Wide angle scattering is assumed in the vertical angle but only narrow angle scattering is assumed in the azimuthal angle. Scattering near the receiver, scattering in the deep mantle, and multiple scattering, are, for the time being, neglected.

There is still a suggestion of the northerly minimum in coda amplitude in Figure 12, but the minimum is not as intense or as wide in azimuthal range as for the direct P wave. The nearly constant levels of amplitude in westerly azimuths for more distant stations are due to the fact that the scattered P rays traversed a portion of the model in which the reference one-dimensional model of structure was unperturbed.

These effects are consistent with those observed by Lay and Wells (1986ab) in Pahute waveforms in the 5 to 10 sec. time window following the direct P. They found the coda to be less affected by defocusing in northerly azimuths. The effects decreased with later time in the coda. P waveforms were generally more complex in northerly azimuths. This agrees with one of the scenarios proposed for the origin of waveform complexity by Douglas et al. (1973), in which complex waveforms are created when the direct P wave is defocused by mantle structure relative to the P coda.

Other examples of forward modeling of focusing and defocusing (Cormier, 1986; McLaughlin, 1987) find that variations in source location as small as 30 to 50 km. are sufficient to strongly affect the amplitudes of direct P waves. The controlling factor is the characteristic scale lengths of 1 percent and greater velocity heterogeneities in the upper mantle. These observations bear upon a hypothesis of Douglas et al. (1981). To account for complex and simple waveforms observed over nearly identical ray paths, Douglas et al. suggested that the coda was generated by weak scattering all along the ray path rather than by scattering concentrated in the crust and uppermost mantle. The



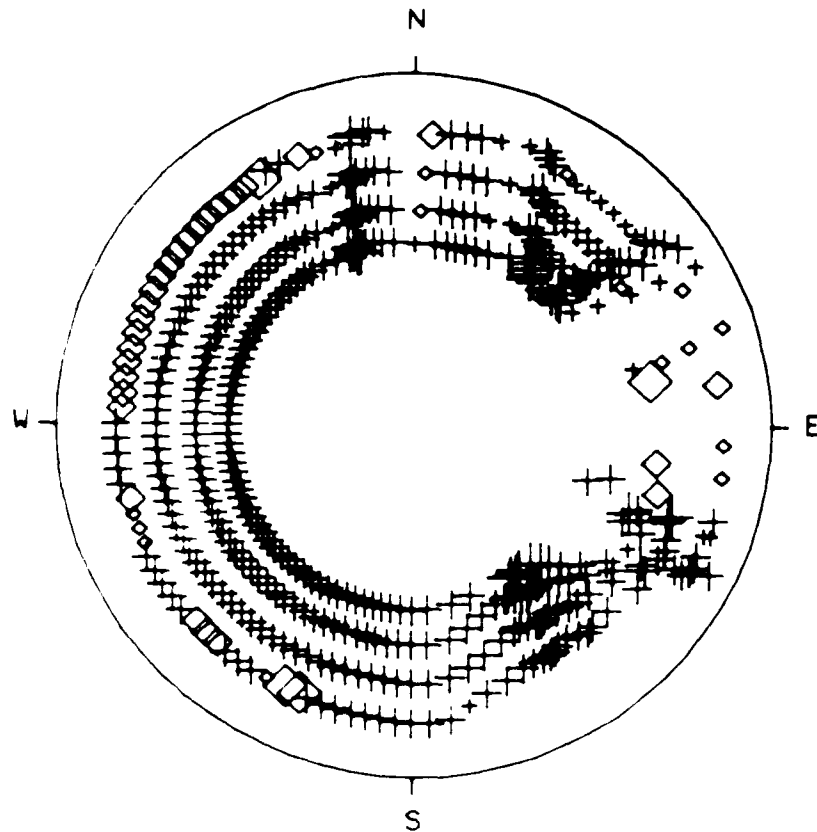


Figure 12. A focal sphere plot of the amplitude of coda arriving 10 sec. after direct P using the approximate calculation illustrated in Figure 11. The ring of scatterers was assumed to be centered around the epicenter shown in Figure 1. Symbols are defined in Figure 6. This calculation only simulates effects on coda generated near the source. The coda will also have a component generated near the receiver.

results of the focusing and defocusing experiments reported here and in other studies, however, suggest that it may not be necessary to invoke significant scattering in the deep mantle to account for simple and complex waveforms for nearby ray paths, if "nearby" is taken to be distances as large as 30 to 50 km.

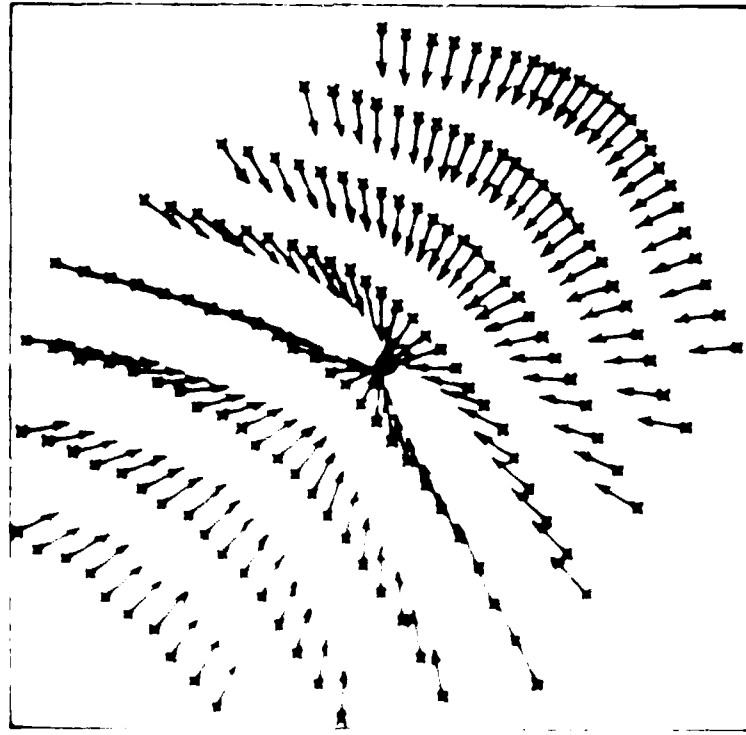
*Wide versus narrow angle scattering* Wide angle scattering in the azimuthal angle can be more effective in reducing the effects of focusing and defocusing compared to narrow angle scattering. Wide angle scattering allows greater opportunities for scattered P waves to sample regions outside of a particular focusing/defocusing structure in the upper mantle. From amplitude and phase correlations at NORSAR, Wu and Flatto' (1986) suggest that wide angle scattering is particularly important in the upper 1 to 2 km of the crust. They postulate that wide angle scattering at shallow depths can account for imperceptible fluctuations in travel time being associated with large amplitude fluctuations at small (7 km) aperture sub-arrays (e.g., Thomson, 1983).

To the extent that greater scattering at wider angles occurs in the shallow crust, the teleseismic P coda of shallower explosions should be more stable and successful in minimizing and homogenizing the effects of focusing/defocusing structures in the mantle beneath the source. Different scattering properties of the shallow crust compared to the deep crust may account for the observation of greater complexity for smaller and shallower events compared to larger and deeper events as reported by Lay and Webb (1980).

*Coda generated near the receiver* Coda generated near the receiver is less successful in removing the effects of focusing/defocusing structure beneath the source region. This is illustrated in Figure 10, where ray end points of ray end points for different vertical and azimuthal take-off angles in the vicinity of a low amplitude defocused and high amplitude focused station. In these cases, the concentration of ray end points is quite different over a large area.

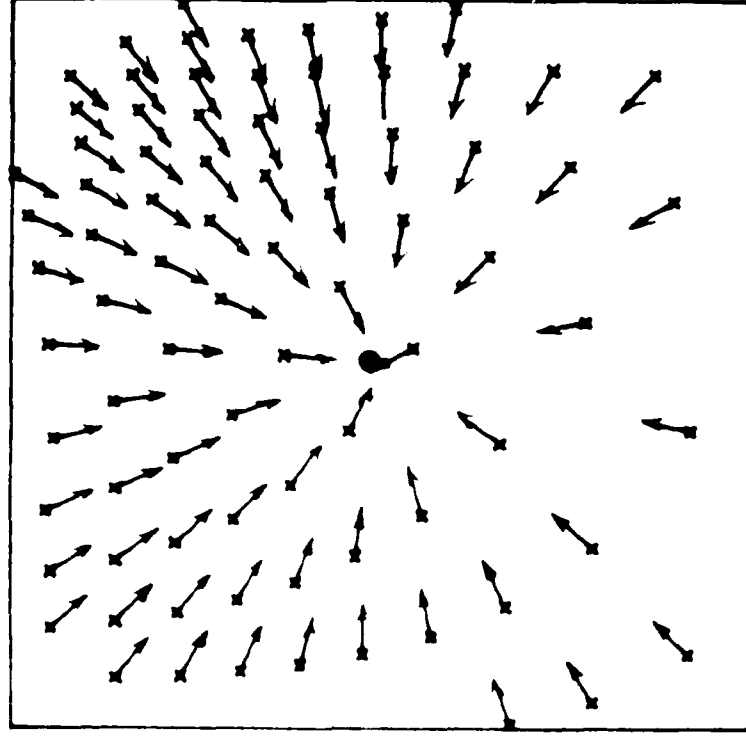
HIGH AMPLITUDE

STATION



LOW AMPLITUDE

STATION



2000 (km.)

Figure 13 Ray end points are marked by crosses(x). Arrows are drawn for possible scattering paths for coda generated near the receivers. The two stations were selected from the set used in the Gaussian beam calculations shown in Figure 3. The high amplitude station was the one at 135° azimuth and the low amplitude station is the one at 0° azimuth. Note that coda generated over a broad region near the receiver can be

This is because the small region in which rays are focused or defocused near the source is spread out over a very broad region after propagation to teleseismic range. Scattering can occur over a very broad region near the receiver for rays having a very small distribution of vertical and azimuthal take-off angles of direct P near the source. Assuming that scattering is uniformly concentrated in the crust and upper mantle near the earth's surface, the P coda for an explosion or earthquake near the earth's surface will be composed of roughly equal amounts of P energy scattered near the source and near the receiver. The P coda of a deep focus earthquake will primarily be composed of P energy scattered near the receiver. These predictions have been verified by comparison of the phase velocities of late P coda energy from deep and shallow earthquake sources (Dainty, 1986). With this model of scattering, it is clear why coda magnitudes of shallow events will tend to be only about fifty percent successful in homogenizing the effects of focusing and defocusing structures near the source and receiver. At each receiver, a coda magnitude will be successful in removing the effects of focusing/defocusing structures beneath the receiver, with the performance progressively improving with increasing time into the coda. Even the very late portion of the coda, however, will not be totally successful in removing the effects of focusing/defocusing structure beneath the source. This is because about fifty percent of the late coda will consist of direct P that has been focused or defocused near the source and then scattered near the receiver.

A true estimate of the fluctuation of coda magnitude due to focusing and defocusing structures near the source would look more like an average of the predictions in figures 8 and 9. This agrees with the results of many coda studies (e.g., and Wood, 1986), for example, find a similar, although less pronounced, azimuthal pattern of amplitudes in the 10-15 sec time window of P coda for great depth earthquakes. The coda also seems to be generally

more stable than direct P, but not necessarily for every source and receiver combination (Bullitt and Cormier, 1984). The increased stability will depend on the relative importance of scattering and focusing/defocusing near the source versus that occurring near the receiver. The worst performance of coda magnitudes will occur in a situation in which the strongest focusing/defocusing is in the upper mantle close to the source and in which scattering in the crust near the source is relatively weak.

### CONCLUSIONS

A known three-dimensional structure beneath Pahute Mesa, Nevada Test Site (Taylor, 1983) can account for many of the features in the azimuthal amplitude pattern of teleseismic P waves from Pahute underground tests. This model can be used to correct for focusing and defocusing effects of the structure beneath Pahute Mesa accounting for factors of three in amplitude fluctuation and for 0.6 sec. in travel time fluctuation. The reduction in variance of teleseismic magnitude or log amplitude using these corrections is about 25 percent, similar to the reduction of variance in teleseismic travel times. These results are useful in predicting the structural resolution needed for models of other test sites to be useful in making corrections for focusing and defocusing. The NTS results suggest that meaningful corrections can be made if the model resolves 10 to 20 km. scale lengths down to 100 km. with perturbations of velocity exceeding 4 percent. Velocity inversions that primarily resolve scale lengths larger than these or that smooth over anomalies larger than 2 percent, (e.g., Montfort and Evans, 1982; Minster et al., 1981), are much less useful in making amplitude corrections. By analogy to the Taylor inversion for NTS, the data required to resolve structure having these scale lengths are teleseismic travel times and locations of tests widely distributed over the area of the source, and a receiver array of 10 km. with significant concentrations of

tests spaced less than 10 km. apart. It is also necessary to obtain an average crustal structure within the test site from seismograms recorded at local and regional range.

The focusing and defocusing effects of 20 to 50 km. scale length structure having perturbation in P velocity of several percent is nearly independent in the frequency band of teleseismic body waves. This conclusion is even stronger in the 0.2 to 10 Hz. band in which measurements are made on the teleseismic P waves of underground nuclear tests. Frequency dependent effects in the coda of teleseismic P waves are probably due to either the effects of heterogeneities having scale lengths smaller than 20 km. and/or to frequency dependent effects in the scattering processes occurring near the source and receiver.

Magnitude measurements based on the integrated energy in the coda of teleseismic P waves are likely to be more stable because they can remove some of the focusing/defocusing effects of three-dimensional mantle structure near the source. The deeper in the coda, the measurement is made, the less affected it will be by mantle structure near the source. The optimal time in the coda for this measurement should be as long as possible after the direct P wave given the signal to noise ratio. The minimum time to achieve good stability can be estimated by dividing the length of characteristic scale lengths of mantle structure near the source by the velocity of the presumed scattered wave near the source. For example, assuming a 3.3 km./sec. S wave is scattered into a P wave that is propagated to teleseismic range, one would estimate that after 30 sec. into the coda, the focusing/defocusing effects of 100 km. scale and smaller length structure beneath the source would be minimized. Coda magnitudes, however, are only partially successful in removing the focusing/defocusing effects of structure beneath the source. They cannot remove these effects from the fraction of the coda that is due to scattering of direct P near the receiver.

These conclusions are consistent with tests of the relative performance of coda versus classical magnitudes. The predicted behavior of coda amplitude critically depends on assumptions about the distribution of mantle heterogeneity with depth. Smaller scale heterogeneities with greater percent velocity fluctuations are assumed to be concentrated closer to the surface. Scale lengths on the order of several kilometers to 10 kilometers are assumed in the crust and scale lengths on the order of 10 to 100 kilometers are assumed in the upper mantle. Fluctuations in the mid and lower mantle down to the D" layer near the core are assumed to be smaller than 1 percent.

#### ACKNOWLEDGEMENTS

Helpful discussions were held with Bob Blandford, Anton Dainty, Stanely Flatte', Keith McLaughlin, and Bob Nowack. I also thank Steve Taylor for listings of his N.T.S. model and Thorne Lay, C. Lynnes, and J. Wele for comments and preprints of their recent papers. This research was supported by the Advanced Research Projects Agency of the Department of Defense and was monitored by the Air Force Geophysics Laboratory under contract #19628-85-K-0031.

## REFERENCES

- Aki, K., A. Christoffersson, and E.S. Husebye (1977). Determination of three-dimensional seismic structures of the lithosphere, *J. Geophys. Res.*, **82**, 277-296.
- Archambeau, C.B. (1972). The theory of stress wave radiation from explosions in prestressed media, *Geophys. J. R. Astr. Soc.*, **29**, 329-366.
- Bache, I.C., (1976). The effect of tectonic release on short period P waves from NTS explosions, *Bull. Seism. Soc. Am.*, **66**, 1441-1457.
- Baumgardt, D. (1985). Comparative analysis of teleseismic P coda and Lg waves from underground nuclear explosions in Eurasia, *Bull. Seism. Soc. Am.*, **72**, S319-S330.
- Bullitt, J.T., and V.F. Cormier (1984). The relative performance of mb and alternative measures of elastic energy in estimating source size and explosion yield, *Bull. Seism. Soc. Am.*, **74**, 1863-1882.
- Červený, V., (1985a). The application of ray tracing to the propagation of shear waves in complex media, in *Seismic Exploration*, eds. Treitel, S., and Helbig, K., Vol. on Seismic Shear Waves, ed. Dohr., G., Geophysical Press, pp. 1-124.
- Červený, V., (1985b). Gaussian beam synthetic seismograms, *J. Geophys.*, **58**, 44-72.
- Cline, A.K., (1981). FITPACK -- software package for curve and surface fitting employing splines under tension, Department of Computer Science, University of Texas, Austin.



- Cormier, V.F., and P. Spudich (1984). Amplification of ground motion and waveform complexity in fault zones: examples from the San Andreas and Calaveras faults, *Geophys. J. R. astr. Soc.*, **79**, 135-152.
- Cormier, V.F., (1986). An application of the propagator matrix of dynamic ray tracing: the focusing and defocusing of body waves by three-dimensional velocity structure in the source region. *Geophys. J. R. Astr. Soc.*, **87**, 1159-1180.
- Dainty, A.M. (1985). Coda observed at NORSAR and NORESS, Final Technical Report, AFGL-TR-85-0199, Hanscom AFB, 73pp. ADA166454
- Douglas A., P.D. Marshall, P.G. Gibbs, J.B. Young, and C. Blamey (1973). P signal complexity re-examined, *Geophys. J. R. Astr. Soc.*, **33**, 195-221.
- Douglas, A., J.A. Hudson, and B.J. Barley (1981). Complexity of short period P sseismograms: what does scattering contribute? Report No. 03/81, Atomic Weapons Research Establishment, Aldermaston, Berkshire, United Kingdom.
- Dziewonski, A.M., and D.L. Anderson (1981). Preliminary reference earth model (PREM), *Phys. Earth Planet. Inter.*, **25**, 297-356.
- Gupta, I.N., R.R. Blandford, R.A. Wagner, J.A. Burnett, and T.W. McElfresh (1985a). Uses of P coda for determination of yield of nuclear explosions, *Geophys. J. R. Astr. Soc.*, **83**, 541-554.
- Helmberger, D.V., and D.M. Eadley (1981). Seismic source functions and attenuation from local and teleseismic observations of the NTS events Jorum and Eadley, *Bull. Seism. Soc. Am.*, **71**, 51-77.
- Lay, T., T.C. Wallace, and D.V. Helmberger (1984). *The effects of tectonic release*

on short period P waves from NTS explosions, *Bull. Seism. Soc. Am.*, **74**, 819-842.

Lay, T., and J.L. Welc (1986). Analysis of near-source contributions to early P-wave coda for underground explosions: 1. Waveform Complexity, *Bull. Seism. Soc. Am.*, **76**, submitted, 1986.

Lay, T. (1986). Analysis of near-source contributions to early P wave coda for underground nuclear explosions: 2. Frequency Dependence, *Bull. Seism. Soc. Am.*, **76**, submitted, 1986.

Lynnes, C., and T. Lay, Defocusing of short period P waves by a high velocity anomaly beneath Pahute Mesa (1984). *EOS Trans. Am. Geophys. Un.*, **65**, 994.

Lynnes, C., and T. Lay, (1987). Analysis of amplitude and travel time anomalies for short-period P waves from NTS explosions, *Geophys. J. R. Astr. Soc.*, in press.

Minster, J.B., J.M. Savino, W.L. Rodi, J.F. Masso, and T.H. Jordan, (1981) Three-dimensional velocity structure of the crust and upper mantle beneath the Nevada Test Site, Final Technical Report, SSSR 81-0138, Scubed, La Jolla, California.

McCreery, C.S., (1986) Yield estimation from spectral amplitude of direct P and P coda recorded by the Wake Island deep ocean hydrophone array, preprint.

McLaughlin, K.L., and L.M. Anderson (1987) Stochastic dispersion of short-period P waves due to scattering and multipathing, *Geophys. J. R. Astr. Soc.* **89**, 933-964.

- Montfort, M.E., and J.R. Evans (1982). Three-dimensional modeling of the Nevada Test Site and vicinity from teleseismic P-wave residuals, Open-File Report 82-409, U.S. Geol. Survey, Menlo Park, California.
- Ringdal, F. (1976). Maximum-likelihood estimation of seismic magnitude, *Bull. Seism. Soc. Am.*, **66**, 789-802.
- Ringdal, F., (1983). Magnitude from P-coda and Lg using NORSAR data, Fifth Annual DARPA Symposium on Seismic Detection, Analysis, Discrimination and Yield Determination, p. 34.
- Spence, W., (1974). P-wave residual differences and inferences on an upper mantle source for the Silent Canyon Volcanic Centre, Southern Great Basin, Nevada, *Geophys J R. Astr Soc*, **38**, 505-523.
- Taylor, S.R., (1983). Three-dimensional crust and upper mantle structure at the Nevada Test Site, *J Geophys Res*, **88**, 2220-2232.
- Thomson, C., (1983). Ray theoretical amplitude corrections for laterally varying velocity structure below NORSAR, *Geophys J R. Astr Soc*, **74**, 525-558.
- Wallace, T.C., D.V. Helmberger, and G.R. Eng (1983). Evidence for tectonic release from underground nuclear explosions in long period P waves, *Bull. Seism. Soc. Am.*, **73**, 593-609.
- Wallace, T.C., D.V. Helmberger, and G.R. Eng (1985). Evidence of tectonic release from underground nuclear explosions in long period S waves, *Bull. Seism. Soc. Am.*, **75**, 171-174.
- Wu, R.S., and S.M. Flatt6 (1986). Transmission fluctuation and angular decorrelation of seismic P waves across a large seismic array caused by the lithosphere modeled as a random medium (abstract), *EOS Trans Am Geophys Un*, **67**, 315.

## 5 Three-dimensional slab effects on S waves

### 5.2 A FEASIBILITY STUDY USING VERY WIDE GAUSSIAN BEAMS

It is quite resonable to assume that focusing and defocusing by slabs will be a frequency dependent phenomena. The slab is a narrow structure and one would expect that high frequency, short wavelength radiation would feel the presence of the slab, whereas, low frequency, long wavelength radiation would average out or not see the effects of a slab wider than the wavelength. To calculate these effects, it is necessary to use a technique which does not use the ray-theoretical stationary phase approximation. Instead, a technique is needed that incorporates waves arriving at many different directions and frequencies. Gaussian beam superposition and WKBJ/Maslov seismograms belong to a class of asymptotically approximate techniques that can include these effects. Comprehensive reviews of these respective techniques are given in Červený (1985a,b) and Chapman and Drummond (1982) and Thomson and Chapman (1986). Computational details associated with the examples shown here are described in subsection 5.2.

Figure 5.1 shows the results of synthesizing an S wave at 50 great circle degrees away from a 700 km deep earthquake in a 60 degree dipping slab, which penetrates to 1200 km depth. The velocity structure was derived from a model determined by Creager and Jordan (1986) from P travel time residuals, tied to a specific thermal model as described by Toksoz et al. (1971) and Murat and Tokso (1973). The effect of temperature is assumed to be such that  $\frac{dV_P}{dT} = \frac{dV_S}{dT}$  (Silver and Chan, 1986).  $\frac{dV}{dT}$  was taken to be  $0.0006 \text{ km/sec}^\circ\text{K}$  (Creager and Jordan, 1986). The length of the slab along strike is assumed to be 2000 km. S wave polarization is not yet included in the synthesis, but previous experiments with kinematic ray tracing show that the effects of the slab are small on the polarization angle, and less than  $\pm 10$  degrees (Cherner, 1984).

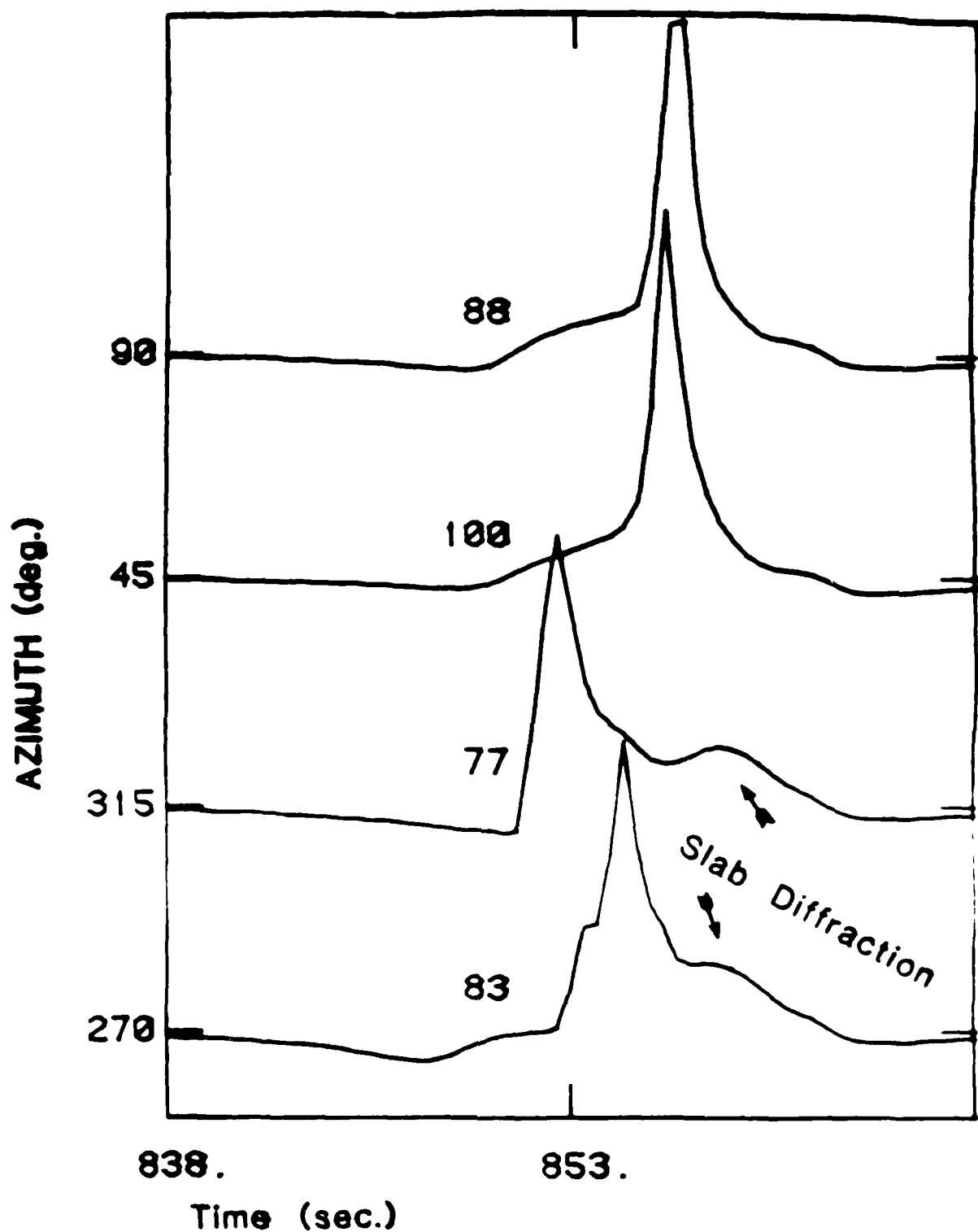


Figure 5.1 Synthetic SH waves at 50 great circle degrees and variable azimuths from a 700 km. deep earthquake located in a 50 degree dipping slab that penetrates to 1200 km. Slab parameters are taken from Creager and Jordan (1986) for the Kuril-Kamchatka slab. Computational details of the synthesis are described in Appendix A of this proposal and in Cormier (1986b). The numbers at the left of each pulse measure peak amplitude.

Several slab effects are illustrated in Figure 5.1. First, stations at azimuths on the dipping side of the slab ( $270^{\circ}$  and  $315^{\circ}$ ) arrive earlier than stations on the side away from the dipping direction ( $45^{\circ}$  and  $90^{\circ}$ ). Second, stations at azimuths on the dipping side have been defocussed by the high velocity slab and are smaller amplitude compared to stations at azimuths on the side away from the dipping direction (the numbers 77, 83, etc., indicate peak relative amplitude). Third, the stations on the dipping side exhibit a tail of energy that persists for up to 10 or more seconds after the peak. This tail may be termed a "slab diffracted" wave. At the station at  $315^{\circ}$  azimuth, the tail exhibits a secondary peak quite similar to the examples of slab diffraction shown in the two-dimensional, finite difference calculations of Vidale (1986).

That "slab diffraction" is an appropriate term can be seen by examining the location in space of the plane wave rays contributing to time window containing the tail. These rays are shown in Figure 5.2. Because of the strong shadow zone of the slab, it was found to be more efficient, in terms of shooting fewer rays, to conduct the synthesis in a reciprocal sense by shooting rays from a receiver towards the source. In Figure 5.2, a dense concentration of rays is seen in two locations near regions of strong gradient defining the position of the slab. The star marks the epicenter for the hypothetical earthquake used in the synthetic calculations. Low frequency energy, being more important further from the earthquake, can be strongly concentrated in these regions. In a sense, the slab diffraction is akin to a head wave traveling along the underside of the slab. It arrives later in the wave form because it is sensitive to the slower velocity structure that surrounds the high velocity slab.

It is significant that slab diffraction was found in the synthetic seismograms at azimuths far removed from the down dip direction. In fact, slab diffraction was found in a wide range of azimuths spanning the entire azimuthal range on the down dip side up to the direction parallel to slab strike. Slab diffraction in this example was stronger in the direction along the normal to the strike of the slab. Although the computational techniques are capable of synthesizing seismograms at any angle with respect to the

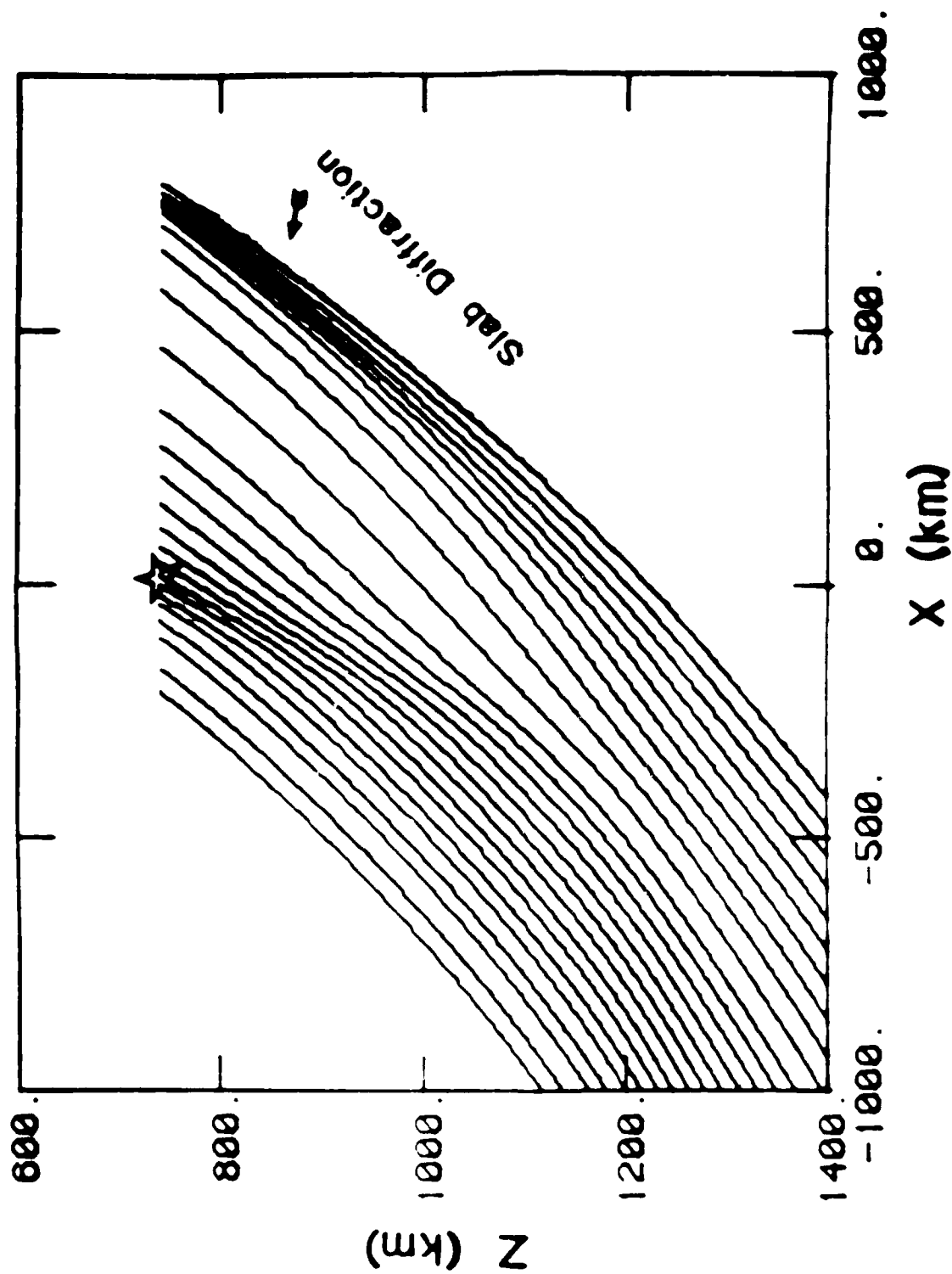


Figure 1. Ray-tray diagram of the velocity of a receiver located in the slab described in Figure 1 at azimuth  $270^\circ$  (down dip and perpendicular to strike of the slab). The synthesis of waveforms was conducted in a region also shown by shading rays from the true receiver location toward the area of loss of contact with the slab.





## EFFECT OF BEAM PARAMETER

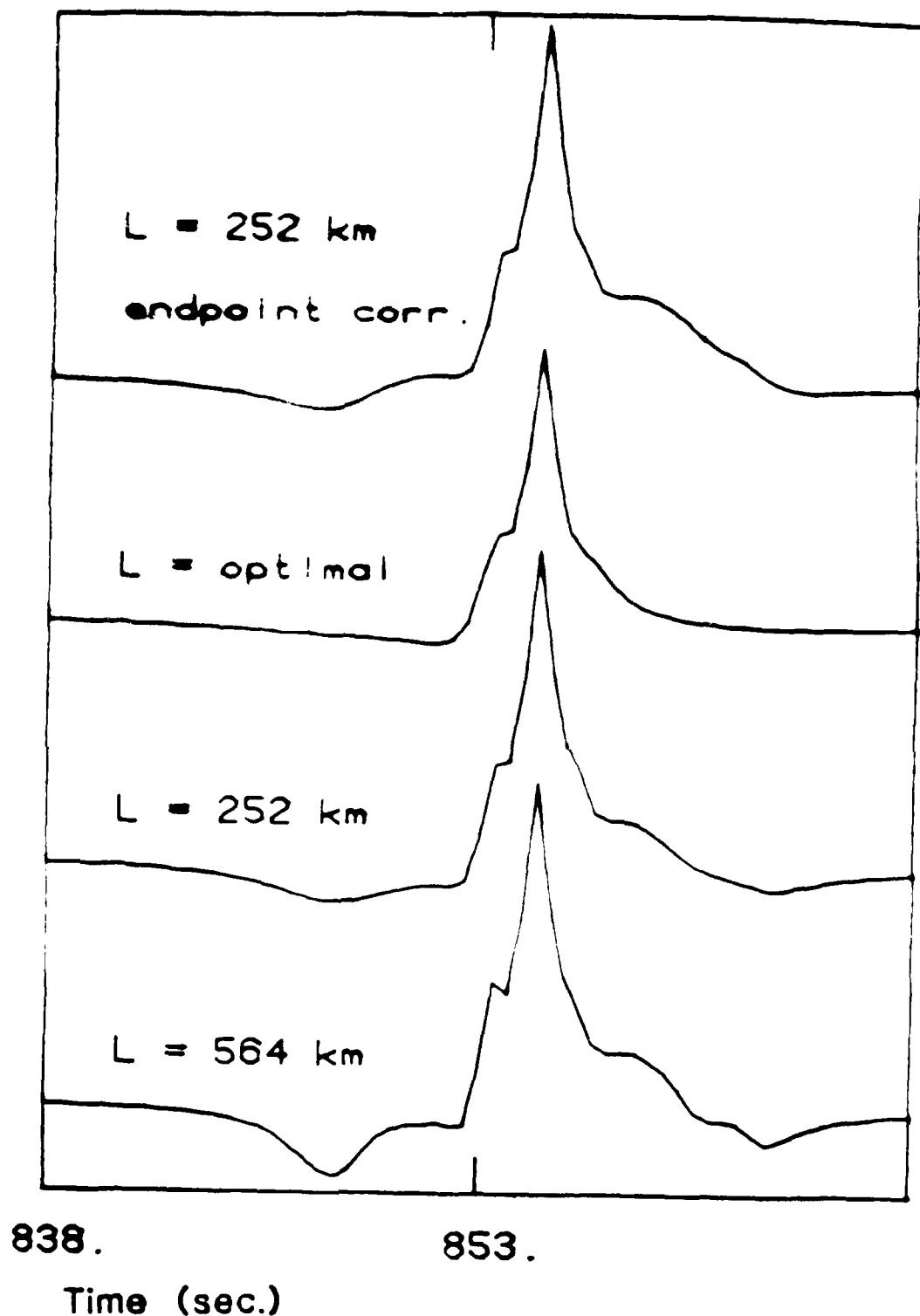


Figure 5.3 Effect of different Gaussian windowing or beam width parameters on synthetic S waves for a deep focus earthquake occurring at 700 km depth in a slab that penetrates to 1200 km. The receiver is perpendicular to the strike on the down dipping side of the slab. The parameter  $L$  is defined by  $\text{Im} \hat{g} = \frac{1}{\pi L^2}$ .

$$= \exp \{ i \mathbf{q}^T \mathbf{m} + \mathbf{M} \mathbf{q} + \Delta t \}$$

$$A = \sqrt{\det \mathbf{Q}^R} \sqrt{-\det(\mathbf{M} - \mathbf{M}^R)} \quad (5.3)$$

Equation (5.3) is summed over vertical and azimuthal take off angles.  $\tau$  is simply the Maslov/WKBJ delay time modified by an imaginary perturbation that depends on the width parameter of Gaussian beams and the distance to the station measured in ray centered coordinates. An additional damping factor has been included (Madariaga, 1984; Madariaga and Papadimitriou, 1985) that depends on the sampling rate  $\Delta t$ . The matrices  $\mathbf{M}$ ,  $\mathbf{Q}$  etc. are calculated by dynamic ray tracing, which involves integration of a set of linear equations along a ray path. These equations are in addition to the kinematic equations for ray trajectory and S polarization (e.g., Červeny and Hron, 1980; Kameš, 1984; Červeny, 1985a,b). The real part of the matrix  $\mathbf{M}$  was chosen to correct for the effects of gradients in the receiver region and makes the Gaussian beam superposition essentially equivalent to WKBJ/Maslov superposition of plane waves at the receiver with a small amount of Gaussian windowing. The quantities  $p_x$ ,  $p_y$  are components of vector slowness evaluated at the receiver. The most serious computational problems in computation are to make sure that a dense enough grid is used so that the complex delay time  $\tau$  is sampled at least at the rate of the sampling rate. The sampling problems are quite analogous to those pointed out by Červeny (1978) for WKBJ seismograms in a vertically inhomogeneous medium. The seismograms can be interpolated in amplitude  $A$  and delay time  $\tau$  if no caustics are present. A rapid variation in

Another interesting feature of the Gaussian beam approach is that the Gaussian windowing is equivalent to a Gaussian beam superposition of plane waves at the receiver. The quantities  $p_x$ ,  $p_y$  are components of vector slowness evaluated at the receiver. The most serious computational problems in computation are to make sure that a dense enough grid is used so that the complex delay time  $\tau$  is sampled at least at the rate of the sampling rate. The sampling problems are quite analogous to those pointed out by Červeny (1978) for WKBJ seismograms in a vertically inhomogeneous medium. The seismograms can be interpolated in amplitude  $A$  and delay time  $\tau$  if no caustics are present. A rapid variation in

AD-A184 203

TELESEISMIC WAVEFORM MODELING INCORPORATING THE EFFECTS 2/2

OF KNOWN THREE-DI (U) MASSACHUSETTS INST OF TECH

CAMBRIDGE EARTH RESOURCES LAB V F CORMIER 08 JUN 87

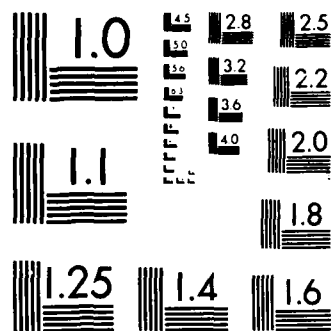
UNCLASSIFIED

AFGL-TR-87-0192 F19628-85-K-0031

F/G 8/11

NL





MICROCOPY RESOLUTION TEST CHART  
NATIONAL BUREAU OF STANDARDS-1963-A

angles at which the discrete superposition is terminated. In a 3-D synthesis there are 8 types of truncation phases, corresponding to 4 sides and 4 corners of the region covered by ray end points. Narrow beam widths can remove these truncation phases, but can also sometimes remove physical radiation. A known example is that of head waves rays, in which a broad spectrum of angles is required to properly describe the head wave. Here, as shown in Figure 5.4, a so called "optimal" beam width (Klimes\**v*, 1986) removes physical radiation corresponding to slab diffraction. The consensus among investigators looking at a variety of 2- and 3-D problems is that in order to include phenomena requiring a broad angular spectrum, one must use as wide a beam width as feasible and make the technique approach the WKBJ/Maslov limit of plane wave superposition (Felsen, 1984; Madariaga, 1984; Wu, 1985; Thomson and Chapman, 1986; Lu et al., 1987). Truncation phases can to some extent be reduced by a small amount of Gaussian beams, or as suggested by Thomson and Chapman (1986) be minimized by asymptotically estimating the integrals in the total angular range up to the truncation angles. This was the procedure used in the "end-point corrected" seismogram in Figure 5.4. In the slab problem, truncation phases can be easily reduced by including more rays in a region of the model in which the calculation can be performed analytically and cheaply. Cormier (1986) describes how fast, analytic integration of the dynamic ray tracing equations can be performed in 1-D, radially symmetric portions of the model and the and simply connected with numerically integrated quantities in the laterally varying portions of the model. radially symmetric portions in the model is described in Cormier (1986a).

The example calculations shown in this proposal have not yet included source radiation, attenuation, reflection/transmission coefficients, and S wave polarization. All of these calculations are well developed and described in a recent text by Cervený (1985b). The programs with which example calculations shown in this proposal have been made incorporate all of these effects, but they have not yet been all tested.

### 5.3 REFERENCES

- Chapman, C.H., A new method for computing synthetic seismograms, *Geophys. J. R. Astr. Soc.*, **54**, 481-518, 1978.
- Chapman, C.H., and R. Drummond, Body-wave seismograms in inhomogeneous media using Maslov asymptotic theory, *Bull. Seism. Soc. Am.*, **72**, S277-S317, 1982.
- Červený, V., and F. Hron, The ray series method and dynamic ray tracing systems for three-dimensional inhomogeneous media, *Bull. Seism. Soc. Am.*, **70**, 47-77, 1980.
- Červený, V., The application of ray tracing to the propagation of shear waves in complex media, in *Seismic Exploration*, eds. Treitel, S., and Helbig, K., Vol. on Seismic Shear Waves, ed. Dohr, G., Geophysical Press, pp. 1-124, 1985a.
- Červený, V., Gaussian beam synthetic seismograms, *J. Geophys.*, **58**, 44-72, 1985b.
- Cormier, V.F., The polarization of S waves in a heterogeneous isotropic Earth model, *J. Geophys.*, **56**, 20-23, 1984.
- Cormier, V.F., An application of the propagator matrix of dynamic ray tracing: the focusing and defocusing of body waves by three-dimensional velocity structure in the source region. *Geophys. J. R. Astr. Soc.*, **87**, 1159-1180, 1986.
- Creager, K.C., and T.H. Jordan, Slab penetration into the lower mantle beneath the Mariana and other island arcs of the northwest Pacific, *J. Geophys. Res.*, **91**, 3573-3590, 1986.
- Felsen, L.B., Geometrical theory of diffraction, evanescent waves, complex rays and Gaussian beams, *Geophys. J. R. Astr. Soc.*, **79**, 77-88, 1984.
- Klimeš, L., Expansion of a high-frequency time-harmonic wavefield given on an initial surface into Gaussian beams, *Geophys. J. R. Astr. Soc.*, **79**, 105-118, 1984.
- Klimeš, L., Discretization error for the superposition of Gaussian beams, *Geophys. J. R. Astr. Soc.*, **86**, 531-551, 1986.
- Lu, I.T., L.B. Felsen, and Y.Z. Ruan, Spectral aspects of the Gaussian beam method: reflection from a homogeneous half space, *Geophys. J. R. Astr. Soc.*, in press, 1987.
- Madariaga, R., Gaussian beam synthetic seismograms in a vertically varying medium, *Geophys. J. R. Astr. Soc.*, **79**, 589-612, 1984.
- Madariaga, R., and P. Papadimitriou, Gaussian beam modelling of upper mantle phases, *Ann. Geophysicae*, **6**, 799-812, 1985.
- Miner, J.W., and M.N. Toksöz, Thermal regime of a downgoing slab and new global tectonics, *J. Geophys. Res.*, **78**, 6009-6020, 1973.
- Silver, P.G., and W.W. Chan, Observations of body-wave multipathing from broad-band seismograms: Evidence for lower-mantle slab penetration beneath the Sea of Okhotsk, *J. Geophys. Res.*, **91**, 13787-13802, 1986.
- Thomson, C.J., and C.H. Chapman, An introduction to Maslov's asymptotic method,

*Geophys. J. R. Astr. Soc.*, **83**, 143-168, 1985.

Thomson, C.J., and C.H. Chapman, End-point contributions to synthetic seismograms, *Geophys. J. R. Astr. Soc.*, **87**, 285-294, 1986.

Toksöz, M.N., J.W. Minear, and B.R. Julian, Temperature field and geophysical effects of a downgoing slab, *J. Geophys. Res.*, **76**, 1113-1138, 1971.

Vidale, J.E., Waveform effects of a high-velocity, subducted slab, *J. Geophys. Res.*, submitted, 1986.

DISTRIBUTION LIST

Dr. Monem Abdel-Gawad  
Rockwell Internat'l Science Center  
1049 Camino Dos Rios  
Thousand Oaks, CA 91360

Professor Keiiti Aki  
Center for Earth Sciences  
University of Southern California  
University Park  
Los Angeles, CA 90089-0741

Professor Shelton S. Alexander  
Geosciences Department  
403 Deike Building  
The Pennsylvania State University  
University Park, PA 16802

Professor Charles B. Archambeau  
Cooperative Institute for Resch  
in Environmental Sciences  
University of Colorado  
Boulder, CO 80309

Dr. Thomas C. Bache Jr.  
Science Applications Int'l Corp.  
10210 Campus Point Drive  
San Diego, CA 92121

Dr. James Bulau  
Rockwell Int'l Science Center  
1049 Camino Dos Rios  
P.O. Box 1085  
Thousand Oaks, CA 91360

Dr. Douglas R. Baumgardt  
Signal Analysis & Systems Div.  
ENSCO, Inc.  
5400 Port Royal Road  
Springfield, VA 22151-2388

Dr. S. Bratt  
Science Applications Int'l Corp.  
10210 Campus Point Drive  
San Diego, CA 92121

Woodward-Clyde Consultants  
Attn: Dr. Lawrence J. Burdick  
Dr. Jeff Barker  
P.O. Box 93245  
Pasadena, CA 91109-3245 (2 copies)

Dr. Roy Burger  
1221 Serry Rd.  
Schenectady, NY 12303

Professor Robert W. Clayton  
Seismological Laboratory/Div of  
Geological & Planetary Sciences  
California Institute of Technology  
Pasadena, CA 91125

Dr. Vernon F. Cormier/Earth Resources  
Lab, Dept of Earth, Atmospheric and  
Planetary Sciences  
MIT - 42 Carleton Street  
Cambridge, MA 02142

Professor Anton M. Dainty  
AFGL/LWH  
Hanscom AFB, MA 01731

Dr. Zoltan A. Der  
Teledyne Geotech  
314 Montgomery Street  
Alexandria, VA 22314

Prof. Adam Dziewonski  
Hoffman Laboratory  
Harvard University  
20 Oxford St.  
Cambridge, MA 02138

Professor John Ebel  
Dept of Geology & Geophysics  
Boston College  
Chestnut Hill, MA 02167

Professor John Ferguson  
Center for Lithospheric Studies  
The University of Texas at Dallas  
P.O. Box 830688  
Richardson, TX 75083-0688



Dr. Jeffrey W. Given  
Sierra Geophysics  
11255 Kirkland Way  
Kirkland, WA 98033

Prof. Roy Greenfield  
Geosciences Department  
403 Deike Building  
The Pennsylvania State University  
University Park, PA 16802

Professor David G. Harkrider  
Seismological Laboratory  
Div of Geological & Planetary Sciences  
California Institute of Technology  
Pasadena, CA 91125

Professor Donald V. Helmberger  
Seismological Laboratory  
Div of Geological & Planetary Sciences  
California Institute of Technology  
Pasadena, CA 91125

Professor Eugene Herrin  
Institute for the Study of Earth  
& Man/Geophysical Laboratory  
Southern Methodist University  
Dallas, TX 75275

Professor Robert B. Herrmann  
Department of Earth & Atmospheric  
Sciences  
Saint Louis University  
Saint Louis, MO 63156

Professor Lane R. Johnson  
Seismographic Station  
University of California  
Berkeley, CA 94720

Professor Thomas H. Jordan  
Department of Earth, Atmospheric  
and Planetary Sciences  
Mass Institute of Technology  
Cambridge, MA 02139

Dr. Alan Kafka  
Department of Geology  
& Geophysics  
Boston College  
Chestnut Hill, MA 02167

Professor Charles A. Langston  
Geosciences Department  
403 Deike Building  
The Pennsylvania State University  
University Park, PA 16802

Professor Thorne Lay  
Department of Geological Sciences  
1006 C.C. Little Building  
University of Michigan  
Ann Arbor, MI 48109-1063

Dr. George R. Mellman  
Sierra Geophysics  
11255 Kirkland Way  
Kirkland, WA 98033

Professor Brian J. Mitchell  
Department of Earth & Atmospheric  
Sciences  
Saint Louis University  
Saint Louis, MO 63156

Professor Thomas V. McEvilly  
Seismographic Station  
University of California  
Berkeley, CA 94720

Dr. Keith L. McLaughlin  
Teledyne Geotech  
314 Montgomery Street  
Alexandria, VA 22314

Professor Otto W. Nuttli  
Department of Earth &  
Atmospheric Sciences  
Saint Louis University  
Saint Louis, MO 63156

Professor Paul G. Richards  
Lamont-Doherty Geological  
Observatory of Columbia Univ.  
Palisades, NY 10964

Dr. Norton Rimer  
S-Gibed  
A Division of Maxwell Lab  
P.O. 1620  
La Jolla, CA 92038-1620

Professor Larry J. Ruff  
Department of Geological Sciences  
1006 C.C. Little Building  
University of Michigan  
Ann Arbor, MI 48109-1063

Professor Charles G. Sammis  
Center for Earth Sciences  
University of Southern California  
University Park  
Los Angeles, CA 90089-0741

Dr. David G. Simpson  
Lamont-Doherty Geological Observ.  
of Columbia University  
Palisades, NY 10964

Dr. Jeffrey L. Stevens  
S-CUBED,  
A Division of Maxwell Laboratory  
P.O. Box 1620  
La Jolla, CA 92038-1620

Professor Brian Stump  
Institute for the Study of Earth & Man  
Geophysical Laboratory  
Southern Methodist University  
Dallas, TX 75275

Professor Ta-liang Teng  
Center for Earth Sciences  
University of Southern California  
University Park  
Los Angeles, CA 90089-0741

Dr. R. B. Tittmann  
Rockwell International Science Ctr  
1049 Camino Dos Rios  
P.O. Box 1085  
Thousand Oaks, CA 91360

Professor M. Nafi Toksoz/Earth Resources  
Lab - Dept of Earth, Atmospheric and  
Planetary Sciences  
MIT - 42 Carleton Street  
Cambridge, MA 02142

Professor Terry C. Wallace  
Department of Geosciences  
Building #11  
University of Arizona  
Tucson, AZ 85721

Prof. John H. Woodhouse  
Hoffman Laboratory  
Harvard University  
20 Oxford St.  
Cambridge, MA 02138

Dr. G. Blake  
US Dept of Energy/DP 331  
Forrestal Building  
1000 Independence Ave.  
Washington, D.C. 20585

Dr. Michel Bouchon - Universite  
Scientifique et Medicale de Grenoble  
Lab de Geophysique - Interne et  
Tectonophysique - I.R.I.G.M.-B.P.  
38402 St. Martin D'Herès  
Cedex FRANCE

Dr. Hilmar Bungum/NTNF/NORSAR  
P.O. Box 51  
Norwegian Council of Science,  
Industry and Research, NORSAR  
N-2007 Kjeller, NORWAY

Dr. Alan Douglas  
Ministry of Defense  
Blacknest, Brompton,  
Reading RG7-4RS  
UNITED KINGDOM

Professor Peter Harjes  
Institute for Geophysik  
Rhur University/Bochum  
P.O. Box 102148, 4630 Bochum 1  
FEDERAL REPUBLIC OF GERMANY

Dr. James Hannon  
Lawrence Livermore Nat'l Lab.  
P.O. Box 808  
Livermore, CA 94550

Dr. E. Husebye  
NTNF/NORSAR  
P.O. Box 51  
N-2007 Kjeller, NORWAY

Dr. Arthur Lerner-Lam  
Lamont-Doherty Geological  
Observatory of Columbia Univ.  
Palisades, NY 10964

Mr. Peter Marshall, Procurement  
Executive, Ministry of Defense  
Blacknest, Brimpton,  
Reading RG7-4RS  
UNITED KINGDOM

Dr. B. Massinon  
Societe Radiomana  
27, Rue Claude Bernard  
75005, Paris, FRANCE

Dr. Pierre Mechler  
Societe Radiomana  
27, Rue Claude Bernard  
75005, Paris, FRANCE

Mr. Jack Murphy - S-CUBED  
Reston Geophysics Office  
11800 Sunrise Valley Drive  
Suite 1212  
Reston, VA 22091

Dr. Svein Mykkeltveit  
NTNF/NORSAR  
P.O. Box 51  
N-2007 Kjeller, NORWAY

Dr. Carl Newton  
Los Alamos National Lab.  
P.O. Box 1663  
Mail Stop C 335, Group ESS3  
Los Alamos, NM 87545

Dr. Peter Easham/Earth Physics Branch  
Department of Energy and Mines  
1 Observatory Crescent  
Ottawa, Ontario  
CANADA K1A 0Y3

Professor J. A. Orcutt  
Geological Sciences Div.  
Univ. of California at  
San Diego  
La Jolla, CA 92093

Dr. Frank F. Pilotte  
Director of Geophysics  
Headquarters Air Force Technical  
Applications Center  
Patrick AFB, Florida 32925-6001

Mr. Jack Raclin  
USGS - Geology, Rm 3C136  
Mail Stop 928 National Center  
Reston, VA 22092

Dr. Frode Ringdal  
NTNF/NORSAR  
P.O. Box 51  
N-2007 Kjeller, NORWAY

Dr. George H. Rothe  
Chief, Research Division  
Geophysics Directorate  
HQ Air Force Technical Applications C  
Patrick AFB, Florida 32925-6001

Dr. Alan S. Ryall, Jr.  
Center for Seismic Studies  
1300 North 17th Street  
Suite 1450  
Arlington, VA 22209-2308

Dr. Jeffrey L. Stevens  
S-CUBED  
A Division of Maxwell Lab.  
P.O. Box 1620  
La Jolla, CA 92038-1620

Dr. Lawrence Turnbull  
OSWR/NED  
Central Intelligence Agency  
CIA, Room 5G48  
Washington, DC 20505

Professor Steven Grand  
Department of Geology  
245 Natural History Bldg  
1301 West Green Street  
Urbana, IL 61801

Professor Keith Priestley  
University of Nevada  
Mackay School of Mines  
Reno, Nevada 89557

DARPA/PM  
1400 Wilson Boulevard  
Arlington, VA 22209

Defense Technical  
Information Center  
Cameron Station  
Alexandria, VA 22314  
(12 copies)

Defense Intelligence Agency  
Directorate for Scientific &  
Technical Intelligence  
Washington, D.C. 20301

Defense Nuclear Agency  
Shock Physics Directorate/SS  
Washington, D.C. 20305

Defense Nuclear Agency/SPSS  
ATTN: Dr. Michael Shore  
6801 Telegraph Road  
Alexandria, VA 22310

AFOSR/NPG  
ATTN: Director  
Bldg 410, Room C222  
Bolling AFB, Wash D.C. 20332

AFTAC/CA (STINFO)  
Patrick AFB, FL 32925-6001

AFWL/NTESC  
Kirtland AFB, NM 87171

U.S. Arms Control & Disarm. Agency  
ATTN: Mrs. M. Hoinkes  
Div. of Multilateral Affairs,  
Room 5499  
Washington, D.C. 20451

U.S. Geological Survey  
ATTN: Dr. T. Hanks  
Nat'l Earthquake Resch Center  
345 Middlefield Road  
Menlo Park, CA 94025

SRI International  
333 Ravensworth Avenue  
Menlo Park, CA 94025

Center for Seismic Studies  
ATTN: Dr. C. Romney  
1300 North 17th Street  
Suite 1450  
Arlington, VA 22209 (3 copies)

Dr. Robert Blandford  
DARPA/GSD  
1400 Wilson Boulevard  
Arlington, VA 22209-2308

Ms. Ann Kerr  
DARPA/GSD  
1400 Wilson Boulevard  
Arlington, VA 22209-2308

Dr. Ralph Alewine III  
DARPA/GSD  
1400 Wilson Boulevard  
Arlington, VA 22209-2308

Mr. Edward Giller  
Pacific Sierra Research Corp.  
1401 Wilson Boulevard  
Arlington, VA 22209

Science Horizons, Inc.  
Attn: Dr. Bernard Minster  
Dr. Theodore Cherry  
710 Encinitas Blvd., Suite 101  
Encinitas, CA 92024 (2 copies)

Dr. Jack Evernden  
USGS - Earthquake Studies  
345 Middlefield Road  
Menlo Park, CA 94025

Dr. Lawrence Braille  
Department of Geosciences  
Purdue University  
West Lafayette, IN 47907

Dr. G.A. Bollinger  
Department of Geological Sciences  
Virginia Polytechnical Institute  
21044 Derring Hall  
Blacksburg, VA 24061

Dr. L. Sykes  
Lamont Doherty Geological Observ.  
Columbia University  
Palisades, NY 10964

Dr. S.W. Smith  
Geophysics Program  
University of Washington  
Seattle, WA 98195

Dr. L. Timothy Long  
School of Geophysical Sciences  
Georgia Institute of Technology  
Atlanta, GA 30332

Dr. N. Biswas  
Geophysical Institute  
University of Alaska  
Fairbanks, AK 99701

Dr. Freeman Gilbert - Institute of  
Geophysics & Planetary Physics  
Univ. of California at San Diego  
P.O. Box 109  
La Jolla, CA 92037

Dr. Pradeep Talwani  
Department of Geological Sciences  
University of South Carolina  
Columbia, SC 29208

University of Hawaii  
Institute of Geophysics  
Attn: Dr. Daniel Walker  
Honolulu, HI 96822

Dr. Donald Forsyth  
Dept. of Geological Sciences  
Brown University  
Providence, RI 02912

Dr. Jack Oliver  
Department of Geology  
Cornell University  
Ithaca, NY 14850

Dr. Muawia Barazangi  
Geological Sciences  
Cornell University  
Ithaca, NY 14853

Rondout Associates  
Attn: Dr. George Sutton,  
Dr. Jerry Carter, Dr. Paul Pomeroy  
P.O. Box 224  
Stone Ridge, NY 12484 (3 copies)

Dr. Bob Smith  
Department of Geophysics  
University of Utah  
1400 East 2nd South  
Salt Lake City, UT 84112

Dr. Anthony Gangi  
Texas A&M University  
Department of Geophysics  
College Station, TX 77843

Dr. Gregory B. Young  
ENSOC, Inc.  
5400 Port Royal Road  
Springfield, CA 22151

Dr. Ben Menaheim  
Weizman Institute of Science  
Rehovot, ISRAEL 951729

Weidlinger Associates  
Attn: Dr. Gregory Wojcik  
620 Hansen Way, Suite 100  
Palo Alto, CA 94304

Dr. Leon Knopoff  
University of California  
Institute of Geophysics  
& Planetarysics  
Los Angeles, CA 90024

Dr. Kenneth H. Olsen  
Los Alamos Scientific Lab.  
Post Office Box 1663  
Los Alamos, NM 87545

Prof. Jon F. Claerbout  
Prof. Amos Nur  
Dept. of Geophysics  
Stanford University  
Stanford, CA 94305 (2 copies)

AFGL/XO  
Hanscom AFB, MA 01731-5000

Dr. Robert Burridge  
Schlumberger-Doll Resch Ctr.  
Old Quarry Road  
Ridgefield, CT 06877

AFGL/LW  
Hanscom AFB, MA 01731-5000

Dr. Eduard Berg  
Institute of Geophysics  
University of Hawaii  
Honolulu, HI 96822

AFGL/SULL  
Research Library  
Hanscom AFB, MA 01731-5000 (2 copies)

Mr. Robert Phinney/Dr. F. A. Dahle  
Dept. of Geological  
Geophysical Sci. University  
Princeton University  
Princeton, NJ 08540 (2 copies)

Secretary of the Air Force (SAFRD)  
Washington, DC 20330

Dr. Kin-Yip Chun  
Geophysics Division  
Physics Department  
University of Toronto  
Ontario, CANADA M5S 1A7

Office of the Secretary Defense  
DDR & E  
Washington, DC 20330

New England Research, Inc.  
Attn: Dr. Randolph Martin III  
P.O. Box 857  
Norwich, VT 05055

HQ DNA  
Attn: Technical Library  
Washington, DC 20305

Sandia National Laboratory  
Attn: Dr. H.B. Durham  
Albuquerque, NM 87185

Director, Technical Information  
DARPA  
1400 Wilson Blvd.  
Arlington, VA 22209

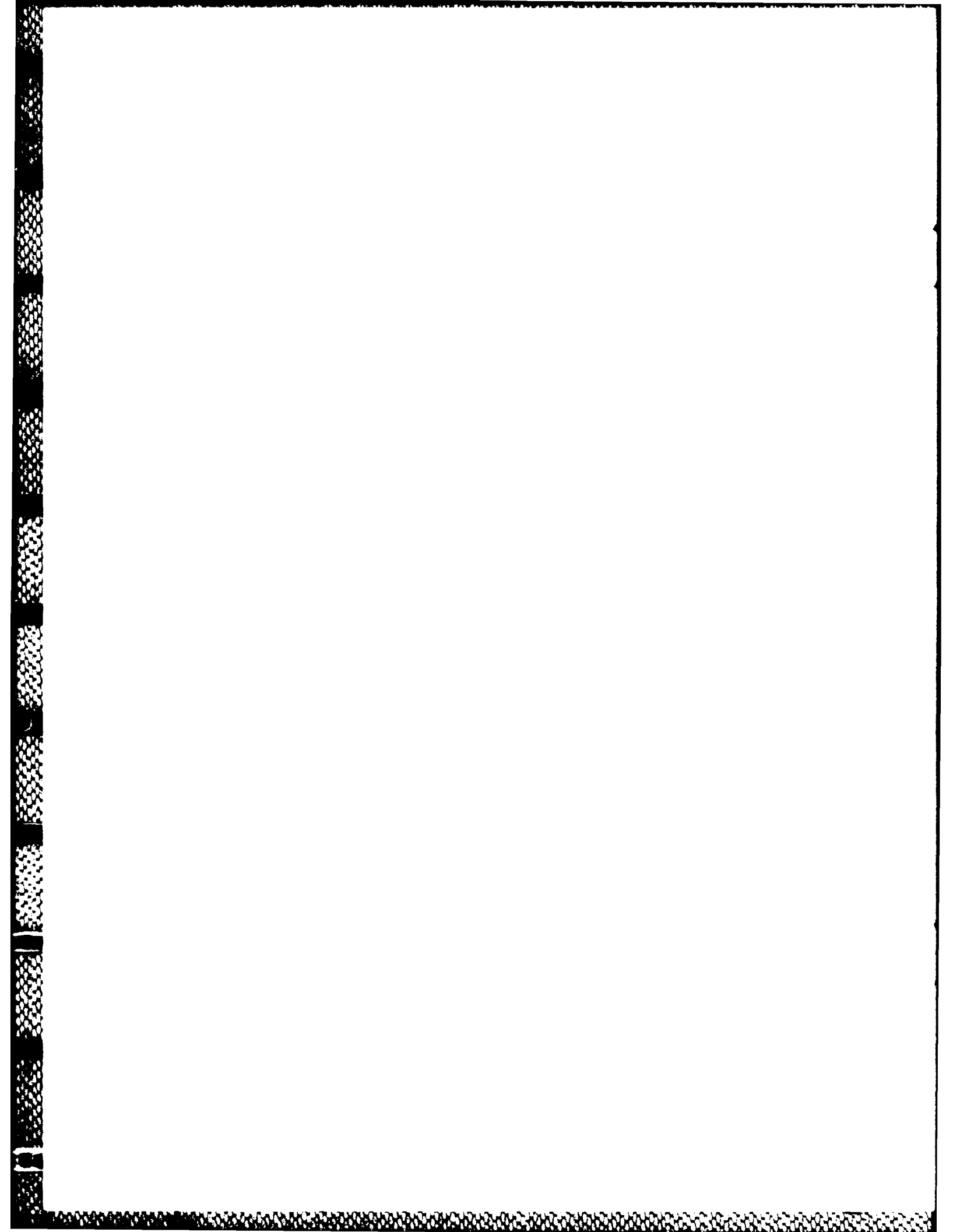
Dr. Thomas Weaver  
Los Alamos Scientific Laboratory  
Los Alamos, NM 87544

Los Alamos Scientific Laboratory  
Attn: Report Library  
Post Office Box 1663  
Los Alamos, NM 87544

Dr. Gary McCartor  
Mission Research Corp.  
375 State Street  
Santa Barbara, CA 93102

Dr. Al Florence  
SRI International  
333 Ravenwood Avenue  
Menlo Park, CA 94025-3493

Dr. W. H. K. Lee  
USGS  
Office of Earthquakes, Volcanoes,  
& Engineering  
Branch of Seismology  
345 Middlefield Rd  
Menlo Park, CA 94025



END

10-87

DTIC